Center for Environmentally Sustainable Transportation in Cold Climates

Development of a Design Method for H2Ri Wicking Fabric in Pavement Structures

Chuang Lin, Graduate Research Assistant
Xiong Zhang, Ph.D., P.E.
Department of Civil and Environmental Engineering
University of Alaska Fairbanks
and
Jie Han, Ph.D., P.E.
Department of Civil, Environmental, and Architectural Engineering
University of Kansas

Date: November 2016

Prepared by:

Center for Environmentally Sustainable Transportation in Cold Climates
Duckering Building, Room 245
P.O. Box 755900
Fairbanks, AK 99775

INE/AUTC 17.02

REPORT DOCUMENTATION PAGE

Form approved OMB No.

1. AGENCY USE ONLY (LEAVE BLANK)	2. REPORT DATE	3. REPORT TYPE AND DATES COVERED
	11/2016	Final Report: 06/2013 – 11/2016

4. TITLE AND SUBTITLE

Development of a Design Method for H2Ri Wicking Fabric in Pavement Structures

5. FUNDING NUMBERS

6. AUTHOR(S)

Chuang Lin, Graduate Research Assistant
Xiong Zhang, Ph.D., P.E.
University of Alaska Fairbanks
Jie Han, Ph.D., P.E.
University of Kansas

7. PERFORMING ORGANIZATION NAME(S) AND ADDRESS(ES)

Center for Environmentally Sustainable Transportation in Cold Climates
University of Alaska Fairbanks
Duckering Building, Room 245
P.O. Box 755900
Fairbanks, AK 99775-5900

8. PERFORMING ORGANIZATION REPORT NUMBER

9. SPONSORING/MONITORING AGENCY NAME(S) AND ADDRESS(ES)

TenCate Geosynthetics
365 South Holland Drive
Pendergrass, GA 30567

10. SPONSORING/MONITORING AGENCY REPORT NUMBER

11. SUPPLENMENTARY NOTES

12a. DISTRIBUTION / AVAILABILITY STATEMENT

No restrictions

12b. DISTRIBUTION CODE

13. ABSTRACT (Maximum 200 words)

A new roadway drainage design concept is proposed to reduce the roadway water content and enhance the overall pavement performance by implementing H2Ri geotextile with lateral wicking ability. Compared with conventional drainage materials, this type of geotextile has high tensile strength and higher specific surface area, which enable to continuously transport water under unsaturated conditions. SEM (Scanning Electron Microscope) images indicated that the geotextile functions effectively for soils with particle size larger than 12 microns. A series of tests were performed to establish the relationships among different parameters, including resilient modulus test, large-scale direct shear test, salt concentration test and pressure plate test. Test results indicated that the soil-geotextile system can work effectively to reduce the water content within the pavement structure by 2%. By doing so, the corresponding resilient modulus can be increased by 3 times and the permanent deformation can be reduced to half of that value. Meanwhile, the interface frictional strength between geotextile and soil was not sensitive to water content change.

14- KEYWORDS : Geotextiles, Subsurface Drainage, Unsaturated Soils, Capillarity, Embankments

15. NUMBER OF PAGES: 95

16. PRICE CODE: N/A

17. SECURITY CLASSIFICATION OF REPORT	18. SECURITY CLASSIFICATION OF THIS PAGE	19. SECURITY CLASSIFICATION OF ABSTRACT	20. LIMITATION OF ABSTRACT
Unclassified	Unclassified	Unclassified	N/A

Development of a Design Method for H2Ri Wicking Fabric in Pavement Structures

Final Project Report

By

Chuang Lin, Graduate Research Assistant

Xiong Zhang, Ph.D., P.E.
Associate Professor

Department of Civil and Environmental Engineering
University of Alaska Fairbanks

Jie Han, Ph.D., P.E.

Department of Civil, Environmental, and Architectural Engineering
University of Kansas

Project Title: Development of a Design Method for H2Ri Wicking Fabric in Pavement Structures

November 2016

DISCLAIMER

This document is disseminated under the sponsorship of the U.S. Department of Transportation in the interest of information exchange. The U.S. Government assumes no liability for the use of the information contained in this document. The U.S. Government does not endorse products or manufacturers. Trademarks or manufacturers' names appear in this report only because they are considered essential to the objective of the document.

Opinions and conclusions expressed or implied in the report are those of the author(s). They are not necessarily those of the funding agencies. This report does not constitute a standard, specification, or regulation.

METRIC (SI*) CONVERSION FACTORS

APPROXIMATE CONVERSIONS TO SI UNITS

Symbol	When You Know	Multiply By	To Find	Symbol
		LENGTH		
in	inches	25.4		mm
ft	feet	0.3048		m
yd	yards	0.914		m
mi	Miles (statute)	1.61		km
		AREA		
in^2	square inches	645.2	millimeters squared	cm^2 ft^2
	square feet	0.0929	meters squared	m^2
yd^2	square yards	0.836	meters squared	m^2
mi^2	square miles	2.59	kilometers squared	km^2
ac	acres	0.4046	hectares	ha
		MASS (weight)		
oz	Ounces (avdp)	28.35	grams	g lb
	Pounds (avdp)	0.454	kilograms	kg T
	Short tons (2000 lb)	0.907	megagrams	mg
		VOLUME		
fl oz	fluid ounces (US)	29.57	milliliters	mL gal
	Gallons (liq)	3.785	liters	liters ft^3
	cubic feet	0.0283	meters cubed	m^3
yd^3	cubic yards	0.765	meters cubed	m^3

Note: Volumes greater than 1000 L shall be shown in m^3

		TEMPERATURE (exact)		
°F temperature	Fahrenheit	5/9 (°F-32)	Celsius temperature	°C
		ILLUMINATION		
fc	Foot-candles	10.76	lux	lx
fl	foot-lamberts	3.426	candela/m^2	cd/cm^2
		FORCE and PRESSURE or STRESS		
lbf	pound-force	4.45	newtons	N psi
	pound-force per square inch	6.89	kilopascals	kPa

These factors conform to the requirement of FHWA Order 5190.1A *SI is the symbol for the International System of Measurements

APPROXIMATE CONVERSIONS FROM SI UNITS

Symbol	When You Know	Multiply By	To Find	Symbol
		LENGTH		
mm	millimeters	0.039	inches	in
m	meters	3.28	feet	ft
m	meters	1.09	yards	yd
km	kilometers	0.621	Miles (statute)	mi
		AREA		
mm^2	millimeters squared	0.0016	square inches	in^2 m^2
meters squared		10.764	square feet	ft^2 km^2 kilometers
squared		0.39	square miles	mi^2 ha hectares (10,000
m^2)		2.471	acres	ac
		MASS (weight)		
g	grams	0.0353	Ounces (avdp)	oz
kg	kilograms	2.205	Pounds (avdp)	lb mg
megagrams (1000 kg)		1.103	short tons	T
		VOLUME		
mL	milliliters	0.034	fluid ounces (US)	fl oz
liters	liters	0.264	Gallons (liq)	gal
m^3	meters cubed	35.315	cubic feet	ft^3
m^3	meters cubed	1.308	cubic yards	yd^3

		TEMPERATURE (exact)		
°C temperature	Celsius temperature	9/5 °C+32	Fahrenheit	°F
		ILLUMINATION		
lx	lux	0.0929	foot-candles	fc
cd/cm	candela/m^2	0.2919	foot-lamberts	fl
^{2}				
		FORCE and PRESSURE or STRESS		
N	newtons	0.225	pound-force	lbf
kPa	kilopascals	0.145	pound-force per square inch	psi

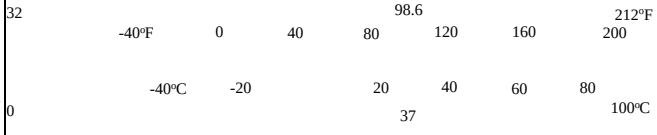

ACKNOWLEDGMENTS

The authors wish to express their appreciation to TenCate Geosynthetics (North America) for its funding support throughout this study.

TABLE OF CONTENTS

Page

DISCLAIMER ..... **I**

ACKNOWLEDGMENTS ..... **III**

TABLE OF CONTENTS ..... **IV**

LIST OF FIGURES ..... **VI**

LIST OF TABLES ..... **VIII**

EXECUTIVE SUMMARY **1**

CHAPTER 1.0 INTRODUCTION **3**

1.1 Problem Statement 3

1.2 Research Objectives 4

1.3 Research Methodology 4

CHAPTER 2.0 LITERATURE REVIEW **7**

2.1 Water Sources in Pavement Structures 7

2.2 Detrimental Effect of Water on Pavement Performance 8

2.3 Conventional Drainage Design Methods and Traditional Geotextile Applications ... 13

2.4 A Geotextile with Wicking Ability for Unsaturated Water Drainage 18

2.5 Potential Issues and Concerns 26

CHAPTER 3.0 MATERIAL CHARACTERIZATIONS **28**

3.1 Soil Properties 28

3.2 Resilient Modulus Test 29

3.3 Pressure Plate Test and Salt Concentration Test 39

3.4 H2Ri Geotextile Air Entry Value Determination 48

3.5 Unsaturated Soil Hydraulic Conductivity 51

3.6 Large Direct Shear Test 56

CHAPTER 4.0 GEOTEXTILE WORKING MECHANISM AND POTENTIAL ISSUES 63

4.1 H2Ri Geotextile Working Theoretical Range..... 63

4.2 Soil-Geotextile System Working Mechanism 64

4.3 Potential Issues..... 71

CHAPTER 5.0 CONCLUSIONS AND RECOMMENDATIONS 93

REFERENCES..... 96

APPENDIX A BASIC PROPERTIES FOR AB3 BASE COURSE 105

APPENDIX B RESILIENT MODULUS TEST..... 106

APPENDIX C SWCC AND GWCC TEST RESULTS..... 113

APPENDIX D LARGE-SCALE DIRECT SHEAR TEST 117

LIST OF FIGURES

Page

Figure 2.1 Conventional drainage design method 9

Figure 2.2 Adverse effects of water on asphalt concrete (AC) pavement (from Taylor and Khosla 1984) 10

Figure 2.3 Resilient modulus of Alaska D-1 materials at varying water contents (fines content = 3.15%, Southeast Region) 12

Figure 2.4 Ice lense formation 13

Figure 2.5 Capillary water in sandy soil 15

Figure 2.6 Geotextile with wicking fabric 20

Figure 2.7 Conceptual drainage design 22

Figure 3.1 Gradation curve and modified Proctor test 29

Figure 3.2 Resilient modulus test equipment 32

Figure 3.3 Resilient modulus and permanent deformation 34

Figure 3.4 Resilient modulus regression 38

Figure 3.5 Pressure plate test for soil 40

Figure 3.6 Pressure plate test for geotextile 44

Figure 3.7 Salt concentration test 45

Figure 3.8 SWCC and GWCC 47

Figure 3.9 Geotextile air entry value testing equipment (from Lin 2015) 50

Figure 3.10 Air entry value test results 51

Figure 3.11 Constant head test 53

Figure 3.12 Unsaturated hydraulic conductivity 55

Figure 3.13 Large-scale direct shear test equipment 57

Figure 3.14 Large direct shear test results 59

Figure 3.15 Determining shear strength from a SWCC 60
Figure 3.16 Predicted unsaturated soil shear strength at different water content levels 62
Figure 4.1 Soil-geotextile system working mechanism 68
Figure 4.2 Theoretical suction, water content, and resilient modulus distributions 71
Figure 4.3 SEM images of clogging effect 73
Figure 4.4 SEM images of mechanical failure 75
Figure 4.5 Aging effect 76
Figure 4.6 Loading plate test setup 79
Figure 4.7 SEM images from locations 1–4 81
Figure 4.8 SEM images of new H2Ri geotextile 82
Figure 4.9 SEM images of geotextile after washing 83
Figure 4.10 $Ca(OH)_2$ solute filtration 86
Figure 4.11 Reaction process 86
Figure 4.12 Geotextile sample air drying process 86
Figure 4.13 Salt concentration for soluble and insoluble salt (drying process) 88
Figure 4.14 Salt concentration for soluble and insoluble salt (wetting process) 89
Figure 4.15 Full-scale spectrum analysis 90
Figure 4.16 Soluble salt concentrations 92

LIST OF TABLES

Page

Table 2.1 H2Ri geotextile specifications 20

Table 3.1 Resilient modulus test loading sequence 32

Table 3.2 Absorption test 41

Table 3.3 Salt concentrations and corresponding suctions 45

Table 3.4 Soil-geotextile system reinforcement function efficiency 62

Table 4.1 SEM analyses summary 77

Table 4.2 Soil salinity 84

Table 4.3 Designed salt concentrations 85

Table A1 Sieve analysis data 105

Table A2 Modified proctor test data 105

Table B1 Resilient modulus test data 106

Table B2 Permanent deformation after test 112

Table C1 GWCC raw data 113

Table C2 SWCC raw data 116

Table D.1 Large-scale direct shear test data 117

EXECUTIVE SUMMARY

When a road is constructed, the soils within the embankment are often compacted at near-optimum water content to ensure better performance. Post-compaction water content tends to increase with time due to capillary water rising from the groundwater table and from infiltration of water from the road surface via pavement cracking. The soils are very sensitive to water content variation. A slight increment in water content will reduce soil stiffness, increase permanent deformation, and eventually compromise the road's long-term performance. One way to mitigate this issue is to implement a layer of geosynthetics, such as geotextile or geogrid, which increases embankment stiffness, providing additional confinement and lateral restriction via geosynthetics-soil interaction. Considering the thickness of a geotextile layer and the entire embankment, the efficiency of a geotextile is relatively limited. Moreover, road performance is not solely determined by the strength and interaction of the soil and geotextile, but relies on another sensitive factor: water content. Unfortunately, conventional subsurface drainage design methods only drain water driven by gravitational force (free water), and cannot deal with capillary water.

A newly developed H2Ri geotextile with wickability has the potential to laterally drain capillary water out of pavement structure under unsaturated conditions. It is possible that maintaining or reducing the embankment post-compaction water content may be an equivalent or more effective way (compared with enhancing the strength and stiffness of soils and geotextiles) to improve road performance. A series of lab tests were performed to characterize the properties of the selected soil and geotextile, and the interaction between the soil-geotextile system. By implementing the new geotextile and maintaining post-compaction water content at its optimum value, the resilient modulus can theoretically be increased by 3 times and permanent deformation

can be decreased to half. Structural benefits can be increased by 4–6 times if the water content is further reduced by 2%. Therefore, this type of geotextile is an efficient drainage material compared with conventional geotextiles and can equally or more effectively improve the performance of pavement over time.

CHAPTER 1.0 INTRODUCTION

1.1 Problem Statement

A new proprietary geotextile-H2Ri wicking fabric-manufactured by TenCate Geosynthetics (North America) contains both a high modulus polypropylene yarn for reinforcement and a nylon wicking yarn, which can absorb and transport water for drainage under unsaturated conditions. A dual-function geosynthetic product, H2Ri can serve as reinforcement and provide drainage. When properly designed, it has the potential to dehydrate the subgrade and base course and consequently improve the performance of pavements. This potential has been qualitatively confirmed by laboratory research (Zhang and Belmont 2009) performed at the University of Alaska Fairbanks (UAF) and by field testing at a small section constructed on the Dalton Highway at Mile 110, a location known as Beaver Slide in Alaska.

No method is available, however, to quantify the benefits of H2Ri in a pavement design. The current research to advance the knowledge of using H2Ri for reinforcement and drainage and to quantify the benefits of H2Ri in pavement design was divided into two parts. First, the proper daylight procedures for H2Ri were explored to wick water out of the geosynthetic. This study includes type of daylight procedure, rate of water movement with different types of daylight procedures, and a method that incorporates them in a pavement design.

Second, a design method was developed to properly incorporate the benefits of H2Ri into a pavement design. Currently TenCate uses the AASHTO (1993) pavement design guide to incorporate high-strength geosynthetics in a pavement. Current practice shows that the use of geosynthetic reinforcement increases the structural layer coefficient of a base course. It was expected that H2Ri could increase not only the structural layer coefficient of the base course but

also the drainage coefficient of the base course, the strength and modulus of the subgrade, because of its reinforcement and drainage functions.

1.2 Research Objectives

The objective of this research was to understand and demonstrate the mechanism of H2Ri to remove water and improve pavement structure performance at the elemental test level. The objective was achieved by establishing the relationship among different parameters such as water content, relative humidity, suction, permeability and permissivity, resilient modulus, and permanent deformation for soil and H2Ri wicking fabric and their interactions when simultaneously used.

1.3 Research Methodology

To achieve the objectives of this research, the following tasks were accomplished:

Task 1: Literature Review

Task 1 involved a comprehensive review of technical literature and research in progress on (1) the influence of water content variations on pavement performance, (2) the mechanisms and benefits of geosynthetic reinforcement of pavement applications, (3) the mechanisms of geosynthetic drainage and the benefits, including magnitude and range of moisture reduction, and (4) the existing geotextile design specifications and construction guidelines. Databases of TRB, TRIS, COMPENDIX, and UMI THESIS AND DISSERTATIONS were searched. Information and data from previous work conducted by different state Departments of Transportation on these topics were gathered, reviewed, and documented as well. A summary from this task provided direction and guidance for further tasks.

Task 2: Laboratory Tests to Characterize Soil and H2Ri Properties

Task 2 was performed mainly in the laboratory. Base course materials commonly used in the state of Kansas were selected and their gradation curves were determined. Prior to preparation of the specimens, the properties evaluated were aggregate gradation, water content, and plasticity index to obtain the liquid limit, plastic limit, and plasticity index for fines only. Compaction tests of the materials were performed to obtain optimum moisture content (OMC) and maximum dry density. Soil water characteristic curves (8-10 specimens) were performed to determine the ability of the soil to hold or drain water (i.e., suction) at different water contents. Constant head tests were performed to measure the permeability of soil under saturated conditions. The saturated permeability was combined with the soil water characteristic curve to predict the unsaturated permeability function under different suctions. Resilient modulus tests were performed at 6 different moisture conditions including (1) full saturation, (2) field capacity (drain of water under gravity, corresponding to the situation of conventional drainage), (3) Wopt+1~2%, (4) Wopt, (5) Wopt-2~3%, and (6) dry (corresponding to the situation at the soil surface). These test results demonstrated the influence of water content variation on soil resilient modulus and permanent deformations.

In addition to soil properties, the following material properties of the H2Ri wicking fabric were investigated or obtained from existing references: soil water characteristic curve, permissivity (hydraulic conductivity), and modulus. Large-scale direct shear tests were performed at 6 different moisture conditions: (1) full saturation, (2) field capacity, (3) Wopt+1~2%, (4) Wopt, (5) Wopt-2~3%, and (6) dry, to investigate the influence of water content variation on soil-geosynthetic interactions. Finally, all the information was combined to evaluate the effects of H2Ri wicking fabric on the performance of pavement structure.

Samples were collected from the field section to evaluate any potential mechanical damage, permanent deformation, clogging, or aging 5 years after installation. Then a lab loading plate test was performed to evaluate the effect of compaction and repetitive traffic loading on the geotextile's drainage ability. Moreover, a salt concentration test was conducted to explore the influence of drying-wetting cycles on clogging severity.

Task 3: Final report

Task 3 involved a final report that includes (1) a literature review, (2) the test results on unbounded granular base course materials and H2Ri wicking fabric at different moisture conditions and their interactions, and (3) the effects of including H2Ri wicking fabric on the performance of pavement structure.

CHAPTER 2.0 LITERATURE REVIEW

This research focus of this project was a method to quantify and incorporate the benefits of H2Ri geotextile to dehydrate the subgrade and base course of roadway to improve pavement system performance. In this chapter, water sources in pavement structure are examined, and the detrimental effects of water on the pavement's long-term performance are discussed in detail. The existing and conventional specifications and guidelines regarding the application of geotextile are explained to give an overview of the existing subsurface drainage design methods. A new drainage design concept that incorporates the application of H2Ri wicking fabric is demonstrated, and the existing successful applications of this type of geotextile are listed. Finally, potential issues related to H2Ri wicking fabric and the concerns about its extensive applications are discussed and evaluated.

2.1 Water Sources in Pavement Structures

There are three major sources of water in pavement structures: condensation at the pavement's surface, precipitation infiltration through existing cracks and joints, and water accumulation through capillary rise. Subsurface drainage is defined as the removal of excess water below the ground surface (water flows under gravitational force), and is the major component in flexible pavement drainage design. Subsurface water exists in four forms: water vapor, bounded water, capillary water, and free water (or gravitational water) (Aravin and Numerov 1953; Muskat 1946). In most cases, water vapor is stored inside soil pores where above the saturation zone. In existing subdrainage design methods, water vapor transmission is negligible. Bounded water is relatively hard to move from soil particles and can be considered

part of the soil particles. Bounded water in soil cannot move under gravitational force and therefore is not considered in subdrainage design methods. Capillary water also exists in soil pores where above the saturation zone. However, unlike water vapor, it can flow under the action of surface tension. The height of capillary rise is a function of the size of soil micropores, which relates to soil particle-size distribution and density (Barber and Sawyer 1952). Since capillary water cannot be drained out by gravity, the most common way to control capillary water is to lower the water table or use a capillary barrier, which blocks the upward capillary flow. Lastly, the most common type of water, namely free water, is the water in liquid form that flows under the force of gravity and obeys Darcy's law. The control of free water is a major concern in existing subdrainage design methods.

Subsurface water comes from a variety of sources and mainly falls into two categories: groundwater and infiltration. Groundwater refers to the water that exists in the saturation zone below the water table. Precipitation is the major source of groundwater. Infiltration water is defined as water that seeps into the pavement structure through the pavement surface, the shoulders, or the median. Precipitation is also the major source of infiltration water. For asphalt pavements, primary water infiltration occurs at longitudinal joints of shoulders and construction joints between strips of paving. For concrete slabs, water infiltration occurs through cracks, joints, and shoulders (Cedergren 1974; Cedergren et al. 1973).

2.2 Detrimental Effect of Water on Pavement Performance

When a road is constructed, soils are compacted at nearly optimum water content to achieve maximum dry density for the road's best performance (see Figure 2.1). After construction, the surface soil is exposed to the surrounding atmospheric environment and dries

quickly due to the air's low relative humidity (RH), usually <90%. Such a low RH value corresponds to a high suction value of 140 MPa (Fredlund and Rahardjo 1993). Under such high suction value, air enters into the voids of the embankment surface and forms an air-dried crust. This layer of crust has very low permeability (nearly impermeable) and impedes further water exchange loss. In the meantime, the soil inside the pavement structure tends to reach equilibrium with the surroundings. The only available water source is groundwater, since the shoulder and embankment are covered with impermeable crust. If the groundwater table is relatively low and the base course material contains higher fines content, the water content in the embankment will gradually increase due to capillary force under unsaturated conditions. Moreover, both thermal and stress-induced cracks will develop at the asphalt concrete layer over time. The infiltration rate for asphalt concrete will increase, and the infiltrated water will pond within the untreated base course layer. In other words, no matter how well the road is constructed, the water content of soil after construction tends to increase over time due to capillary rise from the groundwater table and water infiltration from the road surface via pavement cracking.

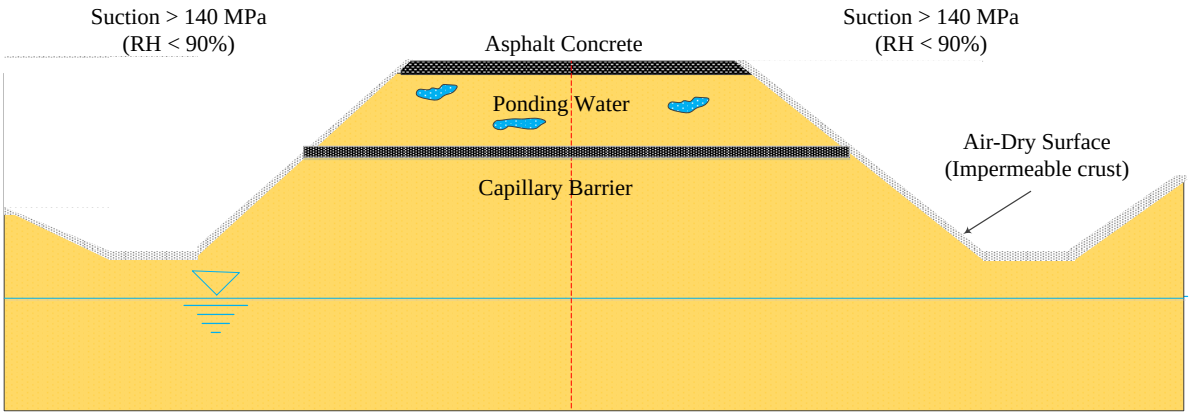

Figure 2.1 Conventional drainage design method

A slight water content increment significantly reduces soil stiffness, increases rutting depth, and eventually leads to degradation of roads. Excessive water in pavement structure is

recognized as one of the major adverse factors that influence a road's overall performance and causes a variety of engineering problems, as shown in Figure 2.2 (Taylor and Khosla 1983). Both dynamic traffic load and thermal shrinkage induce cracks within the asphalt pavement layer. Cracks partially or completely fill with water through infiltration and result in saturation of base and subgrade materials over time. Higher pore water pressure is induced by large dynamic loading of heavy-duty vehicles. In consequence, free water within the base and subgrade, together with fines, are squeezed out of the pavement structure. This phenomenon is called pumping. Free water wedges are produced beneath the asphalt pavement. Wet softened areas due to loss of fines in the base and subgrade layers cause potholes or depressions in the pavement structure.

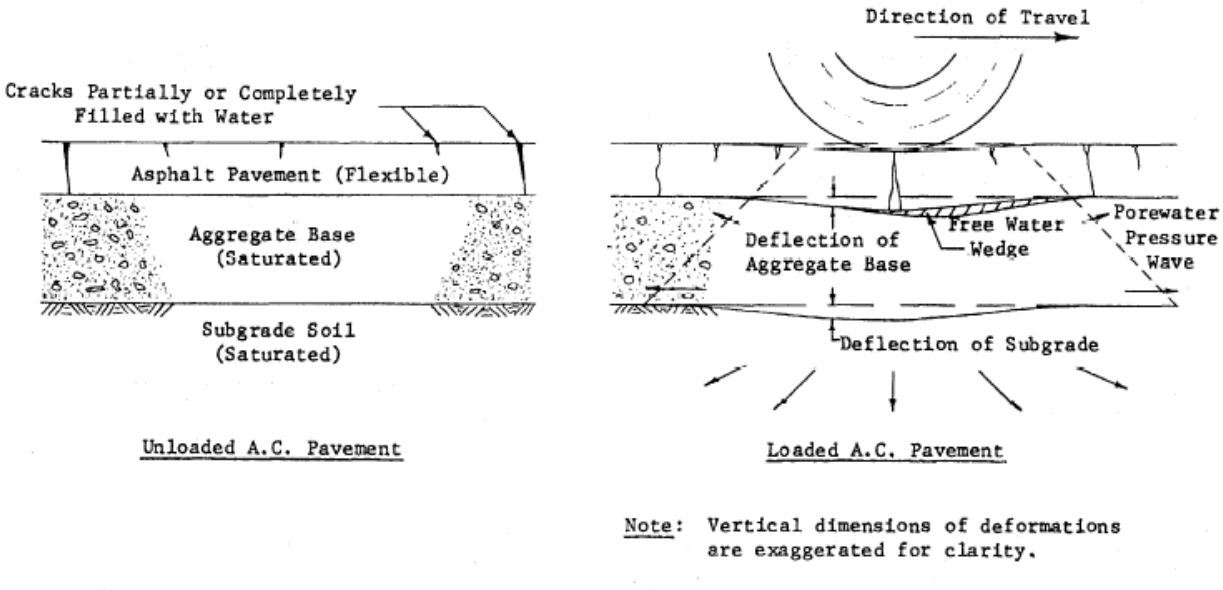

Figure 2.2 Adverse effects of water on asphalt concrete (AC) pavement (from Taylor and Khosla 1984)

The detrimental effects of water on flexible pavement have been documented in a variety of papers. In general, subsurface water was found to significantly affect the resilient response

characteristics of pavement materials in both laboratory and in situ conditions. Numerous researchers (e.g., Hicks and Monismith 1971; Barksdale and Itani 1989), who studied the behavior of granular materials at various degrees of saturation, have reported a notable dependence of resilient modulus on water content, with the modulus decreasing with growing saturation level. Haynes and Yoder (1963), for instance, observed a 50% decrease in resilient modulus in gravel as the degree of saturation increased from 70% to 97%. Figure 2.3 shows the effect of water content on resilient properties of Alaska D-1 materials (Southeast Region, fines content = 3.15%) (Li et al. 2011). Note that when water content decreases from 6.0% to 3.30%, the resilient modulus more than doubles. Subsurface water also significantly affects the permanent deformation of unbounded granular materials. For example, Haynes and Yoder (1963) reported that total permanent axial strain rose by more than 100% as the degree of saturation increased from 60% to 80%. Barksdale (1972) observed up to 68% greater permanent axial strain in soaked samples compared with those tested in unsaturated conditions. Thom and Brown (1987) noticed that a relatively small increase in water content could trigger a dramatic increase in permanent strain rate. Maree et al. (1982) reported that during in situ trials using a heavy vehicle simulator, the rutting potential of granular materials increased due to wetting.

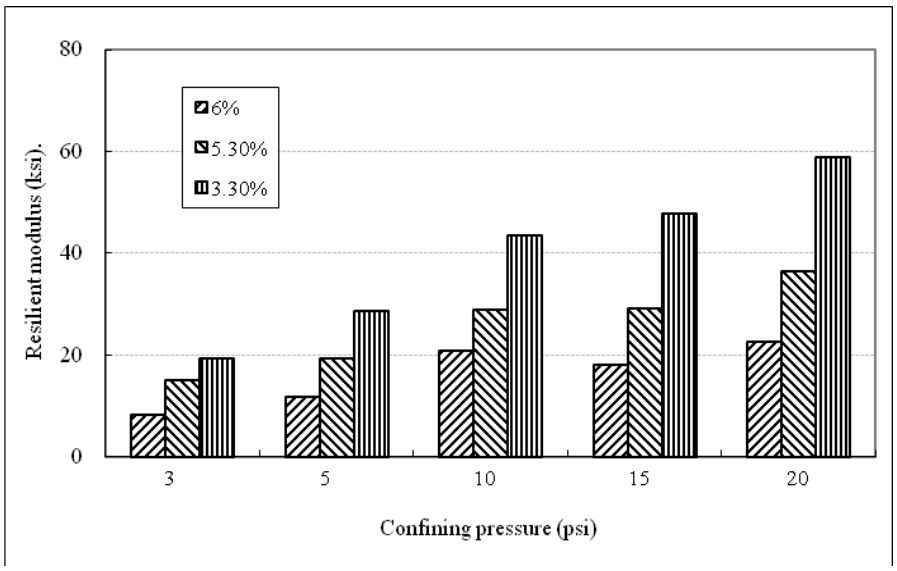

Figure 2.3 Resilient modulus of Alaska D-1 materials at varying water contents (fines content = 3.15%, Southeast Region)

Another adverse effect of subsurface water on pavement structure is called "frost boiling," which causes extensive damage in northern regions or cold climates. The mechanism of "frost boiling" phenomena is related to frost heave and thaw weakening processes (Chamberlain 1987), as shown in Figure 2.4. In coarse-grained base, subbase, and subgrade courses, water drains out fast. However, when encountered by courses with more fines, the fines content is susceptible to intruding into the base layer because of dynamic traffic load, and the water migration causes differential settlement. Frost heave is caused by the formation of an ice lens during freezing. Three key elements are required in the formation of an ice lens: (1) frost-susceptible (FS) soils, (2) subfreezing temperature, and (3) available water sources. Frost-susceptible soils are defined as soils with pore sizes between particles and particle surface area that promote capillary flow (Casagrande 1931 and 1947; Csathy and Townsend, 1962). During freezing period, water in large void space freezes into ice crystals as freezing front moving downward. Water expands about 9% by volume and is considered impermeable when frozen.

Negative pore water pressure was generated and ice crystals tend to attract water from adjacent voids. However, the frozen soil above the freezing front is impermeable and the only available water source comes from the unfrozen subgrade that beneath the freezing plane. As crystals continue to grow and are fed by capillary movement through FS soils, shallow groundwater continuously flows upward to the freezing plane. This will cause pavement to heave and sometimes crack. As the upcoming spring approaches, ice lenses start to melt and cause soft areas within the pavement structure (Taber 1929, 1930a and 1930b). When water drains out over time, differential settlement phenomena can be observed. Soft and weak soils provide limited friction and interlock between subgrade and base materials and result in rutting issues.

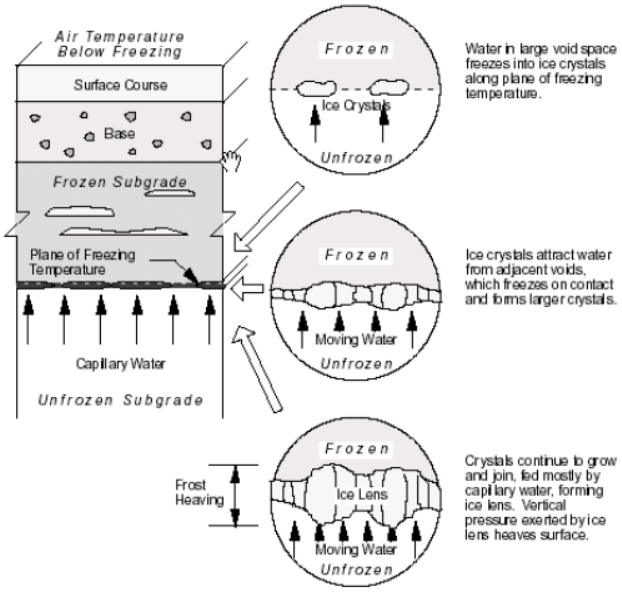

Figure 2.4 Ice lense formation

2.3 Conventional Drainage Design Methods and Traditional Geotextile Applications

Unfortunately, only infiltration water and groundwater seepage were taken into consideration in conventional subsurface drainage design methods (FHWA 1980; AASHTO

1993; MEPDG 2004). The term *time-to-drain* is used to determine the quantity of drainage conditions. For instance, if 50% of the water can be drained within 2 hours (1 month), the permeable base is considered in excellent (poor) drainage condition. In contrast, capillary water is considered undrainable by conventional drainage design methods. The traditional method of mitigating capillary rise is to use a layer of capillary barrier at the bottom of the base course (refer to Figure 2.1). A capillary barrier, that is, either soils such as sand or gravel that have a large pore size or nonwoven geotextiles, is often used to prevent capillary water from rising to the base course and wetting the aggregates. The working mechanism for a capillary barrier is the coarse-grained material or conventional nonwoven geotextile with larger pore size and lower air entry value (<1KPa) than the surrounding soil (Bouazza 2002; Bouazza et al. 2006). The hydraulic conductivity of the capillary barrier is much smaller than the ambient soil under unsaturated conditions. The capillary water cannot further move upward. However, researchers have proved that large amounts of capillary water remain within sandy material, which often is considered a good capillary barrier (Zhang and Belmont 2009), as shown in Figure 2.5. The sand shown in this figure had first been compacted and saturated in a plastic mold and covered with conventional geotextile. The mold was then placed upside down, allowing water to drain under gravitational force. As shown in Figure 2.5, the sand still holds a large amount of capillary water, which did not drain under the force of gravity. Over time, the capillary water would cause a water content increment in the embankment. Another issue related to conventional geotextile capillary barriers is breakthrough suction. At the breakthrough suction level, where suction in the capillary barrier equals suction in the surrounding soil (the hydraulic conductivities of those two materials are the same), the effect of the capillary barrier will diminish and water will gradually build up near the capillary barrier (Zornberg et al. 2010). Moreover, a capillary barrier can only

stop the flow of water in continuous liquid phase. Water can also transport in terms of vapor form, which cannot be stopped by the capillary barrier.

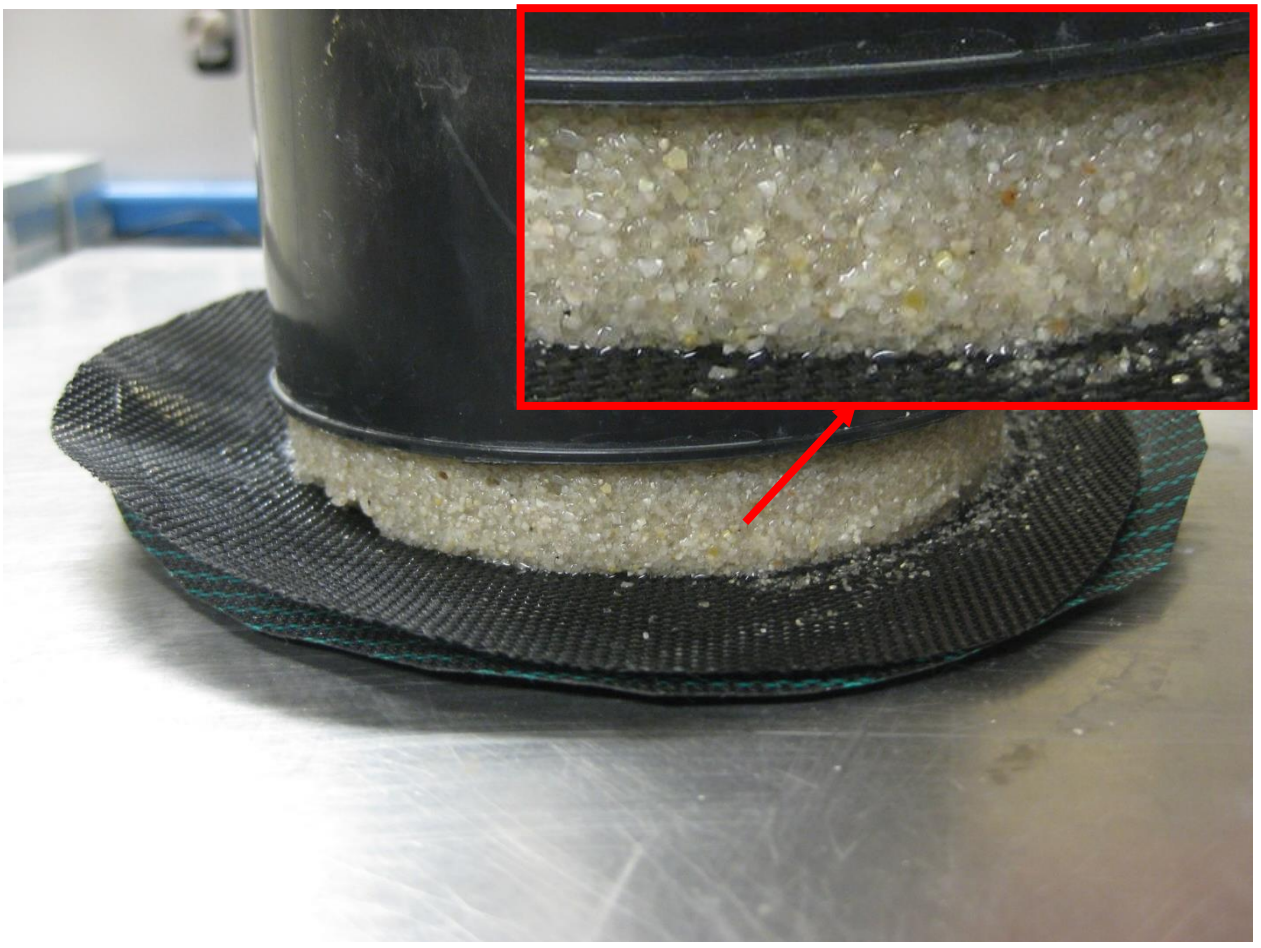

Figure 2.5 Capillary water in sandy soil

Since excess capillary water that has accumulated in an embankment significantly reduces pavement stiffness, which results in severe rutting, and cannot drain out by existing drainage design methods, a common way to mitigate excess capillary water is to use a layer of geotextile to provide additional reinforcement (Shukla and Yin 2006; Fredlund and Rahardjo 1993). Geotextiles have higher tensile strength, which provides lateral restraint of base and subgrade materials, increase system bearing capacity by forcing potential local surface failure to alternate, and provide additional wheel load support (Holtz et al. 1998).

A geotextile is defined as a permeable geosynthetic made of textile materials. A geotextile allows free water to flow across the geotextile plane while controlling soil particle retention. As water and small particles drain through confined layers of aggregates and subgrade, the smaller particles are trapped between the bigger particles, which results in larger grading and provides a more stable layer. Zornberg and Thompson (2010) summarized the major terminologies related to geotextiles. Only those terms relevant to this report are explained. According to the terminology established by ASTM Committee D35 on Geosynthetics and International Geosynthetics Society, "geotextile" is the term adopted. However, the term "fabric" is commonly used in research and industrial fields, so *fabric* and *geotextile* are used interchangeably in this report. *Filaments* are the polymers used to manufacture the geotextile fibers, and *yarns* refer to twisted or spun fibers. Two types of geotextiles are defined by the formations of fibers and yarns: Nonwoven geotextiles are fabricated by placing and orienting the filaments or fibers via needle punching or melt bonding methods, while woven geotextiles are manufactured using weaving methods. *Machine direction* refers to the manufacturing direction, and conversely *cross machine direction* refers to the direction that is perpendicular to the direction of manufacturing.

Geotextiles are widely used in transportation projects. In applications, geotextiles have five functions: separation, filtration, reinforcement, drainage, and capillary break (barrier). Each geotextile function is briefly summarized as follows:

Separation

Geotextiles serve as a separation material to prevent two dissimilar materials from intermixing (Koerner 2005). Soft subgrades (such as silt and clay soils) are susceptible to intruding up into the base layer due to dynamic traffic loads and water migration. Geotextiles as

a separation layer are important for maintaining the design thickness and local bearing capacity of base course materials.

Filtration

Filtration is defined as the equilibrium of a geotextile-soil system that allows for adequate liquid flow with limited soil loss across the plane of the geotextile over a service lifetime compatible with the application under consideration (Koerner 2005). Sometimes geotextiles are used as trench drain material, and the standard characterization of geotextile filtration criteria is apparent opening size (AOS).

Reinforcement

Geotextiles can improve a roadway's overall performance through reinforcement. Holtz et al. (1998) discussed the mechanism of geotextiles as reinforcement material. The bottom base course under traffic load tends to move laterally. Soft and weak soils provide limited friction and interlock between subgrade and base materials, resulting in rutting issues. Moreover, geotextiles are often used extensively with geogrids to enhance the reinforcement function in transportation applications.

Drainage

Geotextiles are now commonly used as an alternative drainage layer for conventional sand and gravel. The geotextile's drainage ability typically refers to its capacity to transfer water through its plane, and is quantified by the term *transmissivity*.

Capillary Barrier

Capillary barrier refers to the ability of a geotextile to prevent the passage of fluid. Geotextiles that serve as capillary barriers are often nonwoven and have especially low air entry values, similar to coarse soils. A critical suction, also referred as breakthrough suction, defines

the functional suction range for a geotextile being considered as a capillary barrier. As moisture increases near the location of the geotextile, the geotextile's conductivity also increases until the breakthrough suction is obtained and water breaks through the interface.

Although geotextiles and geogrids have proved effective at improving pavement performance, the long-term performance of a pavement system is not solely determined by soil or by geotextiles. The overall performance of pavement depends on the soil, geosynthetic, and soil-geosynthetic interaction. Considering only the geotextile reinforcement function sometimes cannot solve all engineering issues and may result in overestimating the long-term stiffness of pavement materials. In addition, compared with the entire thickness of the embankment (approximately 3 m), the influence range of the geotextile is limited due its relative thickness (often several millimeters). Soil is the dominant factor that controls performance of the road. In terms of soil, another equally important factor that affects the overall performance of pavement is water content. The performance of a soil-geotextile system can be poor when soil approaches saturation, and this weakening phenomenon is more obvious with higher fines content in the soil. Maintaining or reducing the embankment post-compaction water content can be an equivalent or more effective way (compared with conventional methods of enhancing the strength and stiffness of soils and geotextiles) to improve road performance.

2.4 A Geotextile with Wicking Ability for Unsaturated Water Drainage

Geotextiles are often considered construction materials that provide additional reinforcement and confinement to enhance pavement performance. However, pavement's long-term performance is also highly dependent on its post-compaction water content, as discussed in the previous section. Theoretically, if there is a way to connect the soils inside the embankment

with the outside environment and continuously transport water under unsaturated conditions, it is feasible to “wick” water out of the embankment by taking advantage of the natural suction gradient (induced by RH gradient within and outside the pavement structure). In other words, reducing the pavement water content is an equivalent or more effective alternative for improving pavement performance compared with conventional geotextile functions (providing higher tensile modulus and improving better load distribution by increasing the bonding between base and subbase courses).

A newly developed H2Ri geotextile with wickability drains water under unsaturated conditions, potentially improving pavement performance. The geotextile is made of special hydrophilic and hygroscopic 4DGTM fibers with multichannel cross sections, as shown in Figure 2.6. Figure 2.6(a) shows a scanning electron microscopic (SEM) photo of a single fiber. The diameter of the micropores (inner-yarn drainage) on the fibers varies from 5.7 microns to 47.8 microns, which enables the transport of water under unsaturated conditions. Figure 2.6(b) shows the design of the wicking fabric, a small piece having been torn apart. The drainage path between different wicking yarns is referred to as the inter-yarn drainage path. Figure 2.6(c) shows the top view of the woven weaves. The multichannel cross section has a high shape factor and a great number of channels per fiber (the specific surface area of wicking fabric is 3650 cm^2/g), which allow the wicking fabric to maximize capillary action and water transport in an unsaturated environment, as demonstrated in Figure 2.6(d). Table 2.1 lists some specifications of the H2Ri geotextile. The geotextile has a high tensile modulus and a high ability to transport water (permittivity of $0.24s^{-1}$, equivalent to a flow rate of 611 $L/min/m^2$). A salient feature of the wicking fabric is that it can maintain saturation in low relative humidity. In a laboratory environment (relative humidity about 50%), in 983 minutes, the wetting front of the water moves

1.86 m horizontally at a zero hydraulic gradient. With this feature, the geotextile can be used to build a connection between the soil inside the embankment and the environment outside the embankment to drain water under unsaturated conditions.

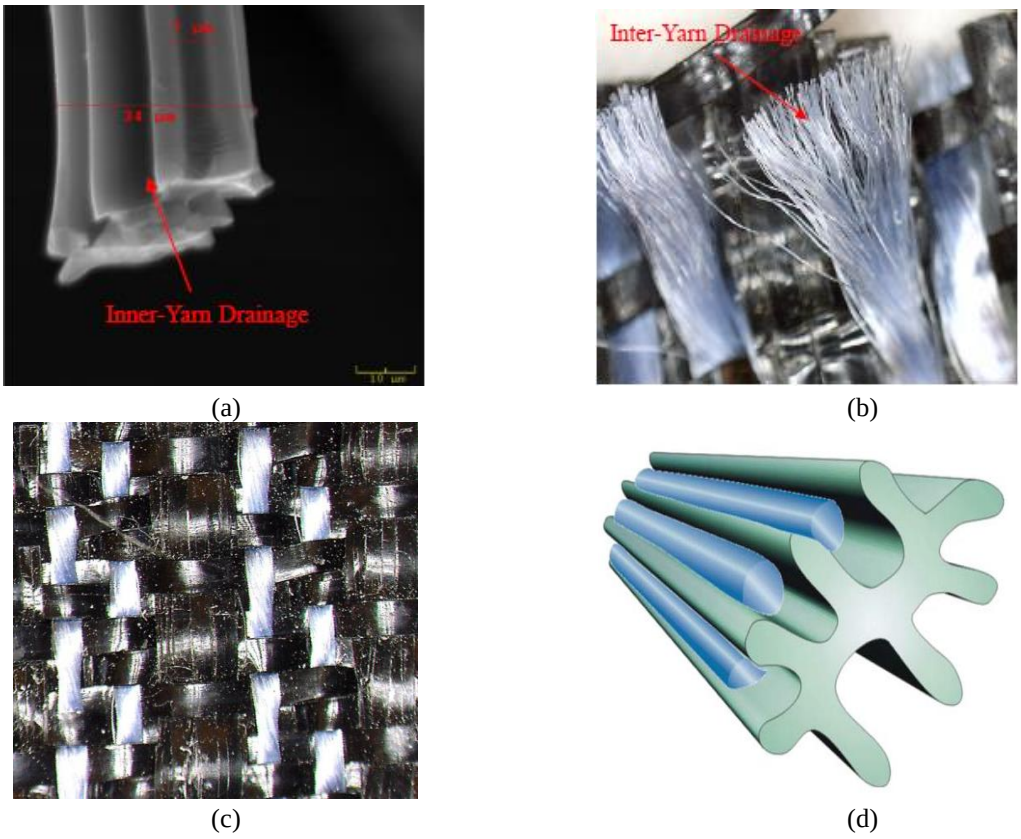

Figure 2.6 Geotextile with wicking fabric

Table 2.1 H2Ri geotextile specifications

Physical Properties		**Unit**	**Typical Value**
Roll Dimensions (width × length)		ft (m)	15×300 (4.57×91.4)
Roll Area		$yd^2(m^2)$	500 (418)
Mechanical Properties	**Test Method**	**Unit**	**Average Roll Value**
Tensile Modulus @ 2% Strain (CD)	ASTM D4595	kN/m	657
Permittivity	ASTM D4491	Sec^{-1}	0.24
Flow Rate	ASTM D4491	$L/min/m^2$	611
Pore Size (O50)	ASTM D6767	microns	85
Pore Size (O95)	ASTM D6767	microns	195

Apparent Opening Size (AOS)	ASTM D4751	mm	0.43
			Tested Value
Wet Front Movement (24 minutes)	ASTM C1559	inches	6.0 Vertical Direction
Wet Front Movement (983 minutes) Zero Gradient	ASTM C1559	inches	73.3 Horizontal Direction

Figure 2.7 shows a conceptual drainage design that implements the geotextile with wickability. A layer of this geotextile is installed at the bottom of the base layer, and 1 to 2 m of the material is exposed to the atmosphere at both sides of the embankments. Due to its hydrophilic and hygroscopic nature, the wicking fabric can absorb water from the surrounding soils inside the embankment. As discussed previously, the suction gradient induced by the RH difference provides the driving force that wicks water out of the pavement structure to the embankment, where finally the water vaporizes at the exposed surface via evaporation. Unlike the granular or conventional geotextile drainage system, the new geotextile builds a liquid connection between the inside of the pavement structure and the outside for continuous water removal even under low RH (high suction) conditions. Compared with the amount of water needed to saturate earth's atmosphere, the amount of water in pavement structure is very small. Therefore, the surrounding air provides an unlimited driving force, and the wicking process continues until soil near the wicking fabric is dry and cannot provide sufficient water supply. With the geotextile installed, the pavement's post-compaction water content is expected to maintain at optimum level or decrease to a lower level. As long as the pavement water content is controlled at a relatively low level, soil stiffness will be ensured at the designed value, and rutting depth will remain within an acceptable range. Thus, the pavement's long-term performance is improved.

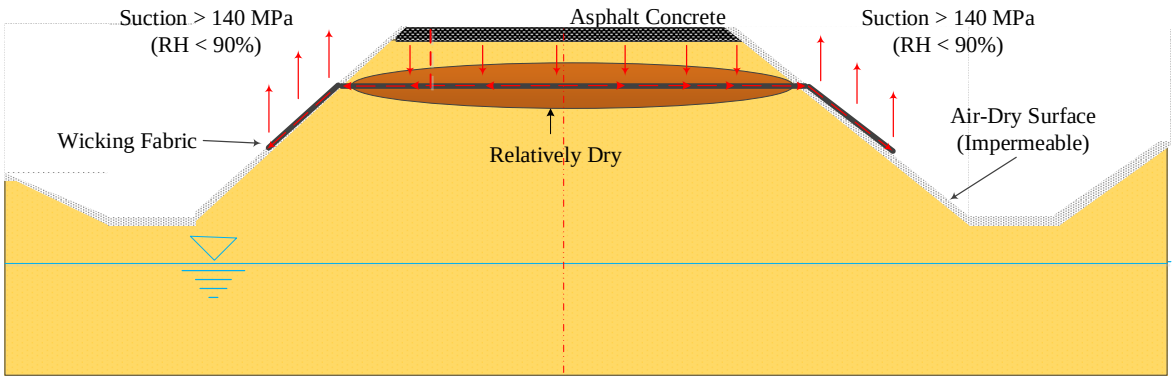

Figure 2.7 Conceptual drainage design

Researchers at the University of Alaska Fairbanks (Zhang and Presler 2012) conducted a series of tests, including a drainage test, capillary rise test, rainfall infiltration test, and frost heave test, to evaluate the effectiveness of this geotextile in controlling frost heave problems. Test results of four different types of geotextile confirmed that the geotextile has advantages at wicking water out of soil under unsaturated conditions.

Wang et al. (2015) evaluated the effectiveness of the geotextile's wicking ability under unsaturated and rainfall conditions. To simulate field conditions, a layer of the innovative geotextile was sandwiched by a 152 mm thick AB-3 base course and a 381 mm thick subgrade, mixed with Kansas River sand and Kaolinite. The geotextile extended from the closed system to the dehumidifier section so that water could be wicked out. A total of 11.3 kg of water was poured into the system to simulate a 38.1 mm/hour rainfall, and the water content with depth was monitored. Test results indicated that the geotextile effectively wicked water out of soils compacted at optimum water content, and the water wicked out by the geotextile was 1.65 times greater than that drawn by gravity. Therefore, lab test results provide evidence that this type of geotextile has the potential to wick water out of soils under unsaturated conditions and is competitive in that respect with other types of geotextiles.

Although laboratory test results indicated that H2Ri shows promise as a drainage material for wicking water from pavement structure, no direct evidence was available to prove good field performance. In addition to lab test results, several reports and papers were found regarding the wicking performance of this innovative geotextile as discussed in the following cases.

Case 1: Beaver Slide, Alaska

Zhang et al. (2014) reported successful application of the H2Ri geotextile to prevent frost boils in Alaska pavements. Application was made at a section of the Dalton Highway named Beaver Slide, an unpaved road with significant heavy truck traffic. Frost heave and thaw weakening had caused extensive damage to the pavement structure. Previous rehabilitation with geocomposites had proved unsuccessful. Twenty-two TDR sensors were used to monitor the temperature and water content change of an approximately 18 m long road section, where the most soft spots had been observed the previous summer. Two layers of the geotextile were installed 45 cm apart. Test results over 5 years of monitoring indicate that H2Ri geotextile has successfully eliminated the "frost boil" issue. Field observation shows a clear difference in the road surface for sections with and without geotextile. No soft spot was observed during early spring season, and soil at the shoulders was damp, indicating that water flowed along the direction of the H2Ri geotextile. The H2Ri geotextile successfully eliminated frost and thaw weakening to a depth of 1.1 m, which could be considered an effective depth or functional range of the H2Ri geotextile's wickability. Even though excess water was found in soil 1.2 m beneath the surface, it was beyond the depth affected by frost heave and thaw weakening and had limited effect on roadway performance.

Case 2: Coldfoot, Alaska

Frost heave problems similar to the problems at Beaver Slide occur about 30 miles north of Coldfoot, Alaska. The extremely cold temperatures and ice-rich soil adjacent to the roadway worsen the road's frost heave problem. A 19 km test section (9.5 km with H2Ri geotextile and 9.5 km without) aimed at mitigating frost heaving and preventing ice lens formation was constructed in 2012. One lane with 0.3 m of aggregate over the geotextile was completed first. The other lane was built using the same structure with a minimum of 0.15 m geotextile overlap. Test results showed that the application of H2Ri geotextile was successful at preventing water from rising to the subgrade via capillary action. Since this test section is relatively new, close monitoring is required to evaluate overall roadway performance over time. Preliminary observation, however, indicates the geotextile's effectiveness as a capillary break to wick water out of the pavement structure.

Case 3: St. Louis County, Missouri

The objective of this project in St. Louis County, Missouri, was to use the H2Ri geotextile to remove water from underneath the pavement section of a new bridge being constructed over the Missouri River. The original design was to construct a pavement section with 10 cm of base aggregate, 10 cm of drainable aggregate, and a prepared subgrade. It was expected that the geotextile could reduce the aggregate base material by 5 cm and be able to wick water from under the pavement. Observation indicates that the geotextile successfully wicked the water out of the aggregate.

Case 4: Texas County, Texas

Zornberg et al. (2013) discussed several cases involving the innovative geotextile in pavement construction and rehabilitation projects. One of the applications was the Texas State Highway 21 rehabilitation project to control differential settlement in expansive clay subgrades. The testing area included 8 sections with 4 different types of separator geotextile. Unfortunately, there were no conclusive results indicating the effectiveness of the innovative geotextile to change the water content in subgrades, possibly because of the high plasticity of the subgrade soil (Plasticity Index = 35%). Another case mentioned in Zornberg et al. (2013) was in Lecheria, Mexico, where a pavement section was constructed over a high plasticity clay embankment. A wicking fabric geotextile was used in this project to reduce differential settlement of the plastic clay by balancing the non-uniform distribution of moisture and reinforce the base course of the road section. Wicking fabric geotextile was placed on top of the subgrade soil to decrease the vertical flow of water and dissipate water in the horizontal direction. The geotextile was also designed to reinforce the base layer, so that the thickness of the base layer would be a minimum of 38 cm. The performance of these sections is currently being monitored.

Case 5: Corona, California

In Corona, California, a large section of roadway was affected by an excessive amount of runoff, which saturated the roadway and ultimately caused it to fail. The geotextile with wicking fabric was provided to help drain away the excess water while providing enhanced stabilization. A 15 cm layer of base material was placed on top of the geotextile, followed by a layer of geogrid and another 15 cm of base material. A 10 cm layer of asphalt concrete was the final element of the design to complete the road section. Observation indicated that the geotextile

provided superior tensile strength at low strain for subgrade support, separated the natural subgrade soils from the aggregate base, wicked excess water, and provided lateral confinement for the base section.

Case 6: Jefferson County, Wisconsin

Another application occurred at Jefferson County, Wisconsin, where the geotextile was used to solve a differential settlement problem. The primary challenge was the presence of wet and saturated silt and peat deposits to depths exceeding 10 m beneath the existing pavement. Simply removing the deposits was not an economically feasible solution. The geotextile was placed directly on the exposed subgrade, followed by a 0.38 m lift of crushed stone, a single layer of geogrid, and a 0.38 m lift of crushed stone. The Jefferson County Highway Department reported that subgrade undercutting was minimized to about 0.8 m, compared with a potential 1.5–1.8 m (or more) undercut for the soil conditions present. In addition to the cost savings, a substantial time savings in the project's construction schedule was achieved.

2.5 Potential Issues and Concerns

Although preliminary laboratory and field test results indicate that the application of the new geotextile is promising, some questions regarding the use of the wicking fabric for more general conditions remain unanswered. For example, what is the working mechanism of the soil-geotextile system that drains water out of the pavement structure laterally? To what extent can pavement structure water content be reduced? By implementing this type of geotextile, how much improvement in the pavement structure can be obtained in terms of resilient modulus, permanent deformation, and shear strength along the soil-geotextile interface? Most importantly,

will the geotextile stop working at a certain point (similar to the breakthrough suction of a capillary barrier)? If yes, at what condition?

The objective of this study was to better understand and demonstrate the mechanism of this type of geotextile to remove water and improve the performance of pavement structure. The objective has been achieved by having comprehensively characterized the mechanical and hydraulic properties of the geotextile, the soils, and soil-geotextile system interaction. By establishing the relationship among different parameters such as water content, suction, resilient modulus, permanent deformation, and soil-geotextile interactions, theoretic analyses have been performed and the benefits of implementing the geotextile have been analyzed.

One of the issues is that of excessive compaction introduced during construction and installation. Will compaction cause permanent deformation or mechanical failure? During the geotextile's service life, will dynamic traffic load cause additional deformation that impedes the geotextile's drainage efficiency? Will other factors such as aging, clogging, and salt concentration influence the geotextile's long-term performance? The potential issues have been examined and evaluated via microscopic analyses of SEM images of lab and field samples.

CHAPTER 3.0 MATERIAL CHARACTERIZATIONS

3.1 Soil Properties

Since this project was collaborative (University of Kansas and University of Alaska Fairbanks [UAF]), the tested soil from Kansas was shipped to UAF to maintain the consistency of the test results. The sieve analysis indicated that the selected soil was Aggregate Base Class 3 (AB-3), according to AASHTO T27-99. Figure 3.1(a) shows the sieve analysis test result. The uniformity coefficient (Cu) and the coefficient of gradation (Cc) were 54.7 and 4.1, respectively. The fines content was about 8.5%, and the liquid limit and plasticity index of the fines material were 20 and 7, respectively. Therefore, the fine-grained soil was classified as CL-ML based on the plasticity chart. Figure 3.1(b) gives the modified Proctor test results, according to ASTM D1557. The optimum water content and maximum dry density were 8.5% and 2.2×10^3 kg/m^3, respectively. The raw data for sieve analysis and modified proctor test can be found in Appendix A.

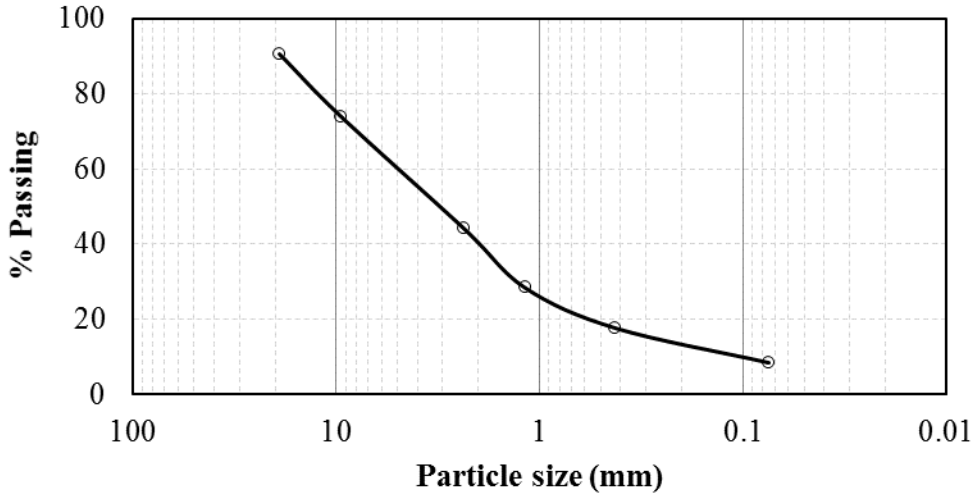

(a) Sieve analysis test result

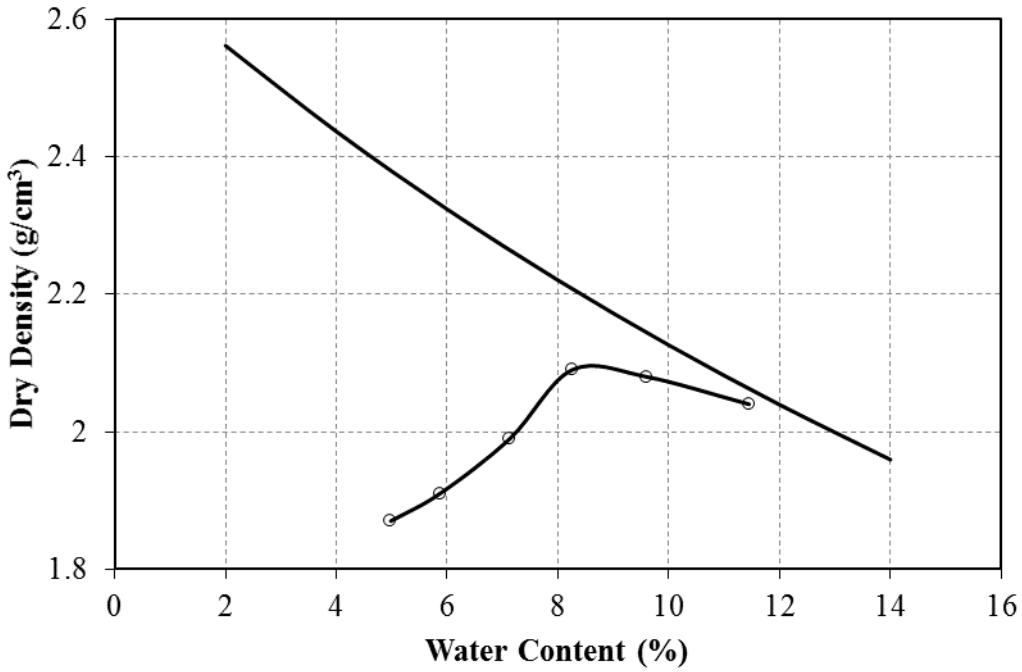

(b) Modified Proctor test result

Figure 3.1 Gradation curve and modified Proctor test

3.2 Resilient Modulus Test

The resilient modulus test is commonly used to demonstrate the dynamic performance of base and subbase materials; it is an important input parameter for the Mechanistic Empirical Pavement Design Guide (MEPDG 2004). Several factors influence the resilient modulus value of a base course material, such as stress state, moisture condition, and matric suction (Yang et al. 2008). It is obvious that the resilient modulus of base course material is affected by the stress state (both confining pressure and deviatoric stress). Detailed discussions regarding the effect of stress state on base course can be found in a series of publications (Khoury and Zaman 2004; Liang et al. 2008; Nazzal and Mohammad 2010; Nguyen et al. 2010). The focus of this study was the effect of water content on the resilient modulus of the base course. It is equally important

to take water variations into consideration during the design process because (1) the water content within a pavement structure changes seasonally, and underestimating water fluctuations of base course and subgrade will result in a non-conservative design; and (2) in many cases, most of the pavement structure is in unsaturated condition. The stiffness of a base course not only is related to soil stress state, but also is dependent on soil suction, which is closely related to soil water content.

Note that the existing MEPDG method only uses an adjustment factor, F_u, to compensate for the loss of stiffness in pavement structure induced by water variation during the pavement's service life. The Enhanced Integrated Climatic Model (EICM) uses the adjusted resilient modulus value based on water variations under different climatic and seasonal conditions. This model uses a singular design parameter, in situ or as compacted resilient modulus, rather than a water content dependent parameter. The EICM cannot represent real-time pavement stiffness and makes numerical simulation even harder when taking water content variation into consideration.

Even though the resilient modulus test is a standard test according to AASHTO T307-99 (AASHTO 1999), the purpose of this research was to conduct a resilient modulus test by covering the full water content range, from dry samples to fully saturated ones. To the authors' knowledge, little research has been performed on base course materials with such a wide range of water content. The designed water content varied from 0% to 10%, with 2% increment each time. It is well known that soils compacted at different water contents have different microstructures. From the viewpoint of unsaturated soil mechanics, these soils cannot be treated as the same. In order to eliminate the influence of soil microstructure, all soil samples were compacted at optimum water content (8.5%) to ensure that all soil specimens had the same microstructure. Next, the samples with a target water content lower than 8.5% were exposed to

open air for 15-20 minutes every day and then covered with plastic wrap until they reached the target water content. Meanwhile, the samples with a target water content higher than 8.5% were first sprayed on the surface to dampen the samples and then were covered with plastic wrap for at least 1 week to achieve uniform distribution of water content. For each target water content, three identical samples were prepared.

The resilient modulus value is obtained by performing repeated load triaxial tests on cylindrical specimens. The test equipment is shown in Figure 3.2. Vertical deformation was monitored by using two LVDTs that were mounted on circumferential rings clamped on the specimen. The load was monitored with a miniature load cell located on the loading ram outside the triaxial cell.

Table 3.1 gives the scheduled loading sequence for base course. According to the standard, sample conditioning is required to eliminate the effects of the interval between compaction and loading, and to minimize the effect of imperfect contact between the loading cap and the soil specimen. If the height of the sample still decreases after 500 repetitions, stress cycling was increased to 1000 times. For each loading sequence, the resilient modulus value, M_R, was calculated with the last five cycles in each loading sequence. After completion of the loading sequences, the quick shear test was continued at a constant axial strain rate of 1%/min and 34.5 kPa confining pressure if the total permanent strain exceeded 5%.

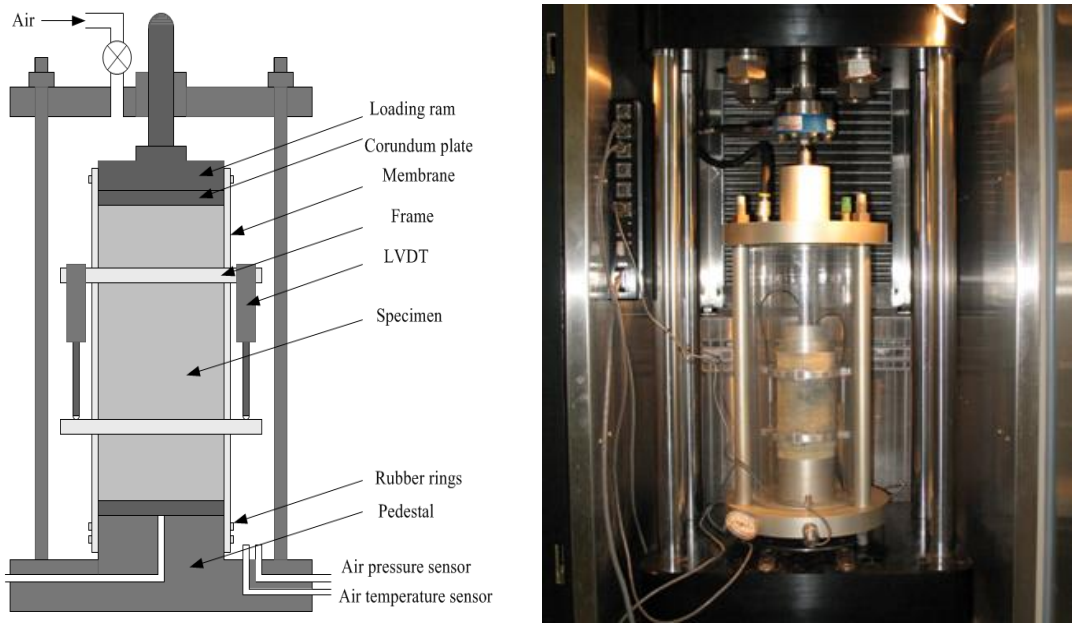

Figure 3.2 Resilient modulus test equipment

Table 3.1 Resilient modulus test loading sequence

Sequence number	Confining pressure (psi)	Deviator stress (psi)	Bulk stress (psi)	Contact stress (psi)	Loading applications
Conditioning	15	13.5	58.5	1.5	500
1	3	2.7	11.7	0.3	100
2		5.4	14.4	0.6	100
3		8.1	17.1	0.9	100
4	5	4.5	19.5	0.5	100
5		9	24	1	100
6		13.5	28.5	1.5	100
7	10	9	39	1	100
8		18	48	2	100
9		27	57	3	100
10	15	9	54	1	100
11		13.5	58.5	1.5	100
12		27	72	3	100
13	20	13.5	73.5	1.5	100
14		18	78	2	100
15		36	96	4	100

Figure 3.3(a) shows the resilient modulus test results. The resilient modulus values decreased with increment of water content. Samples with 10.8% water content were too soft to survive the conditioning process, and vertical permanent strain exceeds 5%. These results indicate that even if the base course is compacted at optimum water content, as long as post-compaction water content exceeds 10.8% and bulk stress is greater than 300 kPa, permanent deformation of the base course will cause significant rutting and deterioration of the pavement structure. The resilient modulus was not sensitive to the variations of confining pressure and deviatoric stress when the sample water content was smaller than 4%. For samples with 2.1% water content, the resilient modulus only varied from 944 kPa to 1156 kPa when the deviatoric stress increased from 37 kPa to 248 kPa and confining pressure increased from 20.7 kPa to 137.9 kPa. Similar results held for samples with 3.8% and 0% water content. In contrast, water content variation was a more predominant factor affecting the resilient modulus. When the deviatoric stress and confining pressure were fixed, the resilient modulus decreased by 10 times when water content varied from 10.8% to 0% (confining pressure 137.9 kPa and deviatoric stress 248 kPa), and could be as high as 75 times (confining pressure 20.7 kPa and deviatoric stress 37 kPa). Rada and Witczak (1981) presented similar results by comparing the resilient modulus variation of granular base course 2% plus/minus the optimum water content. The resilient modulus increased by 30% (water content 2% lower than the optimum value) and decreased by 30% (water content 2% lower than the optimum value). Note that keeping the post-compaction water content at its optimum level is a more efficient and cost-effective way to maintain the base course stiffness compared with increasing the stiffness of either the base course or the geotextile.

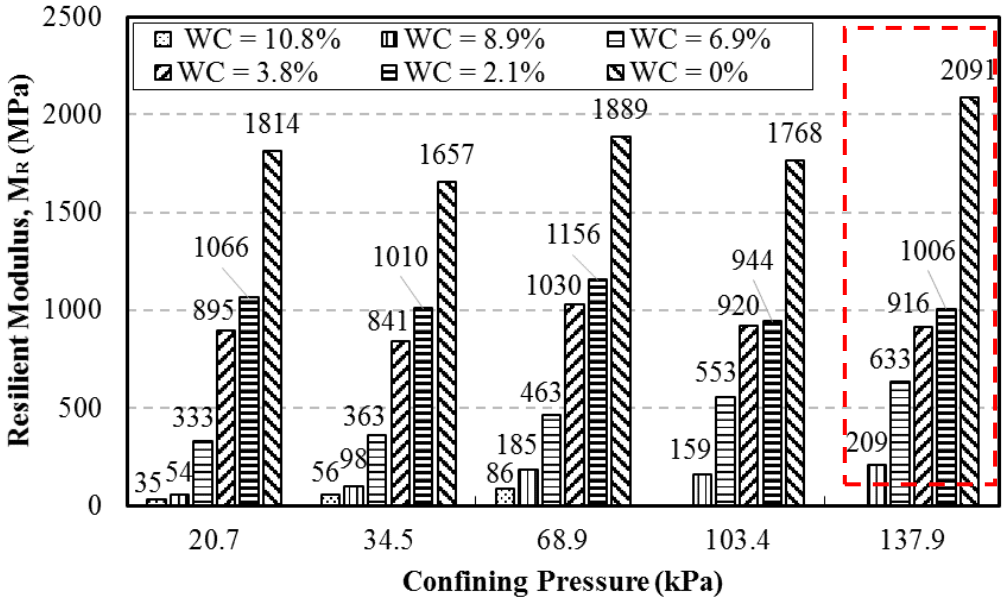

(a) Resilient modulus test results

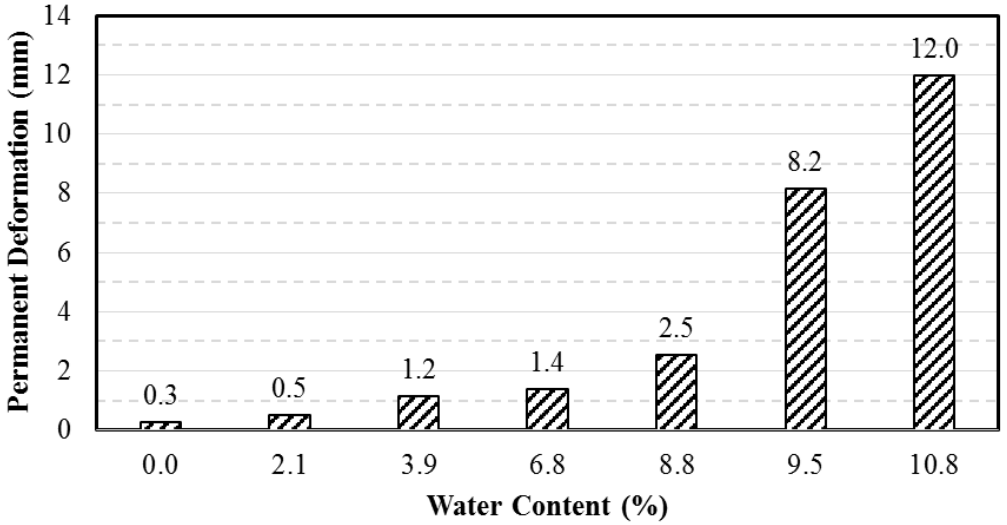

(b) Permanent deformation

Figure 3.3 Resilient modulus and permanent deformation

The following discussion concerns the field condition of the geotextile when it is placed at the bottom of the base course, which corresponds to a confining pressure of about 138 kPa (approximately 20 psi) (dashed box in Figure 3.3a). Normally, the base course is compacted

under optimum water content (8.5%) and maximum dry density (2.2 kg/m^3), but sometimes it is neither feasible nor cost effective to perform the compaction to this extent. The water content of the base course tries to reach equilibrium with ambient conditions according to the season (Yang et al. 2005). When base course contains more fines or when the groundwater table is shallow, post-compaction water content increases by 1–2%. Considering the tested soil in this study, if the post-compaction water content increases to 10.8%, the base course cannot form its own shape and the resilient modulus will be low (close to 0). If the geotextile maintains the base course post-compaction water content at optimum level, the stiffness of the base course can be maintained at the designed value (209 MPa). Furthermore, if the geotextile is effective enough to reduce the post-compaction water content by 2%, the resilient modulus can be increased to 633 MPa, which is about 3 times higher than that value at 8.5%. Combining the two cases discussed, the geotextile can theoretically increase the stiffness of the base course from nearly 0 to over 600 MPa. (This is without considering the influence of the stiffening effect).

Figure 3.3(b) gives the average permanent deformation after the resilient modulus test at different water contents. Permanent deformation tended to increase faster when the water content of the sample was greater than the optimum water content. For example, permanent deformation increased from 2.5 mm to 12 mm when water content changed from 8.8% to 10.8%. The permanent deformation exceeded the allowable value of 10.2 mm (corresponding to a vertical strain of 5%) when water content was greater than 10.8%. For comparison, permanent deformation varied from 0.3 mm to 2.5 mm when water content increased from 0% to 8.8%. Therefore, to prevent severe rutting, the post-compaction water content should not be greater than 9.5%. The raw data for the resilient modulus test can be found in Appendix B.

As a focus of this study was the effect of water content variation on the residual properties of granular soil, it was important to develop a regression model that could be used for later mathematical simulation. In the Mechanical Empirical Pavement Design Guide (MEPDG 2004), the following model is suggested:

$$M_R = k_1 p_a \left(\frac{\theta}{p_a}\right)^{k_2} \left(\frac{\tau_{oct}}{p_a} + 1\right)^{k_3} \quad (3.1)$$

where M_R = resilient modulus;

k_1, k_2, and k_3 = regression parameters;

p_a = atmospheric pressure, 101 kPa;

θ = bulk stress $\frac{1}{3}(\sigma_1 + \sigma_2 + \sigma_3)$; and

τ_{oct} = octahedral shear stress, $\frac{1}{3}\sqrt{(\sigma_1 - \sigma_2)^2 + (\sigma_2 - \sigma_3)^2 + (\sigma_1 - \sigma_3)^2}$.

This model not only accounts for the dilation effect by incorporating shear stress as one of the attributes, but also considers the confining pressure effects. The model can be used for simulating various types of soils without altering modeling parameters. The octahedral normal (or bulk) and shear stress provide a better explanation for the stress states of a material. Within the scope of this study, Equation 3.1 has been modified to incorporate the water content effects on resilient modulus values. The revised constitutive model is shown in Equation 3.2:

$$M_R = (c_1 + wc_2)p_a(\frac{\theta}{p_a})^{(c_3+wc_4)}(\frac{\tau_{oct}}{p_a} + 1)^{(c_5+wc_6)} \quad (3.2)$$

where $c_1 \sim c_6$ = regression constants, and w = water content.

The authors wanted to fit all the tested data in one regression equation, but because of the significant variation in resilient modulus values with various water contents, it was impossible to do so. Referring to Figure 3.3, permanent deformation and resilient modulus values significantly

change as water content becomes greater than 6%. Therefore, two separate equations were used for water content smaller (or greater) than 6%:

$$M_R = 6.89(5153.769 - 1110.537(6 - w))p_a(\frac{\theta}{p_a})^{(-0.1-0.23(6-w))}(\frac{\tau_{oct}}{p_a} + 1)^{0.2(6-w)} \text{ (w < 6%)}$$

$$M_R = 6.89(937.1214 - 139.102(w - 6))p_a(\frac{\theta}{p_a})^{(1.1203-0.2373(w-6))}(\frac{\tau_{oct}}{p_a} + 1)^{(-1.0330+0.7398(w-6))} \text{ (w > 6%)} \quad (3.3)$$

Figure 3.4 shows the predicted and measured resilient modulus values. For water content < 6%, the R^2 value is 0.7073, which indicates that the deviation of the regression equation is moderate. Due to the lower water content level, the soil samples are stiffer, which indicates that any eccentric loading or imperfect sample shape will cause significant deviatoric testing results. However, when water content > 6%, the R^2 value is 0.8092, much closer to the diagonal line. This phenomena indicates that the regression results are closer to the tested values.

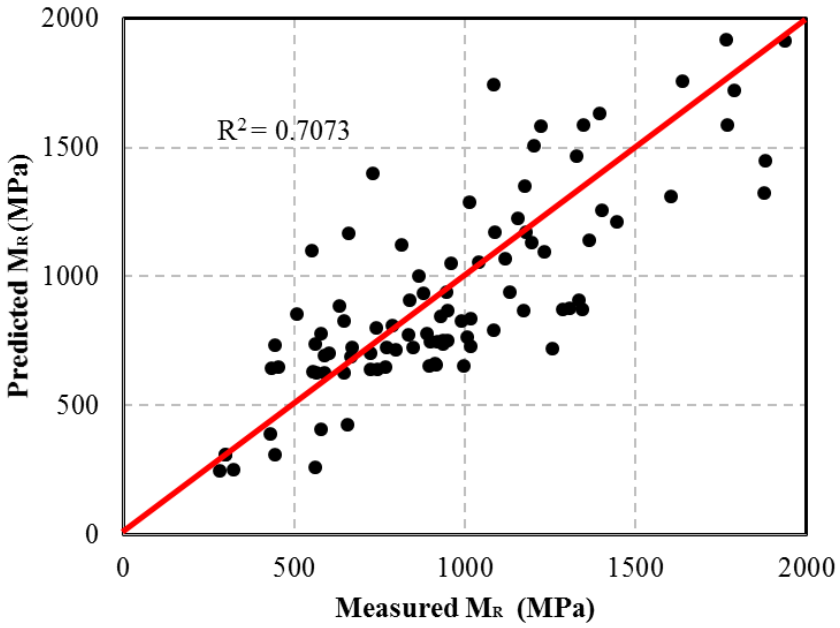

(a) Measured M_R vs. predicted M_R (water content < 6%)

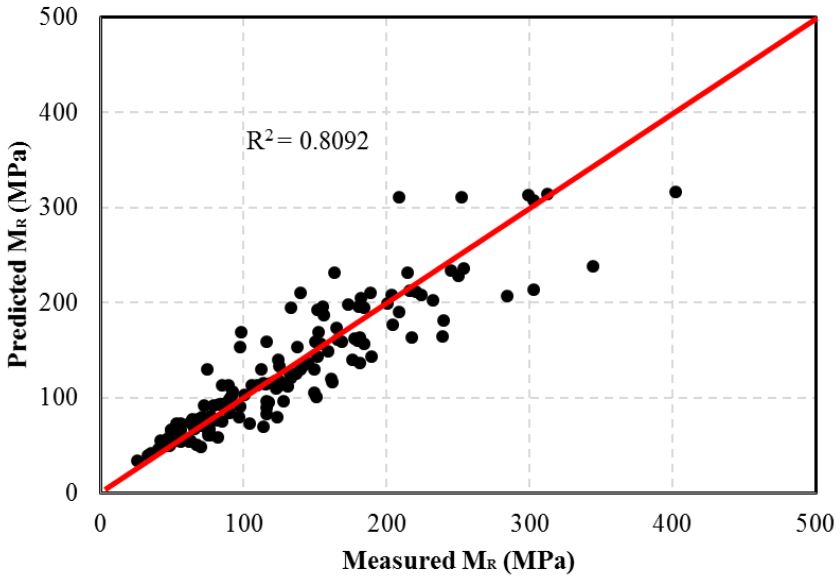

(b) Measured M_R vs. predicted M_R (water content > 6%)

Figure 3.4 Resilient modulus regression

3.3 Pressure Plate Test and Salt Concentration Test

The soil water characteristic curve (SWCC) and geotextile water characteristic curve (GWCC) depict the water content changes due to suction variation and are fundamental components of the characterization of the hydraulic properties of an unsaturated soil and geotextile. The hydraulic properties of an unsaturated soil are relevant to the amount of water stored and released within the soil pores. The SWCC is the base of engineering practice for unsaturated soils, since it correlates to the permeability, shear strength, and volume change of an unsaturated soil (Alim and Nishigaki 2009). Similarly, woven geotextile is considered a porous material; its water retention properties are critical in evaluating its drainage efficiency and, more importantly, the equilibrium moisture profile in the embankment, as discussed in later sections.

The pressure plate test equipment is shown in Figure 3.5. The samples were first compacted using the modified Proctor test, and each compaction layer was separated with a metal plate to ensure a flat and smooth contact surface. Then each layer was wrapped with a thin layer of gauze, stacked together to form a 4 inch × 8 inch mold, and fastened with 3 O-rings at the bottom, middle, and top. For saturation, the mold was put in a bucket filled with water for at least 24 hours. The saturated samples were put into the pressure plate extractor. The pressure plate extractor drained the water out of the soil using air pressure. A period of 7 days was required for the samples to reach equilibrium. At equilibrium condition, the soil water content was measured, and the applied pressure was recorded. By conducting several replications using different pressures, the SWCC within low suction range (< 1500 kPa) can be obtained.

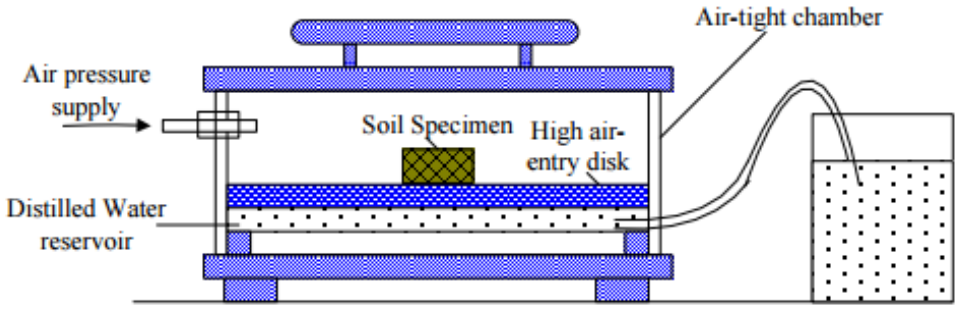

Figure 3.5 Pressure plate test for soil

However, the maximum soil particle size for the tested base course (AB-3) was about 19 mm, which made it difficult to achieve a relatively consistent pressure plate test result after several trials. It was critical to ensure good contact between the soil sample and the porous ceramic plate. Since the larger the soil particle size, the worse the contact between the soil and the porous ceramic plate, modification of the test method was required to obtain a consistent pressure plate test result. A series of papers were reviewed to evaluate the feasibility of this modification. Arya and Paris (1981) tried to apply the concept of shape similarity between SWCC and the cumulative grain-size distribution for sandy soils. Gupta and Ewing (1992) further applied the shape similarity concept to determine the SWCC of intra-aggregate pores. Recently, Fredlund et al. (2002) and Arya et al. (1999) tried to establish the relationship between

SWCC and the soil particle size-distribution curve. The grain-size distribution curve was divided into several fractions of uniformly sized particles. Knowing the arrangement of each soil particle and the volume of pores for each particle-size fraction made it possible to reduce the influence of larger particles on the SWCC. For saturated soils, water flows through the soil sample via large pores among soil particles. The permeability is dominated by the soil particle skeleton, which is closely related to the distribution of larger soil particles. However, the pores are partially filled with water when the soil is under unsaturated conditions, and the smaller pores (pores among smaller soil particles and fines) play a dominant role in controlling the soil hydraulic behavior. Even though none of the tested soils had a soil particle size larger than 4.75 mm (coarse sand), the theories behind the experiments by Fredlund et al. (2002) and Arya et al. (1999) held valid and could be applied in this study. Therefore, it was reasonable to remove the soil particles with diameters greater than sand (4.75 mm) and only conduct the pressure plate test for the rest of the soil particles. Before compacting the soil samples, the absorption capacities of the removed soil particles were determined according to the standard absorption testing method (ASTM C127 2015), as shown in Table 3.2. Then the soil was compacted with particle sizes smaller than 4.75 mm. The amount of water used for compaction should subtract the amount of water attached to the surface of the larger soil particles previously removed. When the pressure plate test was accomplished, the portion of the removed soil particles and the amount of water subtracted were added back proportionally to obtain the modified water content at this suction level.

Table 3.2 Absorption test

Sieve #	Percentage Retained (%)	AC (%)
3/4	9.48	3.49
3/8	16.54	3.53
# 8	29.84	4.58

The pressure plate test equipment for the H2Ri geotextile is the same as for the soil, as shown in Figure 3.6. However, due to the special woven texture of the geotextile, another modification was required to determine the GWCC at low suction range. For the tested geotextile, it consisted of two types of fiber yarns: one was black polypropylene yarn, which was important for reinforcement purposes and tended to repel water; the other one was white nylon yarn that had deep grooves, allowing water transport under unsaturated conditions. In the conventional test method (Figure 3.6b), the woven texture of the geotextile prevented good contact between the test samples. The water in the samples could be transported out of the system by applying air pressure. In reality, the measured water contents were higher due to such an imperfect contact area. Stormont et al. (1997) pointed out that limited data were available on the GWCC and the way in which water flowed through partially water-wet geotextiles. Knight and Kotha (2001) proposed the use of fine sand with a known SWCC and a geotextile column drainage apparatus to determine the GWCC. However, the tested geotextiles were nonwoven, thus not applicable to the woven geotextile being tested in this study. Moreover, the test method used by Knight and Kotha (2001) required additional time and effort, such as new testing equipment, knowledge of the tested sand, and the geotextile's specific gravity. Therefore, an easy, direct, and cost-effective modification was proposed by the authors, as shown in Figure 3.6(c). The H2Ri geotextile samples were sandwiched erectly in the pressure plate extractor with two plastic boards and fastened with two clamps. The bottom of the geotextile was immersed in a small amount of soil slurry (kaolin clay and water, 1:1 by weight). Care was taken so that the soil slurry was not too thick to absorb additional water from the geotextile, and not too watery to flow away. After the pressure plate test, the lower part of the geotextile, which was contaminated by the soil slurry, was cut off, and the water content of the upper part was determined.

(a) Conventional and modified test methods

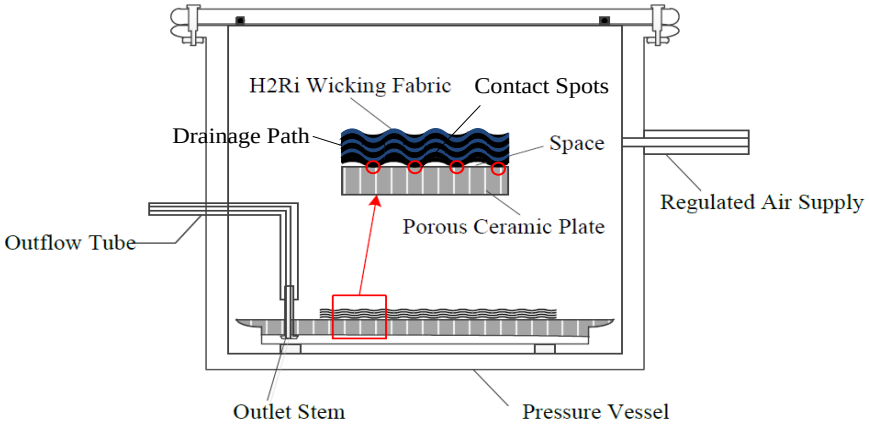

(b) Conventional test method

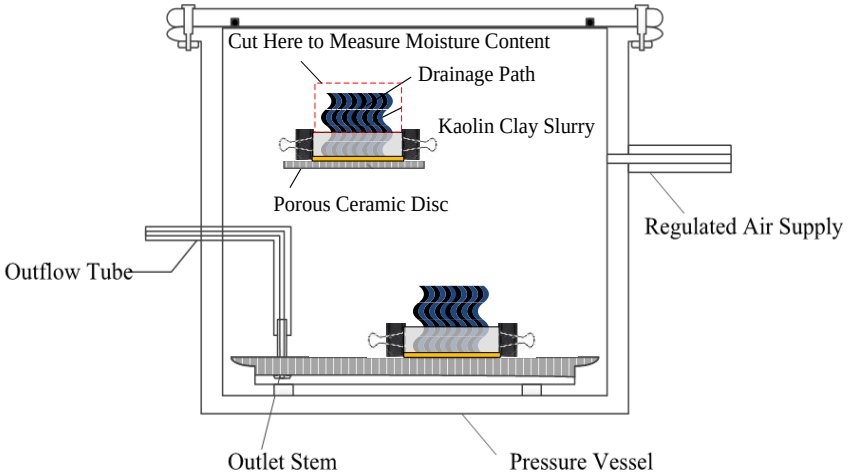

(c) Modified test method

Figure 3.6 Pressure plate test for geotextile

Unlike the pressure plate test (which measures the matric suction), the salt concentration test determines water content changes due to total suction variations. However, Fredlund and Rahardjo (1993) pointed out that matric suction is equivalent to total suction when the suction value is larger than 1500 kPa. The salt concentration test equipment for soil and H2Ri geotextile is the same, as shown in Figure 3.7. The soil samples were first compacted at optimum water content (8.5%) and then scattered to enlarge the contact area with the ambient environment, while the H2Ri geotextile samples were first saturated and cut into small pieces. Since the soil samples were scattered and no smooth contact surface was required, there was no need to remove the large soil particles. Then the samples were put into containers made of tinfoil. The bottom of each container was punched with small holes to shorten the time for reaching equilibrium. The osmotic suctions of different electrolyte solutions were adopted to calibrate the relationship between suction and soil water content (Goldberg and Nuttall 1978). The $MgCl_2$ concentrations used are shown in Table 3.3. The samples were in a desiccator for 7 days before water content was measured.

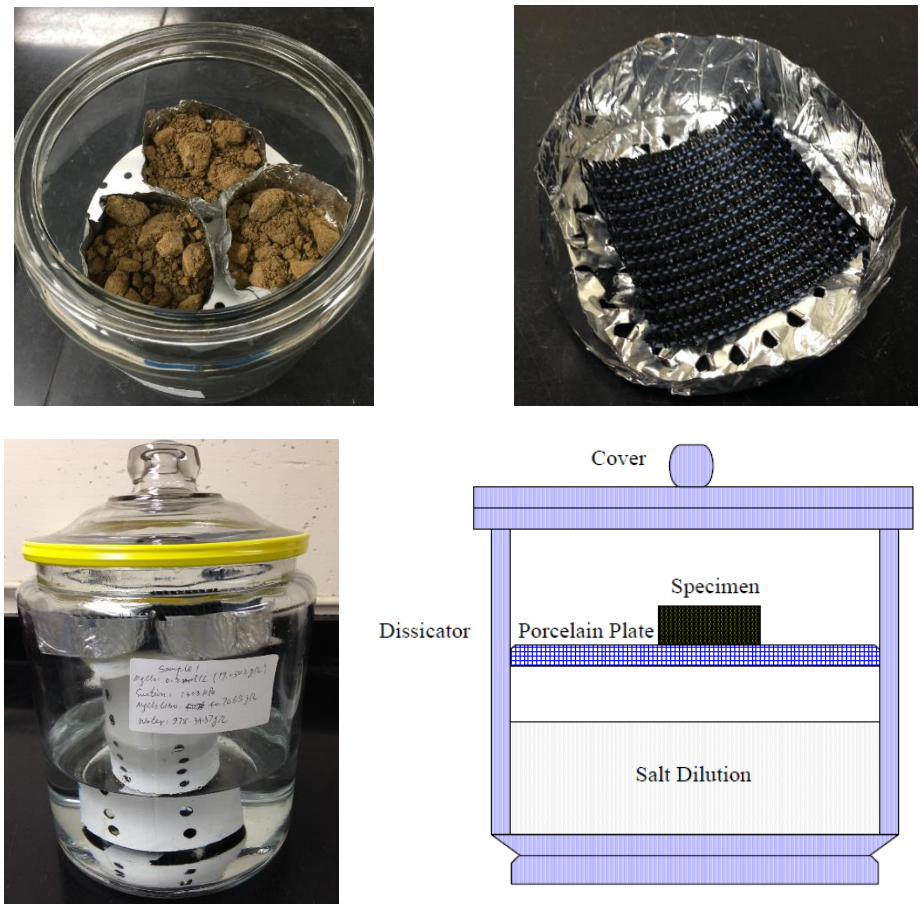

Figure 3.7 Salt concentration test

Table 3.3 Salt concentrations and corresponding suctions

Solute No.	$MgCl_2$ (g/L)	Suction (kPa)
1	19.050	1303
2	38.100	2739
3	47.626	3523
4	66.676	5244
5	95.251	8249
6	142.877	14554

Figure 3.8 shows the test results for the SWCC (dash line) and GWCC (solid line) in semi-log scale. Regarding the SWCC, several critical points need to be discussed first. The air

entry value is the suction at which air starts to enter the pores in the soil. The residual water content is defined as the large suction that needed to remove the additional water out of the soil (Fredlund and Xing 1994). Three stages are identified within the SWCC: the boundary effect stage, the transition stage, and the residual stage. The boundary effect stage ranges from full saturation (zero suction) to the value of suction at air entry where soil is essentially saturated. Within the transition stage, increasing suction causes decreasing water content until the start of the residual stage. At the residual stage, further increases in suction only result in a small reduction in water content. The suction at the beginning of the slope in the drying phase is called the air entry value, which is critical in describing the soil drainage behavior. At suctions greater than the air entry value on the drying path, air starts to intrude into the media and the water content decreases with increasing suction.

The saturated water content for soil was 12.5%. Based on test results, the regression curve could be obtained according to Genuchten's equation (1980). The expression is:

$$w = c\left[\frac{1}{ln\left[2.718+(\frac{S}{a})^{n}\right]}\right]^{m} = 0.125\left[\frac{1}{ln\left[2.718+(\frac{s}{2.352})^{1.241}\right]}\right]^{0.412} \quad (3.4)$$

where w = soil water content;

c = fitting parameter closely related to saturated water content;

a = fitting parameter closely related to air entry value;

n = fitting parameter closely related to the slope of the fitting curve;

m = fitting parameter closely related to residual water content; and

s = suction.

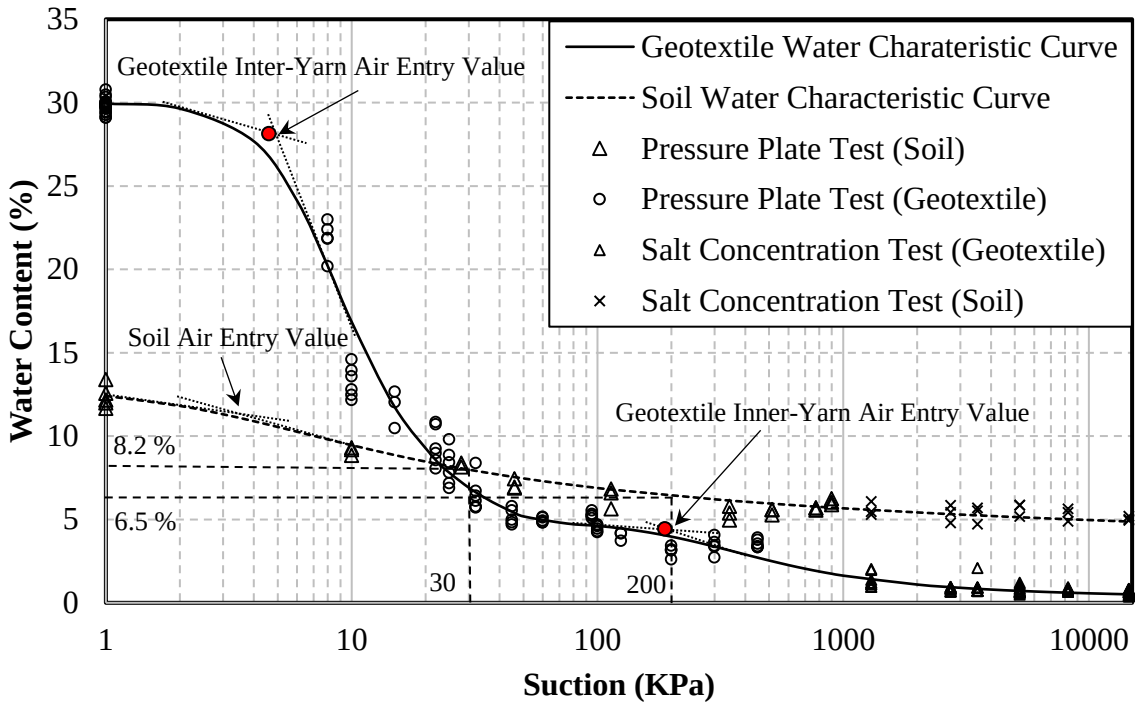

Figure 3.8 SWCC and GWCC

Similar to SWCC, the GWCC depicts the relationship between H2Ri geotextile water content and suction. The design of structures containing soils and H2Ri geotextile layers requires an understanding of how fluids flow through the permeable geotextile media. There are two types of drainage paths in the H2Ri geotextile, as discussed in Chapter 2 (see Figure 2.6); a simple regression curve similar to SWCC is not adequate to demonstrate the relationship between water content and suction in a geotextile. It is reasonable to divide the GWCC into two components: one curve describes the combined wicking effect of both inner- and inter-yarns. When the suction value has reached the inter-yarn air entry value (6.7 kPa), the inter-yarn stops working as a drainage material. Starting from this point, the inner-yarn dominates the GWCC shape until suction reaches the inner-yarn air entry value (200 kPa). Following this assumption, the GWCC curve can be expressed as follows:

$$w = 0.30 \times \left[\frac{1}{ln\left[2.718+\left(\frac{s}{6.7}\right)^{2.837}\right]}\right]^{1.006} \quad \text{(suction < 45 kPa)}$$

$$w = 0.30 \times \left[\frac{1}{ln\left[2.718+\left(\frac{s}{200}\right)^{1.732}\right]}\right]^{1.174} \quad \text{(suction > 45 kPa)} \qquad (3.5)$$

where w = geotextile water content, and s = suction.

The raw data for the SWCC and GWCC can be found in Appendix C.

3.4 H2Ri Geotextile Air Entry Value Determination

As discussed in the previous section, the H2Ri geotextile air entry value is important since it dominates the hydraulic behavior of the geotextile and determines when the geotextile will cease working. Even though the GWCC has given the air entry value, the value is based on the regression equation and may deviate from the real condition. Therefore, it is better to develop a direct testing method to determine the geotextile air entry value.

Figure 3.9 shows the schematic plot of the testing equipment for determining the geotextile air entry value. The tensiometer includes three parts: a pressure transducer, a ceramic disc, and housing. The housing was designed and precisely machined with thread inside to incorporate with the thread on the pressure transducer. A platform inside the housing, on which the stainless steel ring rests, was used to provide a gap between the ceramic disc and the transducer diaphragm. Due to the presence of this gap, empty room space was generated and used as a water reservoir. A ceramic disc with an air-entry value of 15 bar was used as a filter to prevent air from entering the water reservoir. The entire testing system was modified from consolidation testing equipment, as shown in Figure 3.9. A layer of geotextile is sandwiched by two layers of silt (Fairbanks silt). The top layer of soil is fixed with a cutting ring, and the bottom layer of the soil is on the upper part of the base. The tensiometer is placed at the center of the

lower part of the cell base, and contact between the tensiometer and the soil must be ensured to obtain a good test result. The testing system is covered with a layer of plastic wrap, and only part of the geotextile is allowed in the open air for water evaporation. If the air entry value of either the geotextile or the soil is obtained, the soil-geotextile drainage efficiency will be impeded and the suction reading from the tensiometer will be closer to a constant value. Due to the weaving structure of the geotextile, it is difficult to ensure good contact between the tensiometer and the geotextile. Yet, if the soil-geotextile system is in equilibrium, the suction in the soil will be the same as in the geotextile. Therefore, the suction in the soil can be considered the suction in the geotextile.

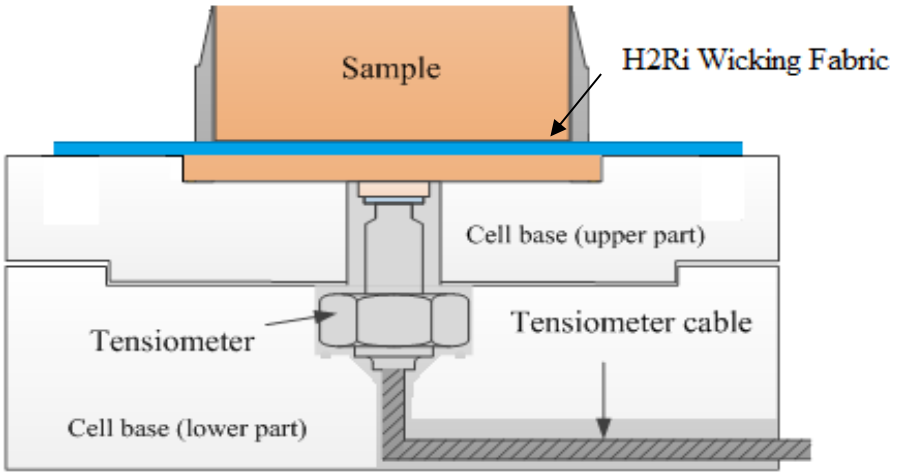

(a) Schematic plot of testing equipment

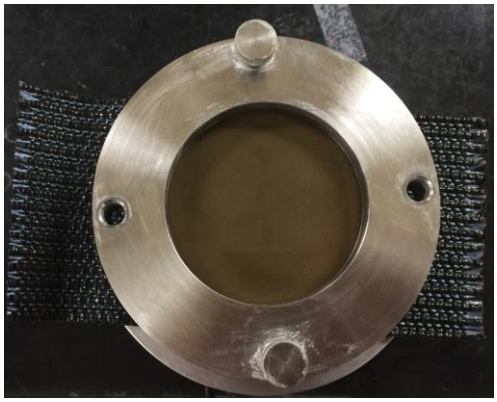

(b) Top view

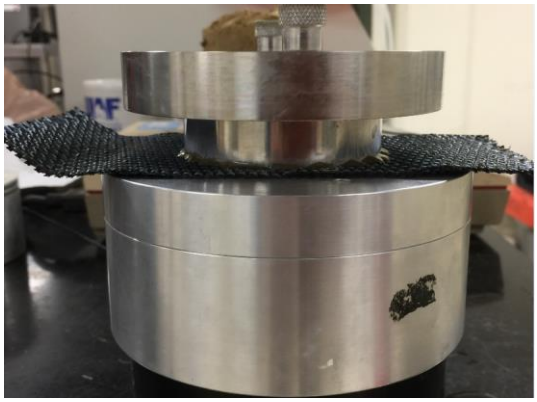

(c) Front view

Figure 3.9 Geotextile air entry value testing equipment (from Lin 2015)

Figure 3.10 shows the test results. In total, three tests were performed, including two water content level (50% and 75%) tests and two stress state (without loading and 150 kPa deviatoric loading) tests. Comparing Tests 1 and 2, the two curves have large overlapping sections, indicating that the initial water content does not have a large impact on suction variation. Both curves indicate a short period with relative constant suction (between 11 and 15 kPa). This value might be the geotextile air entry value, but no other evidence proves this assertion. Moreover, the regression curve in Figure 3.8 indicates that the geotextile air entry value is approximately 5-6 kPa, smaller than the result obtained from this test. After 40 hours,

the suction decreasing rate significantly decreases till the end of the test. Comparing Tests 1 and 3, the deviatoric load only accelerates the water seepage rate and does not influence the final suction value at equilibrium. For Test 3, the suction tends to be a constant value of 39 kPa after 30 hours. The validity of this testing method needs further evaluation, since the soil-geotextile system will stop working when either the air entry value of the geotextile or soil is obtained. The air entry value of silt can be very low if its plasticity is low. Unfortunately, Fairbanks silt is classified as low plasticity silt (ML), which makes the authors' conclusion even more vulnerable. Therefore, further study is needed in this area.

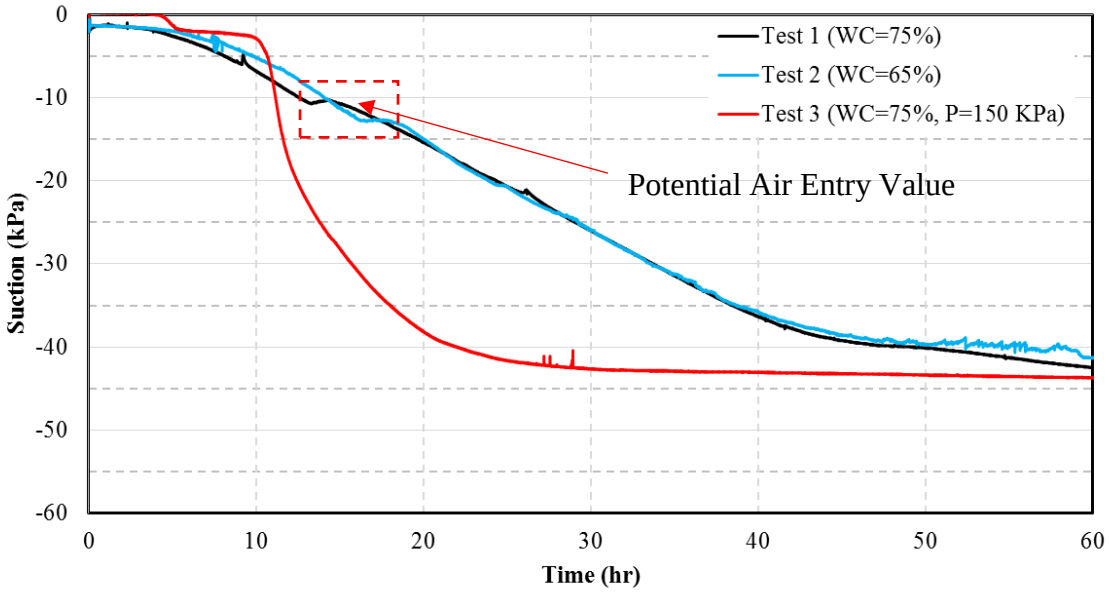

Figure 3.10 Air entry value test results

3.5 Unsaturated Soil Hydraulic Conductivity

It is often difficult to directly measure the hydraulic conductivity of unsaturated soils. Attempts have been made to correlate unsaturated soil and geotextile hydraulic conductivities with the SWCC and GWCC. In order to determine unsaturated soil hydraulic conductivity, the

constant head test was performed to determine the saturated hydraulic conductivity of the soil. The soil was first compacted using the modified proctor test. The compacted dry density was 2.18 g/cm^3. The sample was then saturated for at least 1 day before performing the constant head test. The testing equipment is shown in Figure 3.11. The reservoir was used to provide the constant water head, and two manometers were used to measure the water head before and after passing through the soil sample. A 500 ml beaker was used to collect water ouflow, and a timer was used to determine the corresponding time. In total, three replicates were conducted to determine the hydraulic conductivity and the average value as 1.406×10^{-4} m/s.

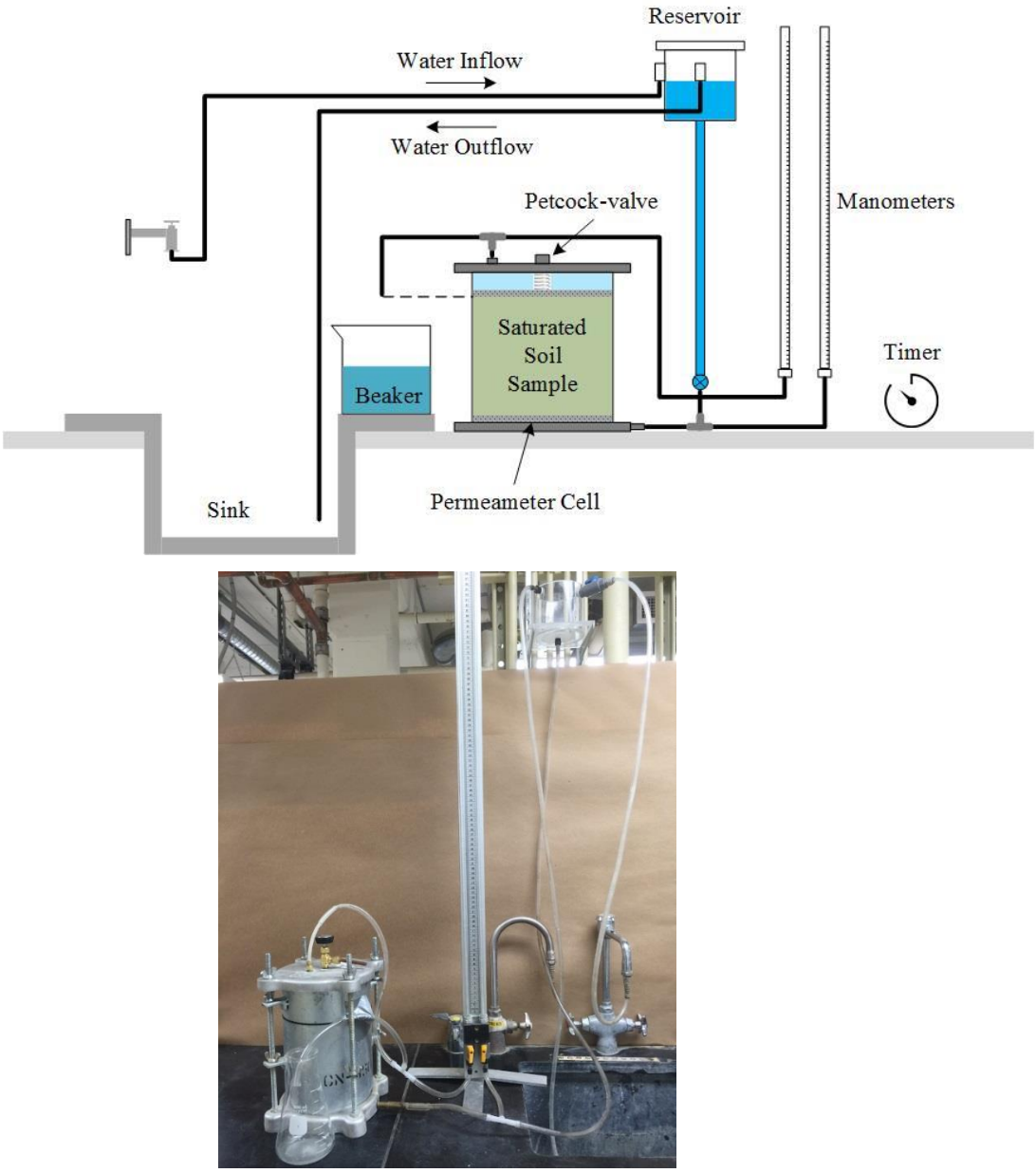

Figure 3.11 Constant head test

The SWCC was used to compute unsaturated hydraulic conductivity. The SWCC was first divided into 20 equal intervals (with 20 midpoints) of water content based on maximum and minimum water content. The first water content corresponds to saturated conditions. Each

midpoint corresponds to a particular suction. The hydraulic conductivity function is in accordance with the following equation (modified from Kunze et al. 1968):

$$k_w = \frac{k_s}{k_{sc}} A_d \sum_{j=1}^{m} \{(2j + 1 - 2i)(u_a - u_w)_j^{-2}\}$$
$$i = 1, 2, \cdots, m \quad (3.6)$$

where k_w = predicted hydraulic conductivity for a water content w_i (corresponding to the ith interval) (m/s);

i = interval number which increases as the water content decreases;

j = a counter from "i" to "m";

m = total number of intervals between the saturated water content and the lowest water content on the SWCC curve (for our case, m = 20);

k_s = measured saturated hydraulic conductivity (for our case, $k_s = 1.406 \times 10^{-4}$ m/s);

k_{sc} = saturated coefficient of permeability (m/s); and

A_d = adjusting constant.

The term $\sum_{j=1}^{m}\{(2j + 1 - 2i)(u_a - u_w)_j^{-2}\}$ describes the shape of the hydraulic conductivity curve, and the term A_d is used to scale the coefficient of permeability function. Based on the regression Equation 3.6, the relationship of unsaturated soil hydraulic conductivity with suction variations is shown in Figure 3.12. Unsaturated hydraulic conductivity decreases dramatically with each increment of suction value. Within engineering applications, when the soil has a hydraulic conductivity lower than 10^{-11} m/s, the soil itself can be considered an impermeable material. At this stage, the suction is about 120 kPa, which explains how the hard crust on the surface of an unpaved road is formed. Recall that atmospheric suction can easily be over 140 MPa, and the unsaturated hydraulic conductivity of a relatively dry surface can be

much lower than 10^{-11} m/s, cutting off the water (vapor) exchange within and outside the roadway. Moreover, base course in the embankment is under unsaturated conditions in most cases, and its hydraulic conductivity is low in most cases, which impedes water transport within the road structure. Since all existing drainage design methods are mostly based on soil saturated hydraulic conductivity, the actual drainage ability of soils above the groundwater table (base, subbase, and part of subgrade) may be lower than expected in most climatic conditions (except for on rainy days).

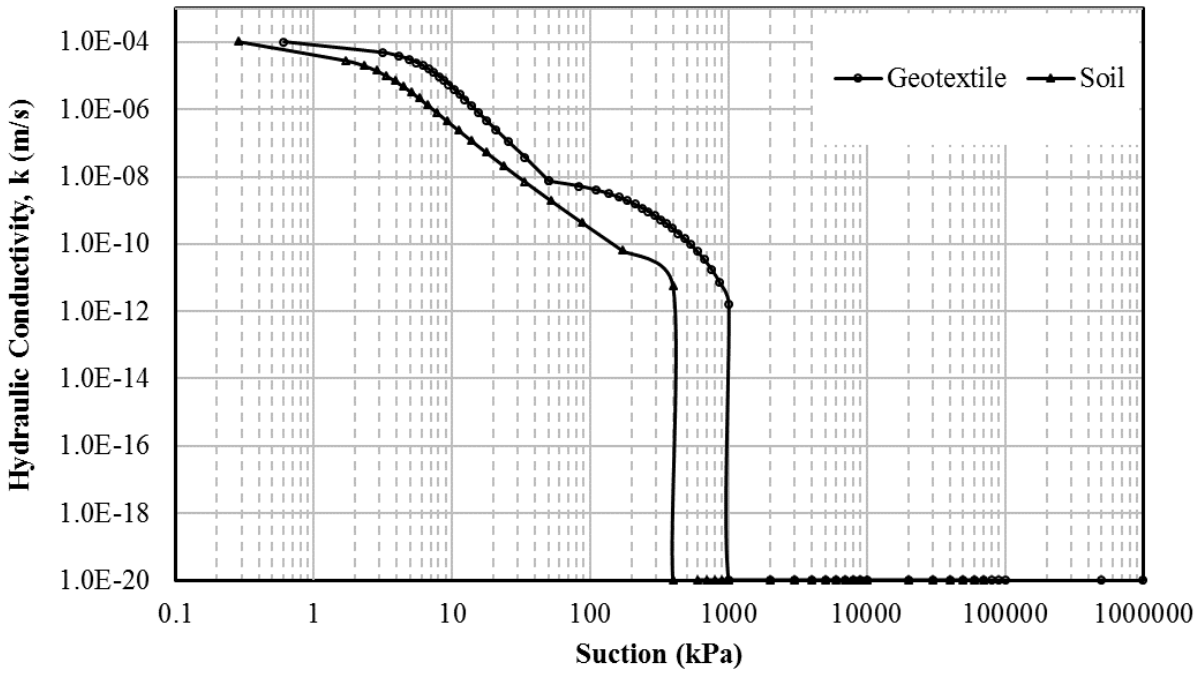

Figure 3.12 Unsaturated hydraulic conductivity

As for the unsaturated hydraulic conductivity of H2Ri geotextile, the derivation process is the same. However, due to the special multichannel cross-section structure, the GWCC has been divided into two parts by the inter-yarn air entry value. Therefore, the unsaturated hydraulic conductivity of the H2Ri geotextile needs to be separated, and each section should be treated

with the same deriviation method discussed above. Figure 3.12 also shows the relationship between the suction and hydraulic conductivity of the H2Ri geotextile. Two nonlinear curves are observed and are always greater than the soil hydraulic conductivity under the same suction level. This indicates that as long as the soil-geotextile system fuctions (theoretically when suction < 200 kPa), a higher unsaturated hydraulic conductivity of geotextile ensures that the water moves from the surrounding soil to the geotextile multichannels. The H2Ri geotextile hydraulic conductivity is higher than 10^{-11} m/s until suction reaches 1000 kPa. However,when suction is larger than 200 kPa, the slope of the curve increases and the hydraulic conductivity decreases dramatically. Therefore, H2Ri geotextile drainage efficiency will be significantly reduced when suction is greater than 200 kPa. In sum, as long as the H2Ri geotextile fuctions, it has the ability to continuously suck water from the surrounding soil and wick it out of the roadway.

3.6 Large Direct Shear Test

The confinement and reinforcement functions of a soil-geotextile system largely rely on the interface shear strength. A large friction-shear machine was used to evaluate the sensitivity of the shear strength of the soil-geotextile system to water content change. The shear box was composed of two parts (upper and lower shear box) with dimensions of 300 mm × 300 mm × 75 mm, as shown in Figure 3.13. Vertical and horizontal displacements were measured by digital indicators with outputs for data acquisition. Side friction was measured by suspending (floating) the upper (stationary) half of the shear box on load cells using threaded rods. The shear-friction force was developed by hydraulic cylinders at a rate of 6 mm/min. The test was performed according to ASTM D5321/D5321 M-14, Standard Test Method for Determining the Shear

Strength of Soil-Geosynthetic and Geosynthetic-Geosynthetic Interfaces by Direct Shear (ASTM D5321 2014).

(a) Shear box

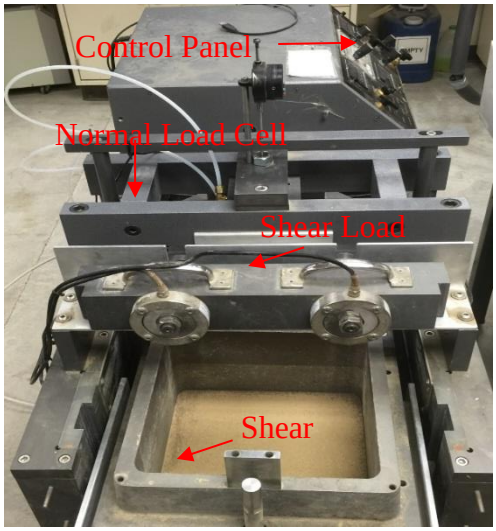

(b) Top view

Figure 3.13 Large-scale direct shear test equipment

Large-scale direct shear test results are shown in Figure 3.14. Similar to the resilient modulus test, the water contents changed from 0% to 10.5% (dry to saturation condition) with a 2% increment. Since the tested soil was AB-3 aggregate, cohesion could be ignored for all samples. The frictional angle, φ, first increased with the increment in water content and then

decreased as water content kept increasing. For such a wide range of water content change, the maximum and minimum frictional angle were 47.5° and 39.4°, respectively. When soil was in dry condition, no pore water pressure existed in the soil voids so that the friction angle represented the interface friction angle between geotextile and dry soil. Yet, for soil samples with 2% water content, soil was in unsaturated condition and voids were partially occupied with water. Suction (or negative pore water pressure) developed and served as additional confining pressure that held soil particles together (reinforcement effect). Therefore, the frictional angle was larger than that compared with the dry sample. When the water content of the soil sample kept increasing, more water was detained in the soil voids and suction decreased as the water content increased, resulting in reduced reinforcement and a smaller frictional angle. In sum, the interface frictional angle was not very sensitive to water content variation. The raw data of the large-scale direct shear test can be found in Appendix D.

Fredlund et al. (1995) has provided a method to predict the shear strength of unsaturated soil via SWCC. The shear strength contribution due to matric suction is primarily through the water inter-aggregate contact area. As there is little change in water content of soil below the air entry value, suction as a stress-state variable is as effective as net normal stress in mobilizing the shearing resistance along all the contact area points, as shown in Figure 3.15. This indicates that φ^b is equal to $\varphi`$. In contrast, when above the air entry value, the contribution of shear strength by suction decreases with the desaturation of the soil and results in a nonlinear variation of shear strength with respect to suction. When suction value continues to increase, the water content does not change rapidly and the contribution of water content to unsaturated soil shear strength

can be neglected. Therefore, there is a strong correlation between the shear strength behavior of unsaturated soil and the SWCC.

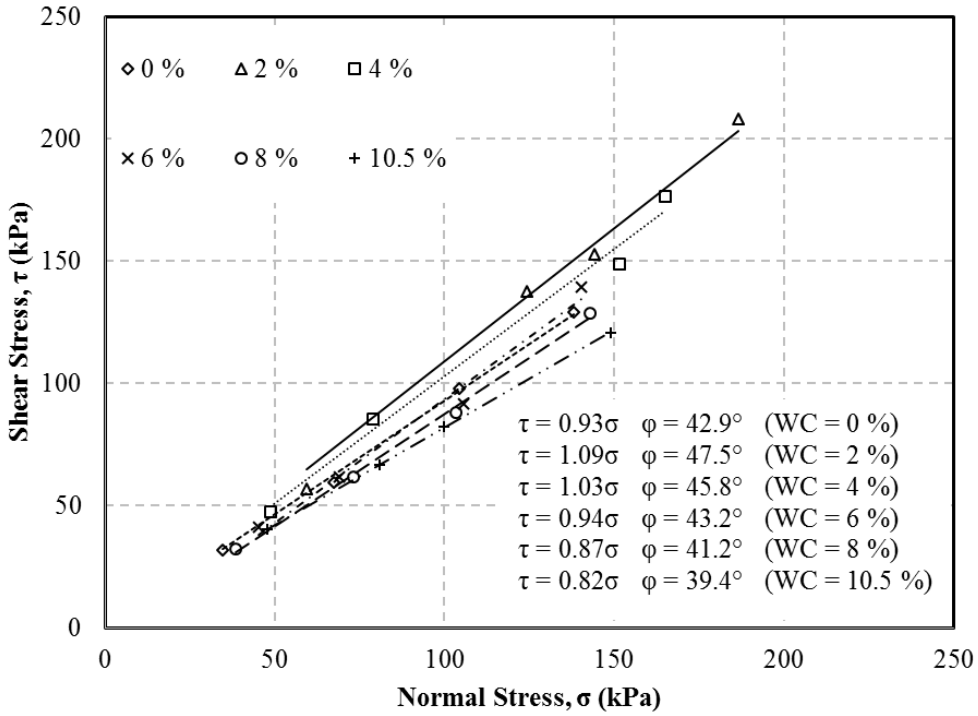

Figure 3.14 Large direct shear test results

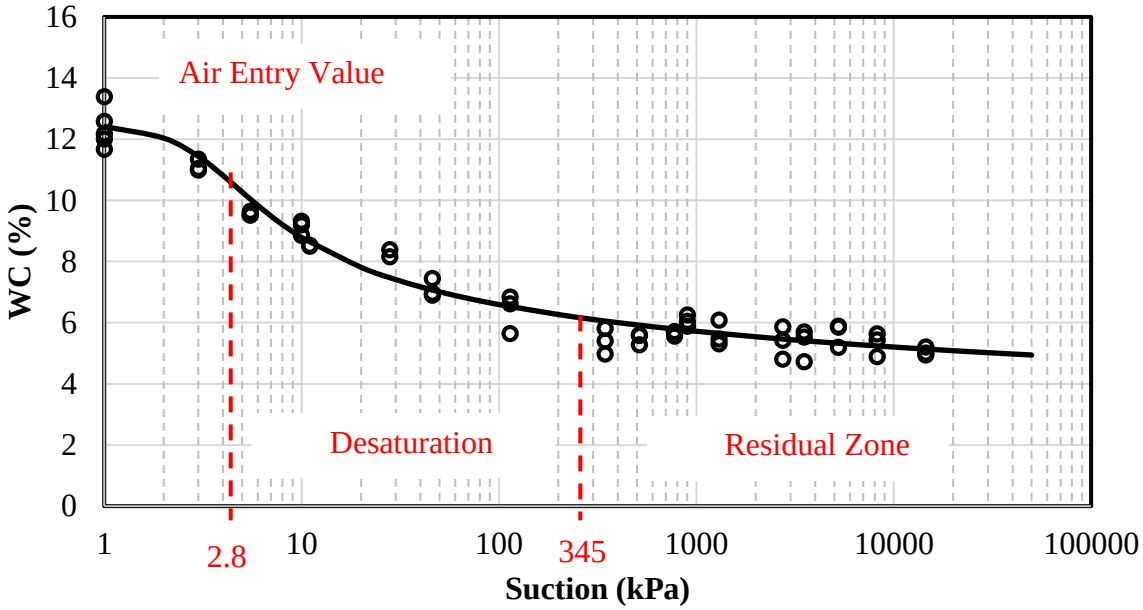

Figure 3.15 Determining shear strength from a SWCC

Unlike saturated soils, the shear strength of unsaturated soils can be described in terms of two stress-state variables: net normal stress and matric suction, shown as:

$$\tau_f = c' + (\sigma_{nf} - u_{af})tan\varphi' + (u_{af} - u_{wf})tan\varphi^b \quad (3.7)$$

where τ_f = shear strength;

c' = effective cohesion;

φ' = effective angle of shearing resistance;

φ^b = angle of shearing resistance with respect to matric suction;

$(\sigma_{nf} - u_{af})$ = net normal stress; and

$(u_{af} - u_{wf})$ = matric suction;

McKee and Bumb (1984) proposed that the unsaturated shear strength prediction depends on the values of residual conditions. Since residual suction has limited influence on unsaturated soil shear strength, Equation 3.7 can be modified as follows to predict unsaturated shear strength based on residual water content:

$$\tau_f = c' + (\sigma_{nf} - u_{af})tan\varphi' + (u_{af} - u_{wf})tan\varphi'(\frac{w - w_r}{w_s - w_r}) \quad (3.8)$$

where w_r = residual water content (corresponding to residual suction);

w_s = saturation water content; and

w = water content.

The regression equation for a SWCC can also be rewritten as:

$$w = 12.5(1 - \frac{\ln(1+s/345)}{\ln(1+10^6/345)})[\frac{1}{\ln[2.718+(\frac{s}{2.8})^{2.63}]}]^{0.29} \quad (3.9)$$

where w = water content, and s = suction, considered same as $(u_{af} - u_{wf})$ at high suction level.

Introducing Equation 3.9 into 3.8, the regression equation for the unsaturated shear strength of the soil can be expressed as:

$$\tau_f = c' + \left(\sigma_{nf} - u_{af}\right)tan\varphi'$$

$$+\left(\frac{12.5\left(1-\frac{\ln(1+s/345)}{\ln(1+10^6/345)}\right)\left[\frac{1}{\ln[2.718+(\frac{s}{2.8})^{2.63}]}\right]^{0.29}-w_r}{w_s-w_r}\right)\left(u_{af}-u_{wf}\right)tan\varphi' \quad (3.10)$$

Figure 3.16 shows predicted unsaturated shear strength with water content variation. As shown in the figure, the frictional angle decreases with increments in water content. The frictional angle can be used as an indicator to demonstrate the effect of reinforcement. For example, by comparing Figures 3.14 and 3.16, the frictional angle for shear strength at the soil-geotextile interface is larger than that for pure soil at the same water content level. Table 3.4 summarizes reinforcement efficiency in terms of percentage of frictional angle increment by using the H2Ri geotextile. At low water content level (2–4%), the soil-geotextile system provides a higher frictional angle due to additional geotextile reinforcement and confinement resulting from suction (negative water pressure). The frictional angle never increases over 10%, and the efficiency never increases higher than 3%, except when water content is between 2% and 4%. Therefore, it can be seen that the soil-geotextile system provides very limited frictional angle (shearing reinforcement) improvement, and the effect of water content on soil-geotextile unsaturated shear strength is low.

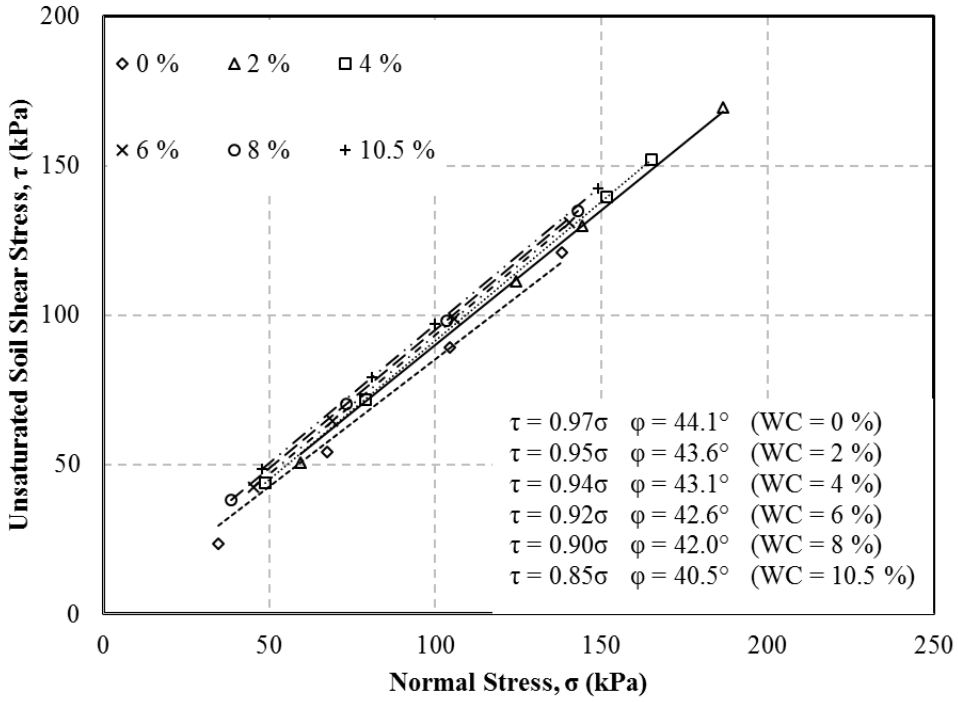

Figure 3.16 Predicted unsaturated soil shear strength at different water content levels

Table 3.4 Soil-geotextile system reinforcement function efficiency

Water Content	Frictional Angle		
	Soil	Soil-Geotextile Interface	Reinforcement Efficiency
%	°	°	%
0	42.9	44.1	2.80
2	43.6	47.5	8.94
4	43.1	45.8	6.26
6	42.6	43.2	1.41
8	41.2	42	1.94
10.5	39.4	40.5	2.79

CHAPTER 4.0 GEOTEXTILE WORKING MECHANISM AND POTENTIAL ISSUES

4.1 H2Ri Geotextile Working Theoretical Range

In considering both the SWCC and GWCC in Figure 3.8, two questions need to be answered before extensive application of H2Ri geotextile: (1) what is the working mechanism of the soil-geotextile system to laterally transport water, and (2) at what condition will the H2Ri geotextile stop working? As for the working mechanism of H2Ri geotextile, two types of drainage paths transport water within the H2Ri geotextile wicking yarns (as shown in Figure 2.6a and b), one being the voids between yarns, namely the inter-yarn drainage path, where small soil particles and air bubbles easily intrude into the drainage path. Figure 3.8 shows that the air entry value for inter-yarn drainage is low, only 6.7 kPa based on the regression curve. In reality, the suction in open air is about 140 MPa, which is much higher than the air entry value of the inter-yarn drainage path. Water can be easily transported or evaporated via the H2Ri geotextile surface. A small suction variation (from 6.7 kPa to 45 kPa) will result in significant H2Ri geotextile water content decrease (from 30% to 5%); therefore, air can easily intrude and block the inter-yarn drainage path. This drainage path is not the dominant factor that controls the hydraulic behavior of the H2Ri geotextile under unsaturated conditions. When suction is greater than 45 kPa, the degree of saturation for the H2Ri geotextile further decreases. The H2Ri geotextile is under unsaturated condition until the air entry value of the inner-yarn drainage path is obtained (200 kPa). The inner-yarn drainage path refers to the deep grooves that have an average spacing of 5 microns to 12 microns. Soil particles and air bubbles cannot easily infiltrate the drainage path with such a small opening. Within this suction range (45 kPa to 200 kPa), the

transmissivity of the H2Ri geotextile decreases significantly, but the deep grooves remain saturated and continuously wick water out of the pavement structure. When suction further increases and surpasses 200 kPa, air bubbles intrude into the multichannels of the deep grooves. The geotextile can no longer transfer any amount of water, and the H2Ri geotextile theoretically stops working. Therefore, the theoretical functional range of the geotextile in transporting water is 0-200 kPa.

The air entry value for soil is about 2.3 kPa, which is even smaller than the H2Ri geotextile inter-yarn air entry value. Since maximum soil particle size is about 19.6 mm, it is expected that the pore size between soil particles will be larger and the air bubbles will easily intrude into the pores. The water content variation is not as large in the geotextile, changing from 12.5% (saturation condition when suction = 0 kPa) to 4.9% (dry condition when suction = 15,000 kPa).

4.2 Soil-Geotextile System Working Mechanism

Combining the SWCC and GWCC provides a comprehensive understanding of the interaction between the geotextile and soil to laterally transport water out of the pavement structure. Capillary water exists in the soil pores above the saturation zone. However, unlike water vapor, capillary water can flow under the action of surface tension. The height of capillary rise is a function of the size of soil micropores, which relates to soil particle-size distribution and density. Since capillary water cannot be drained out by gravity, the most common way to control capillary water is to lower the water table or use a capillary barrier, which blocks the upward capillary flow.

The hydraulic head consists of three components: the gravitational head, z; the pressure head, $\frac{u_w}{\gamma_w}$; and the velocity head, $\frac{v^2}{2g}$, expressed as follows:

$$h = z + \frac{u_w}{\gamma_w} + \frac{v^2}{2g} \tag{4.1}$$

where h = hydraulic head;

z = gravitational head;

u_w = pore water pressure;

γ_w = unit weight of water;

v = flow rate of water; and

g = gravitational acceleration.

The velocity head in a soil type is negligible compared with gravitational and pressure heads, and if the position of a water table is considered as the datum, Equation 4.2 can be simplified as:

$$h = z + \frac{u_w}{\gamma_w} \tag{4.2}$$

Then consider the one-dimensional Laplace equation for water flow:

$$\frac{d^2h}{dz^2} = 0 \tag{4.3}$$

Integrate from both sizes, and Equation 4.3 becomes:

$$h = c_1 z + c_2 \tag{4.4}$$

where c_1 and c_2 = constants relevant to boundary conditions.

Consider the boundary condition for soil at the groundwater table: $h = z = 0$, then $c_2 = 0$. Combining Equations 4.2 and 4.3 gives:

$$c_1 z = z + \frac{u_w}{\gamma_w} \tag{4.5}$$

Moreover, in time, the water in the pavement structure tends to reach a steady state, which indicates:

$$\frac{dh}{dz} = c_1 = 0 \tag{4.6}$$

Therefore, the maximum capillary rise within the pavement structure under equilibrium can be determined, and Equation 4.5 becomes:

$$z = -\frac{u_w}{\gamma_w} \tag{4.7}$$

Water in the granular base course materials in a pavement structure cannot be drained out using a conventional granular drainage system, which relies on the influence of gravity to drain water. Usually the generated differential water head is less than 30 kPa, and the maximum capillary rise for a pavement structure is about 3 m. The blue line in Figure 4.1(a) indicates the suction distribution for pavement without H2Ri geotextile. The pore water pressure beneath the groundwater table is positive, and above, the groundwater table (suction) is negative and linearly related to the distance from the datum. As indicated in Figure 4.1(b), when the suction value is equal to 30 kPa, the water content of the H2Ri geotextile and the soil is 8.06% and 8.47%, respectively. In this circumstance, the resilient modulus value is 292 MPa, and the permanent deformation is expected to be 2.29 mm. As discussed before, those values underestimate the post-compaction water content. In other words, if the water content in the pavement structure continues to increase, the resilient modulus value can further decrease and the permanent deformation will increase.

For comparison, a discussion on pavement implemented with H2Ri geotextile follows. Since the theoretical geotextile functional range is 0-200 kPa, the geotextile can be expected to transport the water out of the pavement structure laterally and create a relatively dry zone in the

pavement structure, as shown in Figure 4.1(a). The suction value at the H2Ri geotextile is 200 kPa, and the suction value at the groundwater table is still 0 kPa. According to Zhang et al. (2014), the effective range of the geotextile is about 1.4 m. The suction value of the soil above the geotextile is considered a constant value (200 kPa). In the long term, the H2Ri geotextile creates a relatively dry zone, and post-compaction water content is expected to be 6.4% within this area. Similarly, as shown in Figure 4.1(b), the resilient modulus value increases to 633 MPa, and the corresponding permanent deformation decreases to 1.07 mm. Compared with the previous case without geotextile (WC = 8.47%), the resilient modulus increases by 3 times and the permanent deformation decreases to half.

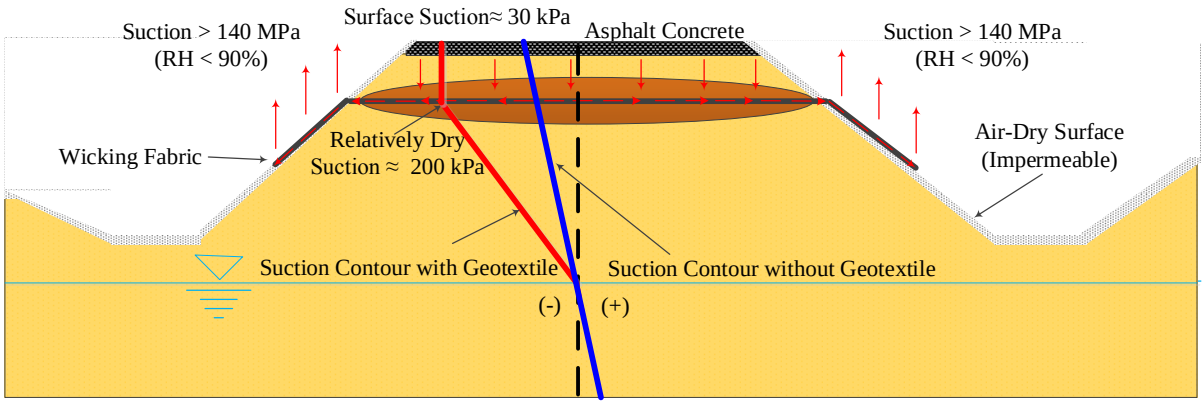

(a) Pavement structure with and without geotextile

Soil Suction (kPa)	1,000,000	1500	200	50	30	5	0
Geotextile WC (%)	0	1.28	3.97	5.18	8.06	26.4	32.5
Soil WC (%)	0	5.52	6.43	7.46	8.47	10.8	12.5
Resilient Modulus (MPa)	2089	1262	633	367	292	N/A	N/A
Perm. Deform. (mm)	0.30	0.91	1.07	1.65	2.29	12.00	N/A

(b) Test results summary

Figure 4.1 Soil-geotextile system working mechanism

The relationships among water content, suction, resilient modulus, and permanent deformation are shown in Figure 4.1(b). When the soil and geotextile are in relatively dry condition, the suction value can be higher than 100 MPa. The resilient modulus for the tested soil is as high as 2089 MPa, and the permanent deformation is limited to 0.3 mm. At the other extreme, when the soil and H2Ri geotextile are in saturated condition, the water content is 12.5% and 32.5%, respectively. In such a case, the soil is too soft to hold its own shape and the resilient modulus cannot fulfil the loading sequences. Therefore, the base course is not considered an acceptable supporting material for traffic load. Furthermore, considering the in situ condition, post-compaction water content is always 1-2% higher than the optimum value for the long run. The H2Ri geotextile has the ability to reduce the post-compaction water content 1-2% more than the optimum value. This means that the soil-geotextile system has the potential to reduce the pavement system water content by 4% in total. In other words, the resilient modulus can theoretically be increased by almost 6 times, and the permanent deformation can be reduced by

over 12 times. Zhang et al. (2014) and Lin et al. (2015b) continuously monitored the field performance of H2Ri geotextile in a test section in Alaska. After 5 years of monitoring, the soil-geotextile system has successfully eliminated frost heaving and the subsequent thaw weakening issue.

Figure 4.2 further summarizes theoretical suction, water content, and resilient modulus distributions with depth for pavement structure with and without H2Ri geotextile. For pavement structure without H2Ri geotextile, suction linearly decreases with depth, and the corresponding water content increases from 6.5% at the surface to approximately 11% at the bottom. The resilient modulus value decreases from 623 MPa at the surface to about 320 MPa at a depth of 2.5 m. In contrast, in a pavement structure with H2Ri geotextile (assuming it is implemented at 0.3 m from the road surface), suction is maintained at 200 kPa to a depth of 0.3 m, then linearly decreases to 0 at 3 m (where groundwater is encountered). The corresponding water content is maintained at 4.9% at the surface, and further increases to about 9.4% at the bottom of the embankment. The resilient modulus value is 819 MPa at the surface, and decreases to about 650 MPa at a depth of 2.5 m, which is even greater than the maximum resilient modulus value for pavement without geotextile. This indicates that H2Ri geotextile can be a promising drainage material for improving road performance by dehydrating water in the embankment.

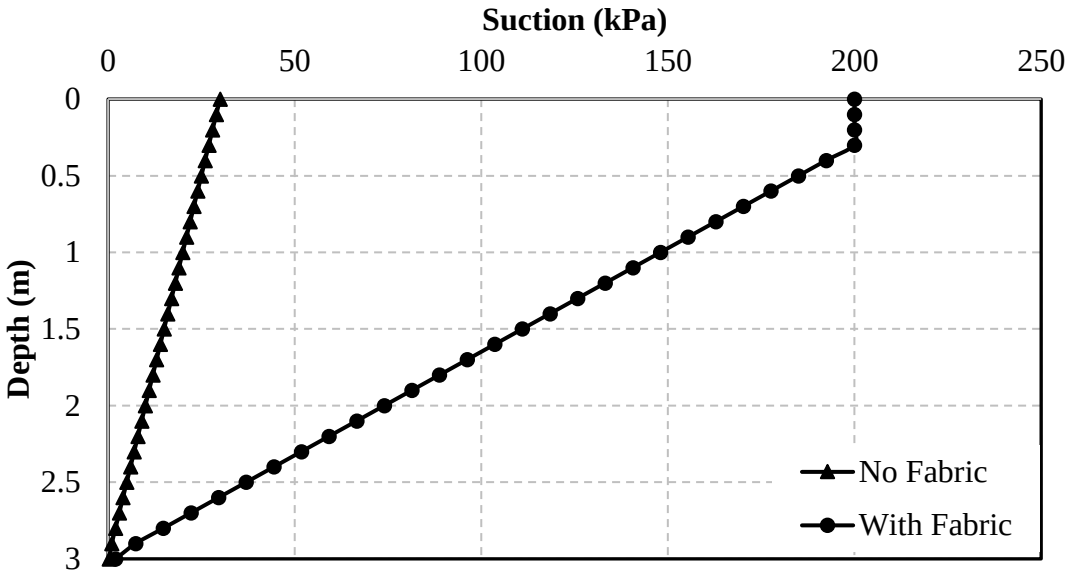

(a) Suction variation with depth

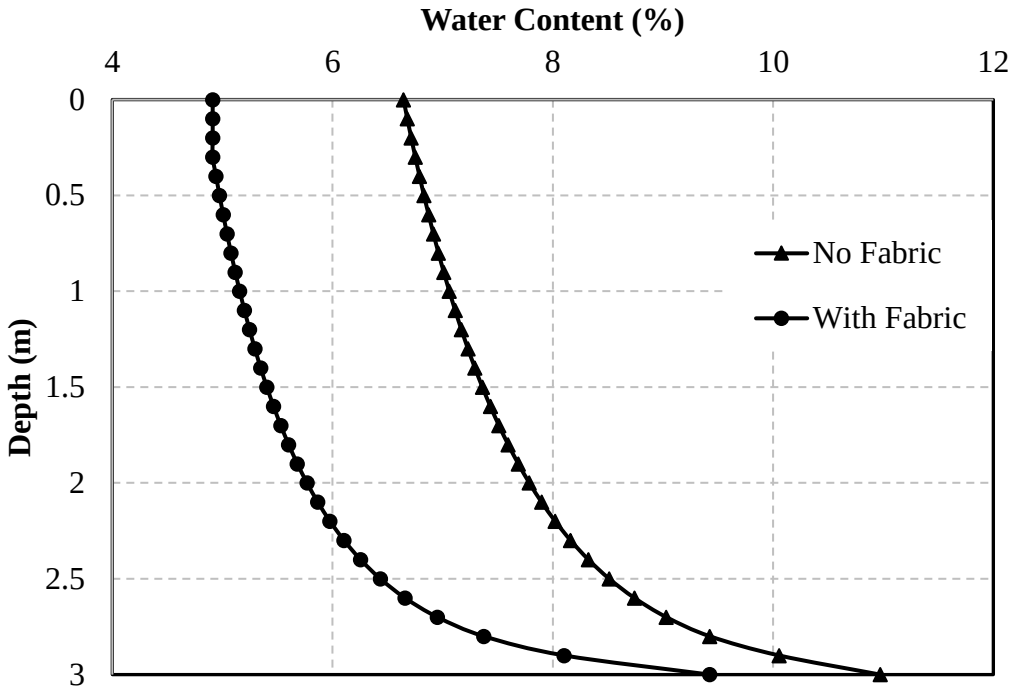

(b) Water content variation with depth

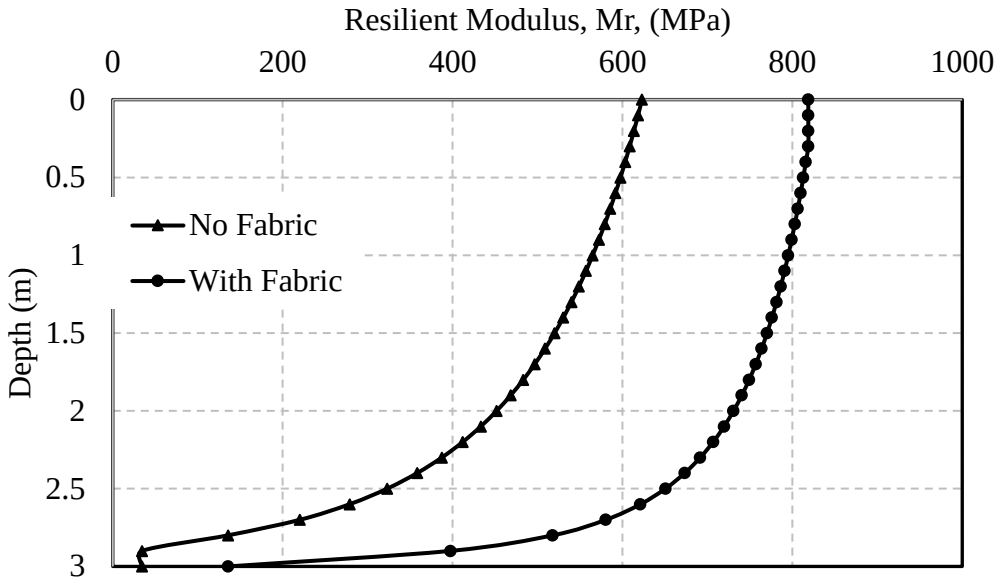

(c) Resilient modulus variation with depth

Figure 4.2 Theoretical suction, water content, and resilient modulus distributions

4.3 Potential Issues

In addition to a macroscopic study, the interaction between H2Ri geotextile and surrounding soils was investigated at a microscopic level. Field samples were collected at the edge of the embankment during a field trip in July 2015 and brought to the laboratory for further testing. A JOEL JXA-8530F Electron Microprobe was used to analyze wicking fabric microstructures. Distress in the form of permanent deformation, mechanical failure, and aging was observed in some samples. The exact cause of distress was not known, so a parallel lab test was performed at the University of Kansas to simulate the factors that could cause the H2Ri geotextile to malfunction during the construction process and under dynamic traffic load. Samples were collected and shipped to UAF to perform SEM analyses. Part of this research has been included in the previous Beaver Slide project report (Lin et al. 2015b). The major objective

of the SEM analyses was to evaluate the severity of distress, the cause(s) of permanent deformation, and the level of salt concentration. A detailed discussion follows.

Field Samples from Beaver Slide (Dalton Highway), Alaska

Clogging Effect

Figure 4.3(a) presents the woven structure of an intact sample at Beaver Slide with ×55 magnification. Large amounts of soil particles were detained on the surface of the H2Ri geotextile. Because the soil contained approximately 6% fines, the clogging effect was obvious at this level; the deep grooved drainage paths were blocked by the fines material. Figure 4.3(b) shows a closer view of the wicking fabric at the surface with ×350 magnification. This view further illustrates that the deep grooved drainage paths were completely filled with fine soil particles. In comparison, Figure 4.3(c) shows the wicking fabric just beneath the surface layer. The deep grooves beneath the surface were much cleaner than the grooves above; few particles were detained in the drainage paths. In other words, the fibers of the wicking fabric at the surface served as a protective layer, preventing the fine soil particles from penetrating deeper into the fabric structure. Figure 4.3(d) shows a comparison of the wicking fibers on the surface with the fibers just beneath the surface. Note from the figure that even though the wicking fabric fibers on the surface are filled with fine soil particles, the wicking fibers beneath the surface effectively drain water out of the pavement structure. It would be inaccurate to base an evaluation of wicking fabric clogging based on the surface fibers, since “surface” is a theoretic term and is difficult to define during an SEM analyses. If too many soil particles were left on the surface of the wicking fabric, the wicking fabric would be covered by the soil. On the other hand, if all the surface soil were removed, the evaluation of the clogging effect would not be objective. It

seemed more reasonable to evaluate the clogging effect based on the wicking fibers below the surface.

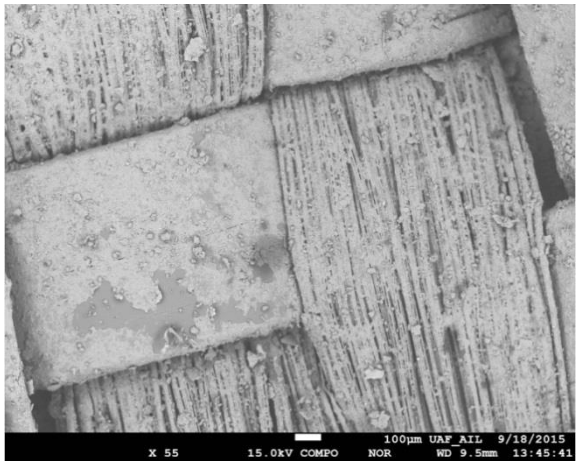

(a) Intact sample (Sample 4)

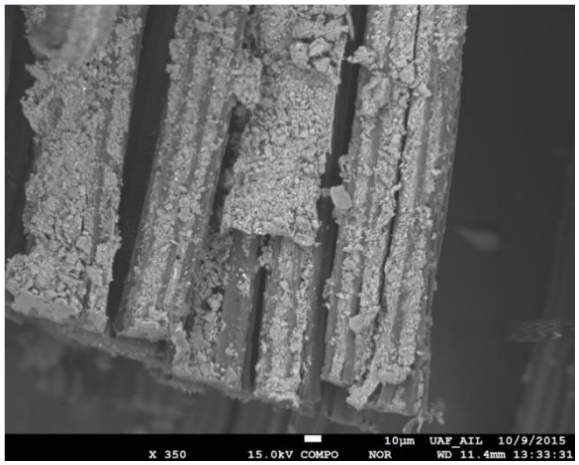

(b) Surface clogging (Sample 20)

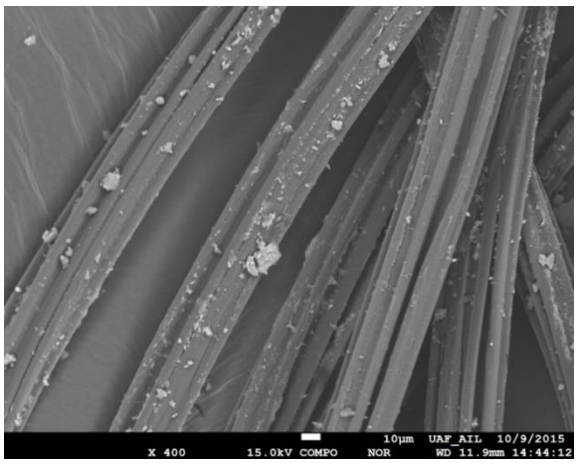

(c) Beneath surface (Sample 25)

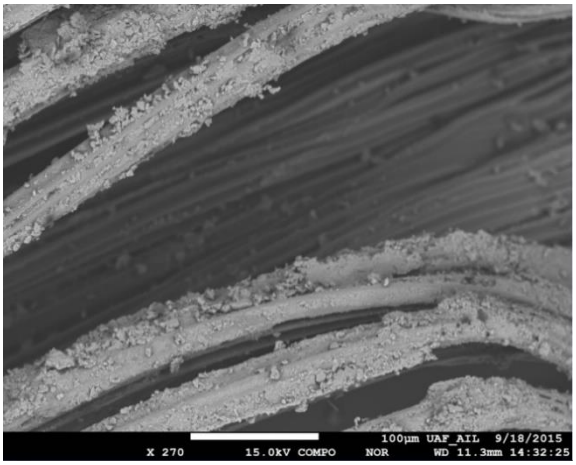

(d) Wicking fabrics comparison

Figure 4.3 SEM images of clogging effect

Permanent Deformation and Mechanical Failure

Figure 4.4 presents the SEM images of samples affected by permanent deformation and mechanical failure. Figure 4.4(a) is an image of new wicking fabric, never used before. The wicking fabric fibers under the woven polypropylene yarns already indicate permanent

deformation in the vertical direction. This deformation might have been caused by pressure applied during manufacturing, or it might have occurred during the transportation process. Figure 4.4(b) shows the image of the wicking fabric collected from the field. The permanent deformation observed in the new materials had further increased. Due to additional vertical pressure, the wicking fabric fibers were nearly flattened, and the deep grooves were unable to hold water under unsaturated conditions. Figure 4.4(c) presents the front view of the wicking fabric. Deep grooves are visible in the vertical direction and tend to close in the horizontal direction.

Another mechanical failure known as *puncturation* is illustrated in Figure 4.4(d) Puncturation refers to the puncturing of the fibers by the large or sharp soil particles that are detained on the wicking fabric surface. The large soil particles, especially those with sharp edges, act as a cutting edge that severs the deep grooves of the wicking fabric. This likely occurs due to high overburden soil pressures and dynamic traffic loads applied to the road surface, or to the compaction effort introduced during construction. The drainage paths break and are unable to continue laterally transporting water. This phenomenon was only observed in 5 out of 30 samples. According to the observed macroscopic results at Beaver Slide, it seems that neither permanent deformation nor puncturation are major concerns, possibly for two reasons: (1) a relatively low percentage of the wicking fabric had permanent deformation or puncturation, and (2) the surrounding fine soil particles might have had a “bridging effect” for water transport at locations where permanent deformation or puncturation occurred.

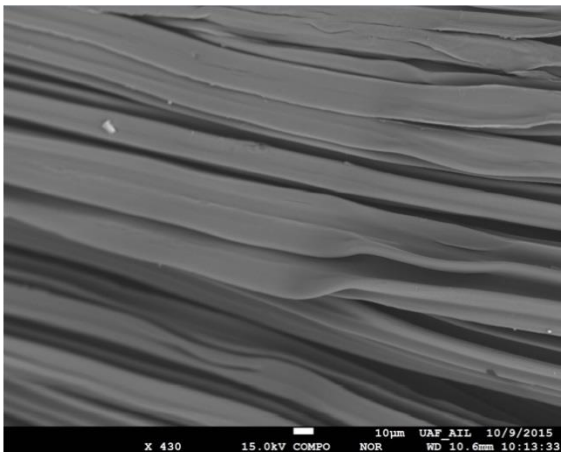

(a) New wicking fabric (Intact Sample 4)

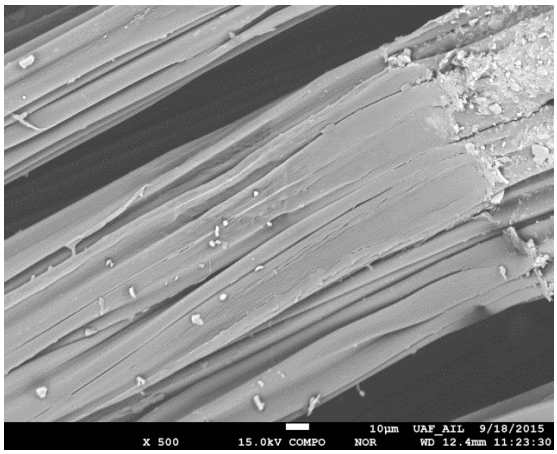

(b) Permanent deformation (Sample 1)

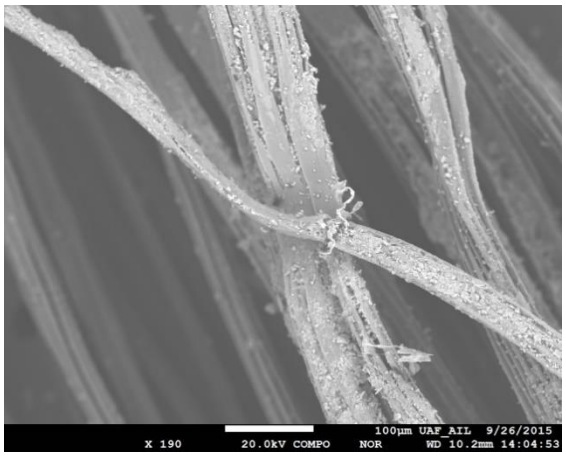

(c) Permanent deformation (Sample 16)

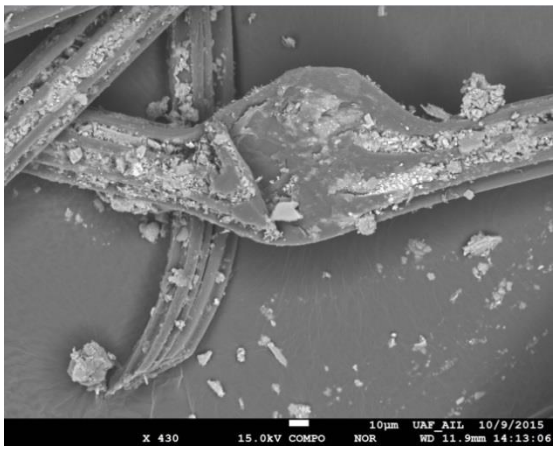

(d) Beaver Slide (Sample 17)

Figure 4.4 SEM images of mechanical failure

Aging

Because the wicking fabric is buried in the soil, another concern involves the wicking fabric's physical and mechanical aging issue, as shown in Figure 4.5. Figure 4.5(a) shows the aging severity of the wicking fabric under the woven polypropylene yarns. Because the fibers on the surface were directly in contact with the soil particles, aging phenomena were usually observed at this location. Figure 4.5(b) shows the fibers at the surface without the woven

polypropylene yarns. As believed, aging was likely due to direct contact with soil particles. The aging effect at the bottom of the deep grooves was more severe than in other areas of the wicking fabric. In comparison, Figure 4.5(c–d) shows the wicking fabric beneath the surface. No obvious aging effect was observed below the surface layer, and the deep grooves were much cleaner than those of fibers at the surface.

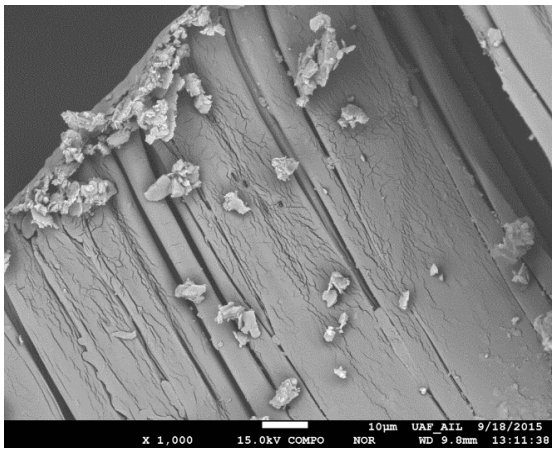

(a) Beaver Slide Sample 3

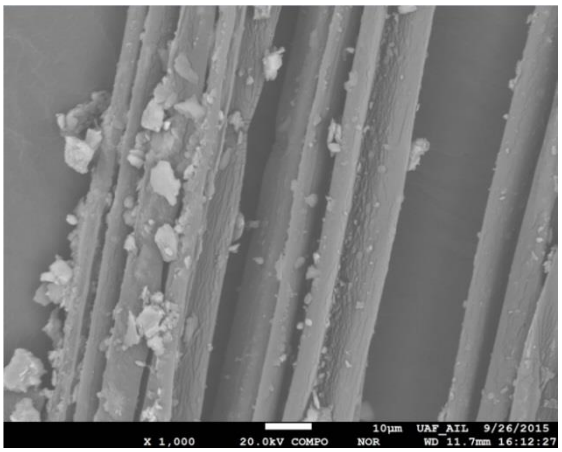

(b) Beaver Slide Sample 11

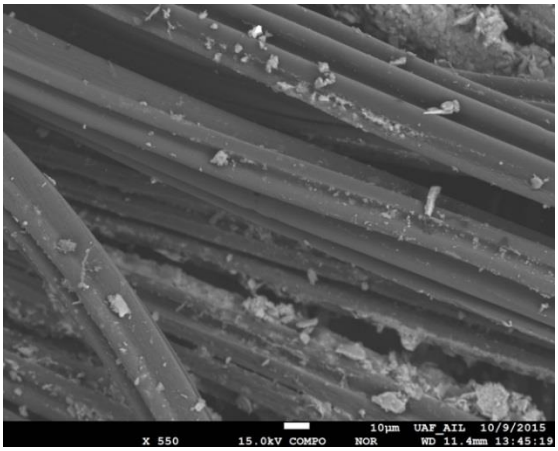

(c) Beaver Slide Sample 21

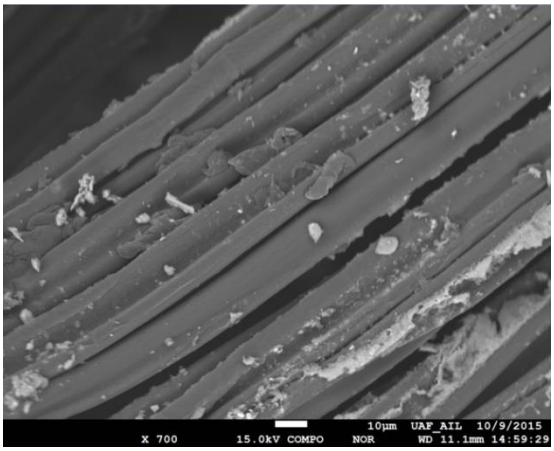

(d) Beaver Slide Sample 26

Figure 4.5 Aging effect

Table 4.1 summarizes the SEM analyses results. In general, the surface of all wicking fabrics was affected by clogging. Permanent deformation and clogging were observed in every

scanned sample. Therefore, these two aspects became major potential issues for consideration in evaluating the H2Ri geotextile's long-term performance. However, only 6.67% of the wicking fabric fibers beneath the surface were affected by clogging, which indicates that even though the surface was contaminated and the drainage paths were blocked, the wicking fibers beneath the surface were well protected and worked effectively as drainage material to transport water laterally under unsaturated conditions. Additionally, permanent deformation was observed in every sample under the polypropylene woven area. Permanent deformations resulted from one or more of the following: (1) high pressure during the manufacturing process, (2) excess compaction energy introduced during the construction and installation process, and (3) high vertical overburden soil pressure and dynamic traffic load during the wicking fabric's service life. Permanent deformation would likely affect the wicking fabric's long-term performance, since drainage paths either are cut off or narrowed, and the deformation would continue to develop over time. Aging effects and mechanical failure were not considered major concerns that would influence the long-term performance of the wicking fabric.

Table 4.1 SEM analyses summary

Sample	**Total**	**Observation**	**Clogging**		**Mechanical Failure**
			Surface	**Beneath**	
Beaver Slide	30	Count	30	2	5
		Percentage (%)	100	6.67	16.67
		Observation	**Permanent Deformation**		**Aging**
		Count	30		7
		Percentage (%)	100		23.33

Lab Samples from Loading Plate Test (Samples Provided by University of Kansas)

Maintaining the high shape factor of a multichannel cross section of the wicking fiber is critical to ensuring the geotextile's best performance. Stresses may cause closure of and cut off the multichannel, which could reduce the geotextile's drainage efficiency. Since SEM analyses of the field samples only indicated cumulative permanent deformation rather than deformation developed during the construction process and under traffic loading separately, the authors wanted to take advantage of samples collected from the lab test performed by the researchers at the University of Kansas. The purpose of the SEM analyses of those samples was to evaluate the geotextile damage that occurred during installation and traffic cyclic loading. The setup of the test section simulated construction and installation in the field. The loading process simulated dynamic traffic loading. By examining the geotextile samples collected from locations with and without loading, it could be determined whether permanent deformation or mechanical failure developed during construction and traffic loading.

The test section consisted of a 0.76 m (30 in.) thick layer of 3% CBR subgrade (75% Kansas River Sand and 25% Kaolinite by weight) and a 0.3 m (12 in.) thick layer of AB-3 aggregate, as shown in Figure 4.6. Three cyclic loading tests were conducted. All three tests were conducted with a 0.3 m (12 in.) diameter steel loading plate that had a rubber bottom layer. The loading plate applied 138 kPa to the base course. For each test, 1000 cycles were carried out. Geotextile was placed at the interface between the two materials. In general, four locations were chosen for sampling, including the center of the loading plate (location 1), edge of the loading plate (location 2), 0.3 m (12 in.) from the center (location 3), and 0.6 m (24 in.) from the center (location 4).

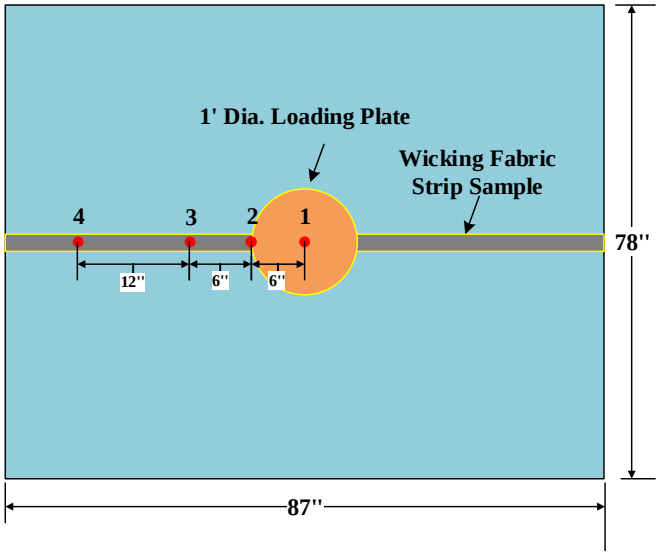

(a) Top view

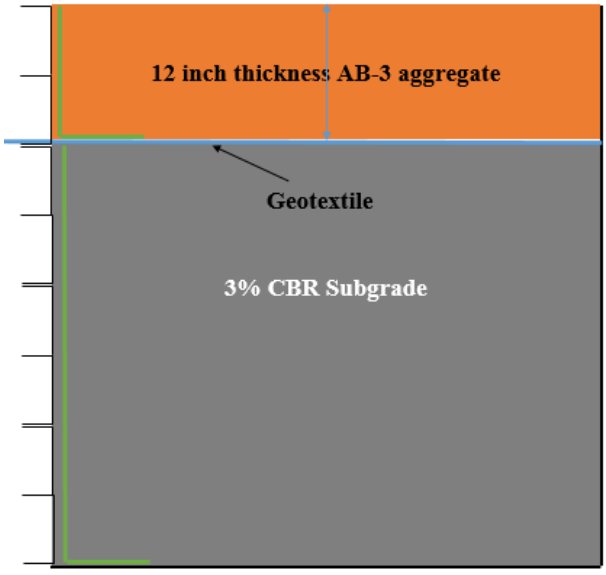

(b) Front view

Figure 4.6 Loading plate test setup

Figure 4.7 shows SEM images of the samples collected from the target locations shown in Figure 4.6. Locations 1 and 2 simulate distress induced during installation and compaction, and locations 3 and 4 represent the potential developed distress under cyclic traffic loading (post-construction). The images to the left are intact geotextile samples; the images to the right are

closer views of the wicking fabric yarns. In general, more soil particles were detained in the deep grooves in locations 1 and 2, where cyclic loading was applied, which indicates that the loading process tends to aggravate the clogging effect. In other words, geotextile beneath wheel paths is expected to have more soil particles detained in the drainage grooves. No significant permanent deformation was observed between locations 1 and 2 and locations 3 and 4, which indicates that the major factor determining permanent deformation is not from the construction (compaction and installation) process or under dynamic traffic load.

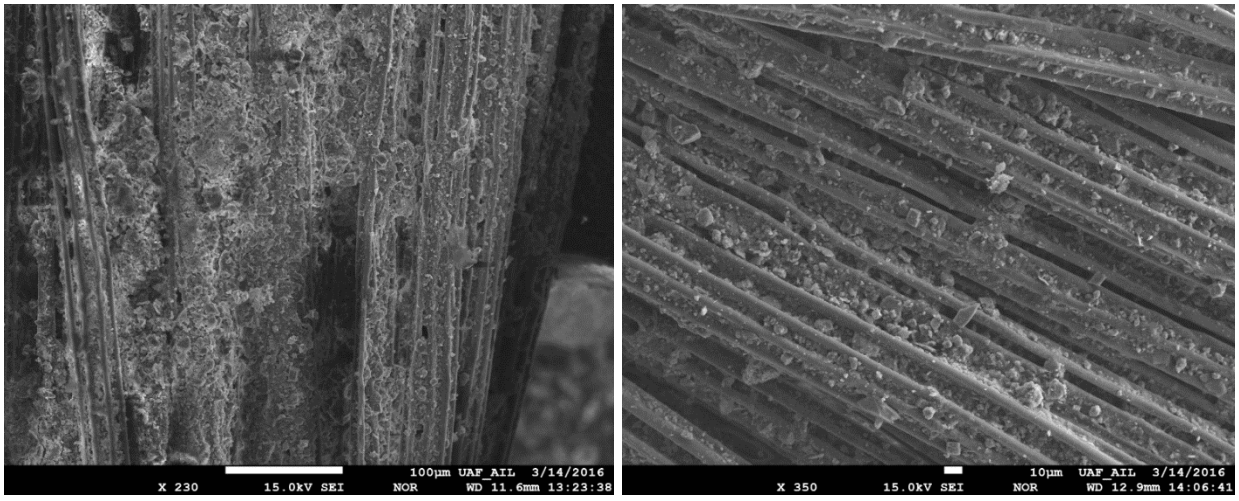

(a) Location1 (intact sample and fabric yarn)

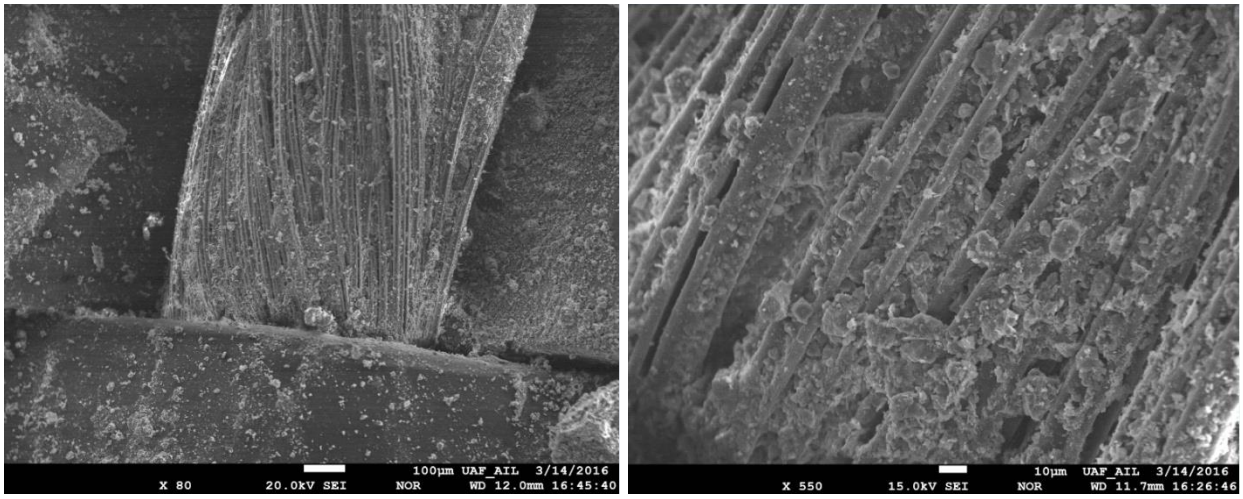

(b) Location 2 (intact sample and fabric yarn)

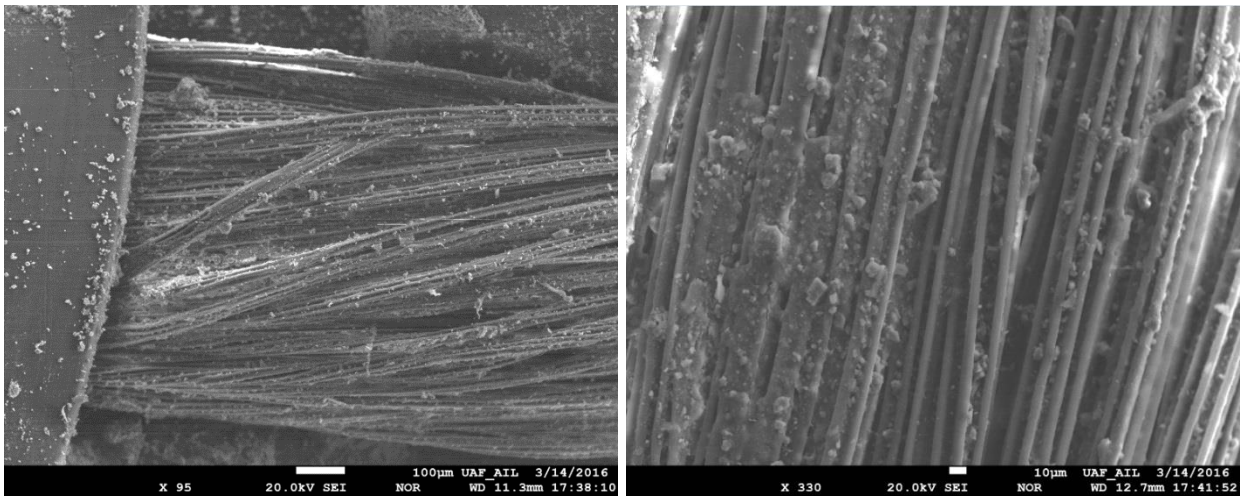

(c) Location 3 (intact sample and fabric yarn)

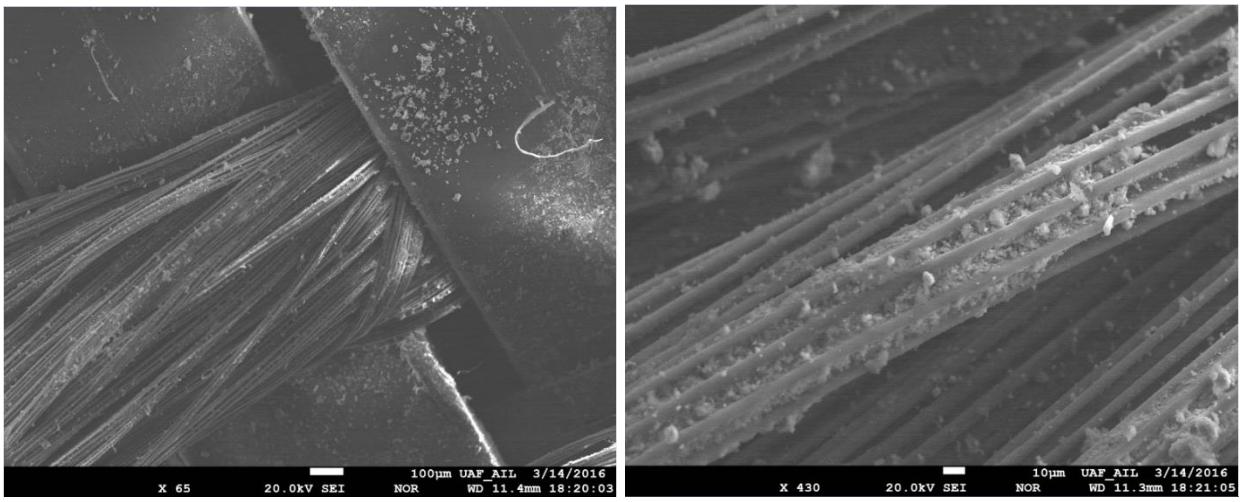

(d) Location 4 (intact sample and fabric yarn)

Figure 4.7 SEM images from locations 1–4

In contrast, Figure 4.8 shows SEM images of brand new geotextile. For the intact sample (left image), permanent deformation already existed under the overlapping area between the polyethene reinforcement yarn and the nylon wicking fabric yarn. A closer view of the overlapping area is shown in the right image. Significant permanent deformation was observed in the overlapping area, where the deep grooves were flattened and could not hold and laterally transport water under unsaturated conditions. Note that SEM images can only be used to

demonstrate the condition of the geotextile surface (where the fibers are directly in contact with the surrounding soils). Field monitoring results indicate that the geotextile still functions 5 years after installation. This fact leads to the authors' argument that deformation occurs at the surface layer and that wicking fibers beneath the surface remain in good shape or are only partially deformed so that the geotextile still functions.

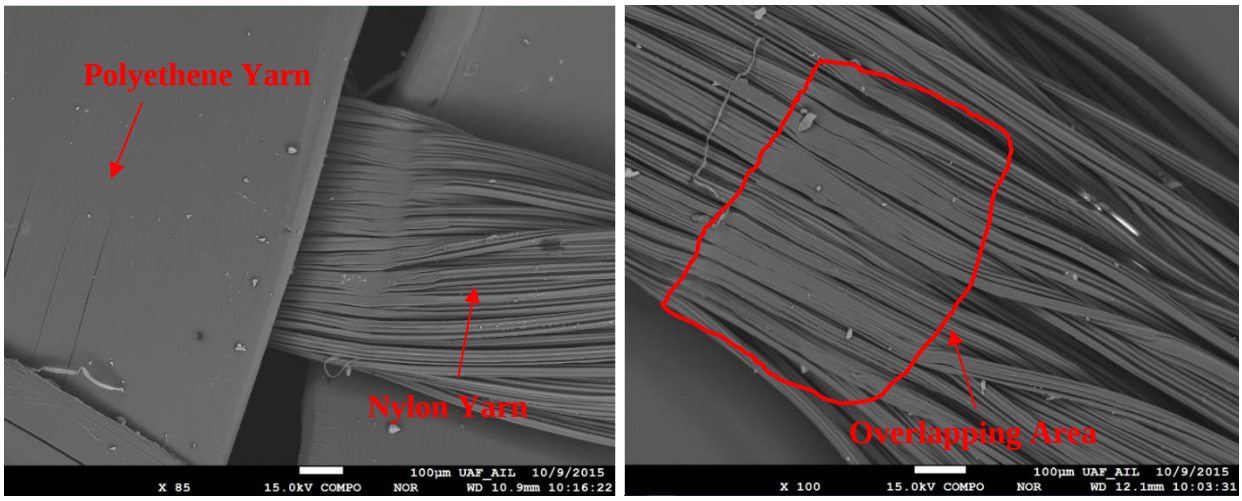

Figure 4.8 SEM images of new H2Ri geotextile

In order to solve this puzzle, the authors washed the geotextile with tap water and air-dried it. Then only one wicking fabric yarn in the overlapping area was scanned, this time to examine the severity of permanent deformation with depth. Figure 4.9 shows the SEM images of the wicking fabric after washing. Compared with the contaminated samples in Figure 4.8, the wicking fabric after washing was partially clean, but some soil particles were still detained in the deep grooves. Figure 4.9(b) shows that permanent deformation did not develop further compared with the new geotextile in Figure 4.8. Figure 4.9(c) demonstrates that the deformation severity of the wicking fabric varied with depth. The permanent deformation decreases with depth, and this phenomena in accordance with the field observation further validates the authors' assertion that the wicking fabric beneath the surface experiences less deformation due to the protection of the

surface layer and can still function effectively to drain water out of the soil. Figure 4.9(d) shows the clogging effect of the wicking fabric beneath the surface. The deep grooves were partially occupied by soil particles, also indicating that clogging does not affect the wicking fabric beneath the surface.

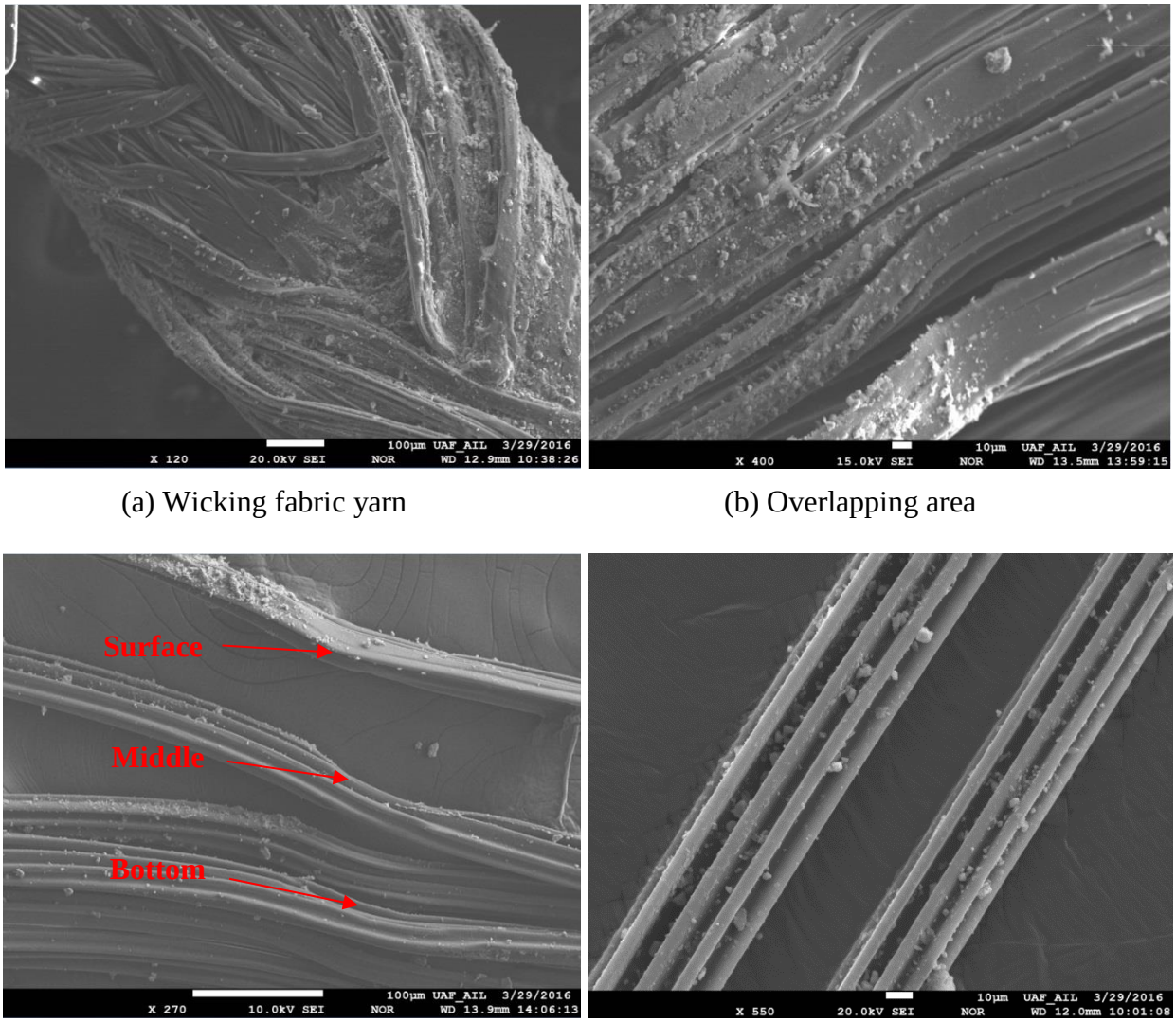

(a) Wicking fabric yarn (b) Overlapping area

(c) Deformation with depth (d) Clogging effect

Figure 4.9 SEM images of geotextile after washing

Salt Concentration Issue

The H2Ri geotextile is environmentally friendly, and its application in roadway drainage systems is growing. Sometimes H2Ri is used in arid climates where intense evaporation draws saline water to the soil surface from the water table by capillary action. Subsequent evaporation increases salt concentration and precipitation, leaving salt in the soil. Due to the cyclic evaporation-precipitation process, soluble and insoluble salt may also concentrate within the deep grooves of the wicking fiber. This salt concentration-induced clogging may impede the drainage efficiency of the geotextile. One of the purposes of this study was to evaluate clogging induced by salt concentration, both soluble (NaCl) and insoluble (CaCO3) salt, at different concentration levels.

The salt concentration of water extracted from saturated soil (called saturation extract) defines the salinity of this soil. According to the FAO (Food and Agriculture) corporate document repository, if this water contains less than 3 g/L, the soil is said to be non-saline (see Table 4.2). If the salt concentration of the saturation extract contains more than 12 g/L, the soil is said to be highly saline.

Table 4.2 Soil salinity

Salt Concentration (in g/L)	**Salinity**
0-3	Non Saline
3-6	Slightly Saline
6-12	Medium Saline
More than 12	Highly Saline

The authors decided to use two types of salt to perform the salt concentration test, including NaCl (soluble salt) and $CaCO_3$ (insoluble salt). The designed salt concentrations listed in Table 4.3 are based on the soil salinity information provided in Table 4.2.

Table 4.3 Designed salt concentrations

Salt Type	Salt Concentration (in g/L)
NaCl and $CaCO_3$	1.5
	4.5
	9
	15

For preparing the soluble salt, the target amount of salt was dissolved in distilled water. Then the geotextile was cut into small pieces and immersed in the salt solute for at least 24 hours. For the insoluble salt two types of chemical reagents were used according to Equation 4.1:

$$Ca(OH)_2 + Na_2CO_3 \rightarrow CaCO_3 \downarrow + 2NaOH \quad (4.1)$$

The solubility for $Ca(OH)_2$ and Na_2CO_3 is 1.73 g/L (20°C) and 164 g/L (15°C), respectively. Since the solubility of $Ca(OH)_2$ is too small, the solute needs to be filtered before using, as shown in Figure 4.10. The $Ca(OH)_2$ solute was filtered with two layers of filter paper. A comparison indicates that the $Ca(OH)_2$ solute was clear after the filtration process.

After the geotextile was soaked in Na_2CO_3 solute for over 24 hours, the geotextile was immersed in $Ca(OH)_2$ solute using tweezers. After another 24 hours, the geotextile was checked for reaction, as shown in Figure 4.11. To ensure that there was enough $Ca(OH)_2$ reagent for reaction, 500 ml of $Ca(OH)_2$ was used. The $Ca(OH)_2$ solute with geotextile after reaction is shown in Figure 4.11. The geotextile samples were removed from the solute and air-dried on the table at room temperature, as shown in Figure 4.12.

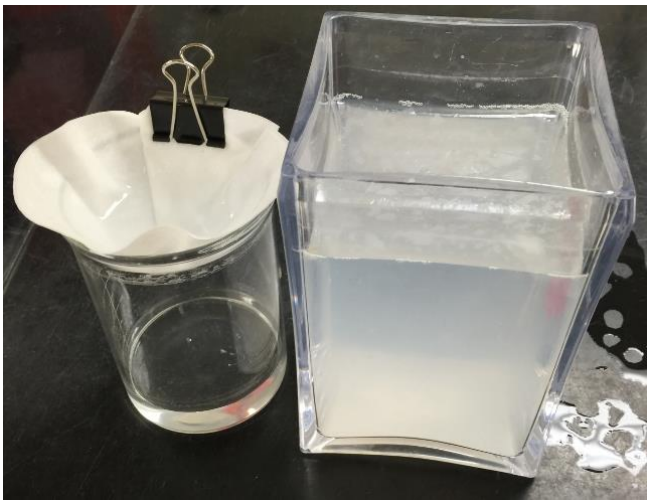

Figure 4.10 $Ca(OH)_2$ solute filtration

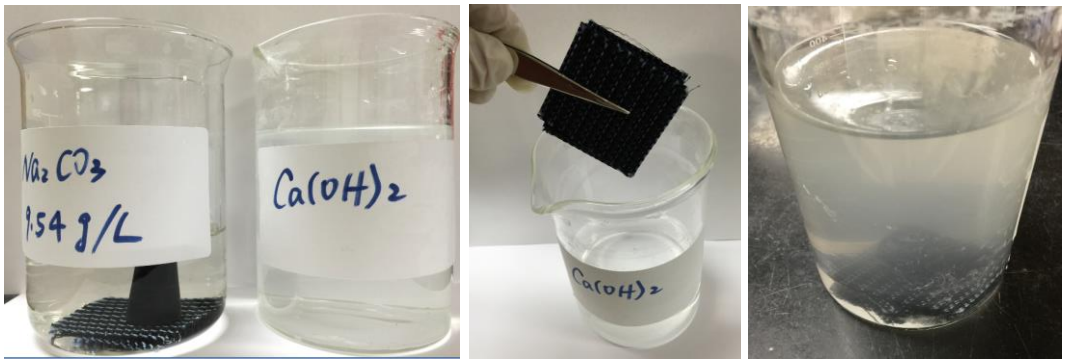

Figure 4.11 Reaction process

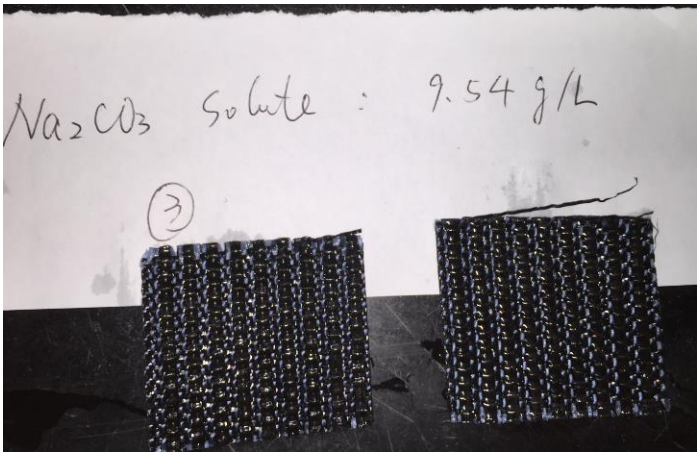

Figure 4.12 Geotextile sample air drying process

To simulate salt concentration during the drying and wetting processes, another set of samples was prepared using the same method discussed above. This set of samples, however, was washed with distilled water and then air-dried (representing the wetting process) again before the SEM analyses.

Salt Concentration for Soluble and Insoluble Salt (Drying Process)

Figure 4.13 shows the comparison of different salt concentrations for samples with both soluble and insoluble salt. For samples with soluble salt, the clogging effect was severe with increments of salt concentration level (Figure 4.13a and c). For salt concentration of 1.5 g/L and 4.5 g/L, clogging was not a major issue during the drying process, while for samples with salt concentration of 9 g/L and 15 g/L, parts of the deep grooves were blocked with salt crystals. Moreover, concentration was worse at the overlapping area (Figure 4.13c). For comparison, no clogging was observed for samples with insoluble salt (Figure 4.13b and d), perhaps because the $CaCO_3$ particles during the reaction immediately precipitated and did not form large clusters that blocked the deep grooves. Therefore, even though the concentration level increased, no clogging was observed throughout the SEM analyses.

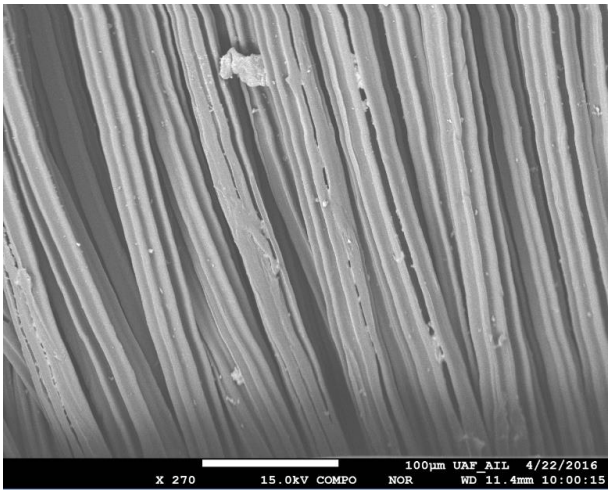

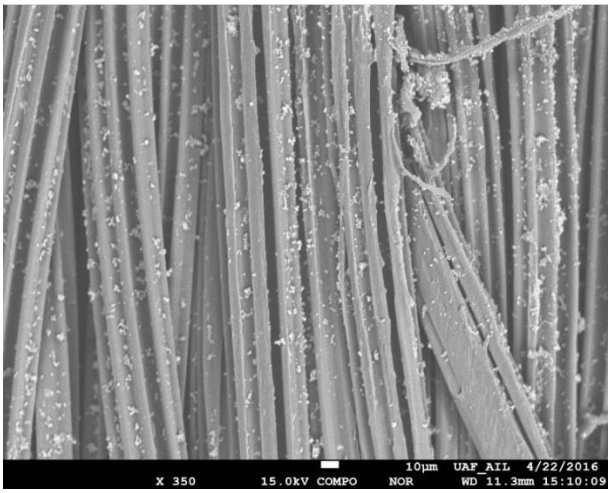

(a) 1.5 g/L (NaCl)

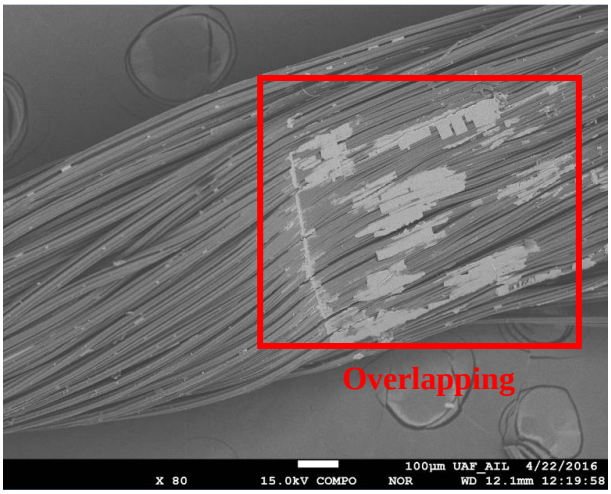

(b) 1.5 g/L ($CaCO_3$)

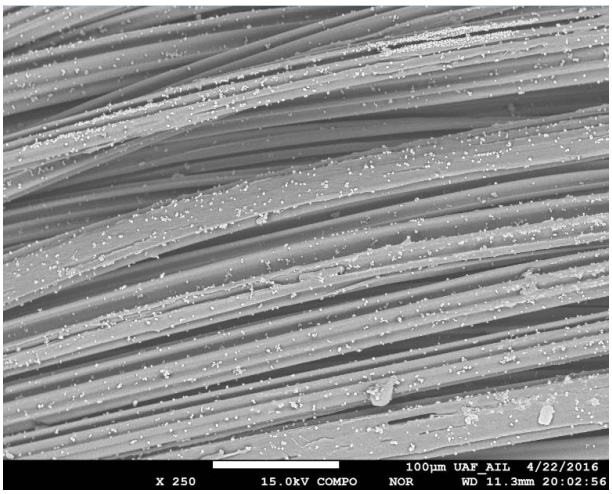

(c) 15 g/L (NaCl)

(d) 15 g/L ($CaCO_3$)

Figure 4.13 Salt concentration for soluble and insoluble salt (drying process)

Salt Concentration for Soluble and Insoluble Salt (Wetting Process)

Figure 4.14 shows SEM images of salt concentration for samples washed with distilled water. During the wetting process, most of the soluble salt could be dissolved in water and washed away. Therefore, clogging was not a major concern during the wetting process for samples with soluble salt (Figure 4.14a), while the $CaCO_3$ particles detained on the wicking fiber could not be washed away since they could not dissolve in water. Similar to Figure 4.13(d), no clogging was observed for samples with insoluble salt.

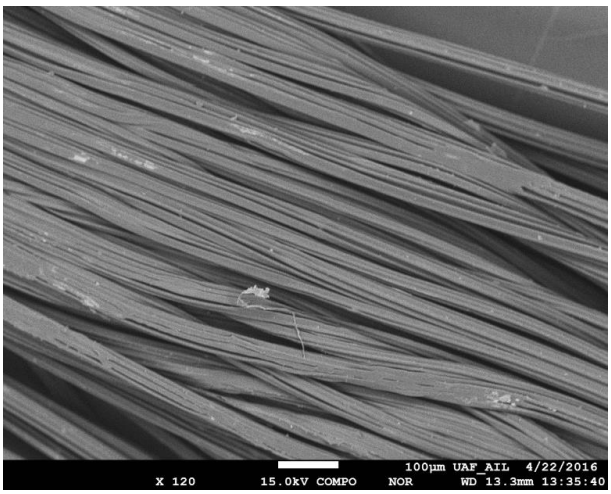

(a) 15 g/L (NaCl)

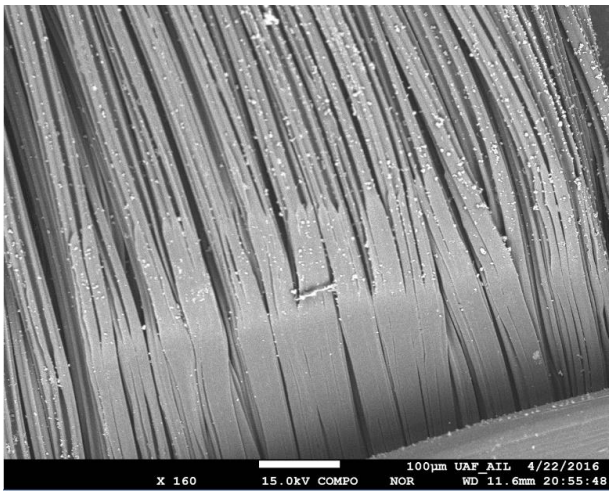

(b) 15 g/L ($CaCO_3$)

Figure 4.14 Salt concentration for soluble and insoluble salt (wetting process)

Salt Concentration Location

It was equally important to observe salt concentration locations. If salt concentrates at the reinforcement yarn, it does not reduce the geotextile's drainage efficiency; however, if salt concentrates in the deep grooves, clogging becomes a major issue. Figure 4.15 demonstrates the full-scale spectrum analysis result. Thirty frames were scanned across the entire scanning area. The full-scale spectrum showed the statistical scanning results based on the cumulative frequency observed for each chemical element in the periodic table.

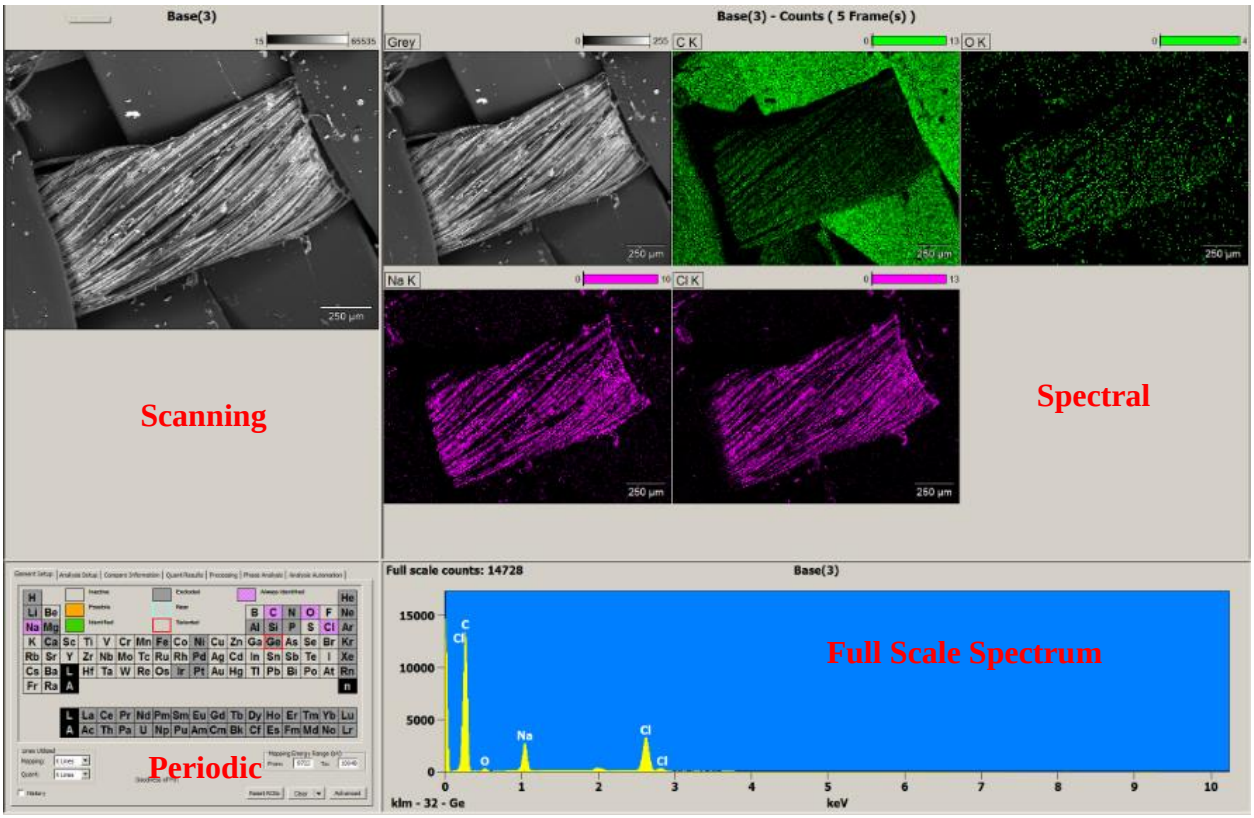

Figure 4.15 Full-scale spectrum analysis

Figure 4.16 shows the full-scale spectrum analysis results. For samples with soluble salt at lower concentration level (1.5 g/L and 4.5 g/L) (Figure 4.16a), no obvious concentration areas were observed during the drying process. However, for samples with soluble salt at higher concentration level (9 g/L and 15 g/L), concentration areas were observed in the deep grooves of the wicking fiber (Figure 4.16b). This indicates that soluble salt causes partial clogging during the drying process and that geotextile drainage efficiency partially decreases. For comparison, no salt concentration was observed after the samples were washed with distilled water, regardless of the salt concentration level (Figure 4.16c and d). Moreover, since the insoluble salt could not form particles large enough to block the deep grooves, no concentration area was observed during both drying and wetting processes (Figure 4.16e and f).

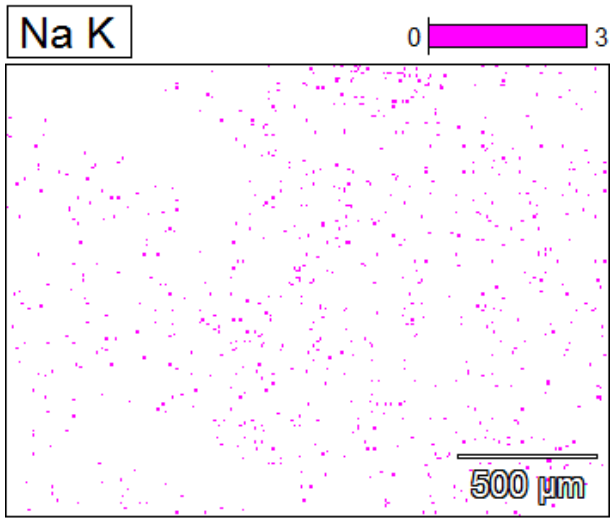

(a) 1.5 g/L (drying process)

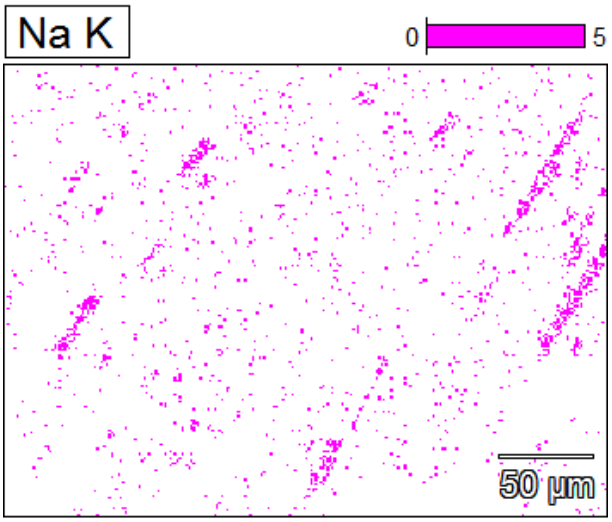

(b) 9 g/L (drying process)

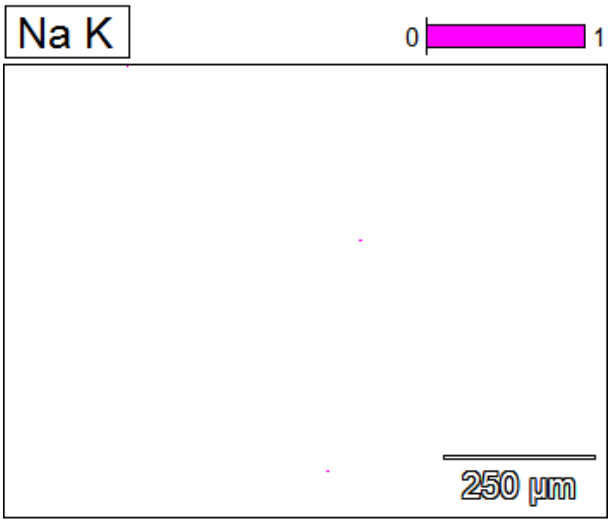

(c) 1.5 g/L (wetting process)

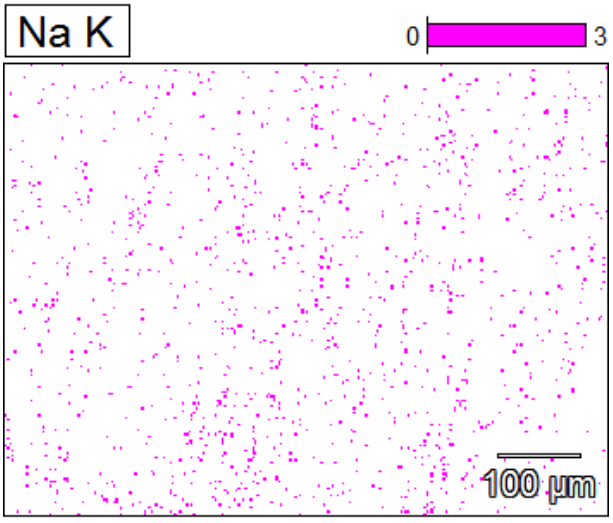

(d) 9 g/L (wetting process)

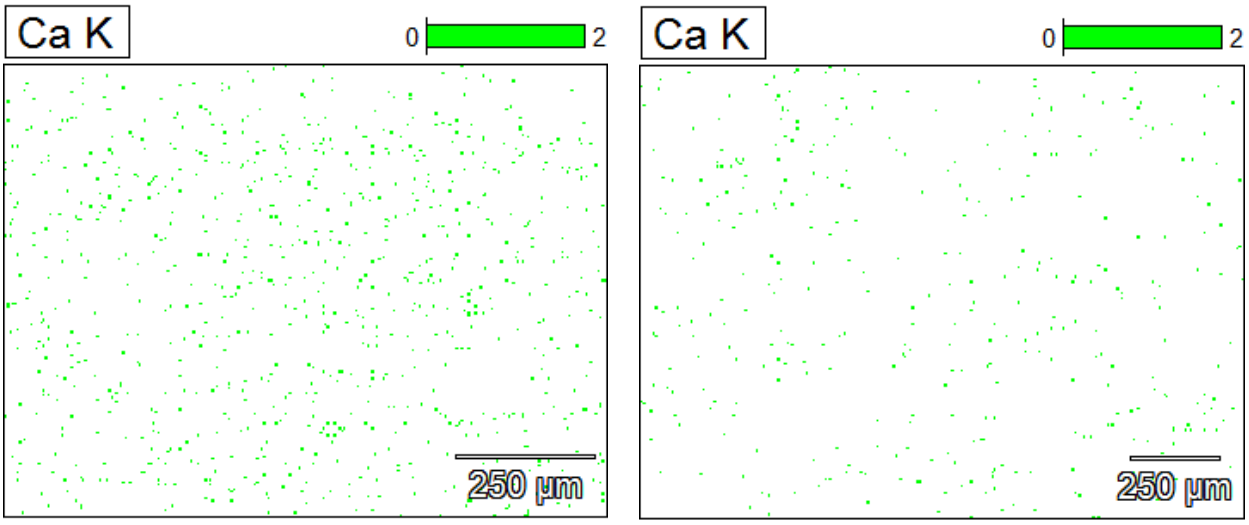

(e) 15 g/L (wetting process) (d) 15 g/L (drying process)

Figure 4.16 Soluble salt concentrations

In sum, salt concentration-induced clogging was observed in samples with soluble salt during the drying process, and clogging severity increased with higher concentration level. However, clogging was not a major issue during the wetting process. Concentration areas were found within the deep grooves and beneath the overlapping area. In samples with insoluble salt, no clogging was observed in both the drying and wetting processes. Therefore, salt concentration is not a major factor that influences geotextile drainage efficiency. Even though the geotextile was installed in soils with high salinity, only the soluble salt in the soil partially influenced its efficiency. The H2Ri wicking fabric is, in general, a promising material for use in laterally draining water under unsaturated conditions.

CHAPTER 5.0 CONCLUSIONS AND RECOMMENDATIONS

Excessive water in pavement structure can cause a variety of engineering problems, such as soil expansion and collapse, soil strength and stiffness reduction, excess pore water pressure, stripping in asphalt pavement, and cracks. Existing pavement or roadway drainage design methods only deal with "free water" or gravitational water flow, and water detained by capillary force (in unsaturated conditions) cannot be drained. A new type of geotextile with lateral wicking ability has been introduced, which when incorporated with higher specific surface area, continuously drains water out of pavement structure even under unsaturated conditions. A series of lab tests were conducted to characterize the mechanical and hydraulic properties of the soil and the geotextile.

The following conclusions and recommendations are based on the lab tests:

1. The soil-geotextile system works effectively to drain capillary water out of embankments under unsaturated conditions. The geotextile can serve as a "connection" that continuously wicks water out of an embankment by taking advantage of the suction gradient within and out of the pavement structure.

2. By implementing the geotextile and maintaining post-compaction water content at its optimum value, the resilient modulus can theoretically be increased by 3 times, and permanent deformation can be decreased to half. Structural benefits can be further enlarged 4–6 times if the water content is reduced by 2%. Although the conclusions are based on a typical type of soil, this report provides the methods and procedures to evaluate and quantify pavement performance improvement. If other types of soil are used, follow the steps described in Chapter 3.0.

3. Theoretically, the soil-geotextile system can effectively wick water out of an embankment within 200 kPa. There are two types of drainage path: inter-yarn drainage (air entry value is about 6.7 kPa) and inner-yarn drainage (air entry value is about 200 kPa).The inner-yarn air entry value plays a critical role in controlling the geotextile hydraulic characteristics under unsaturated conditions. The proposed air entry value-determination method needs further study to be validated.

4. Soil unsaturated hydraulic conductivity is relatively small when the suction value is greater than 70 kPa. This indicates that even though gravel is conventionally considered a good capillary barrier, it cannot effectively drain free water under unsaturated conditions (when the volume of air is large in the soil micropores). Within the soil-geotextile functional range, the unsaturated hydraulic conductivity of geotextile is always higher than that of the surrounding soil, indicating that the geotextile has the ability to continuously wick water out of the pavement structure.

5. The shear strength at the soil-geotextile interface is not sensitive to water content variation. Negative pore water pressure serves as additional confinement when the soil is in unsaturated condition. The maximum frictional angle at the soil-geotextile interface is with a corresponding water content of 2%.

Microscopic-level SEM analyses helped address the concerns and potential issues raised by the engineers and sponsors and led to three additional conclusions, summarized as follows:

6. Clogging, aging, and puncturation are not major concerns that affect the drainage efficiency of the geotextile. Clogging was detected in all the samples. However, clogging only occurs at the geotextile's surface, since this part of the geotextile is in direct contact with the

surrounding soils. The wicking fabric beneath the surface remains relatively clean and is not influenced by clogging. Moreover, since few samples show aging and puncturation (only 16.7%) 5 years after installation, these two issues should not be major concerns at this moment.

7. Salt concentration-induced clogging is not a major concern influencing geotextile drainage efficiency. Salt concentration-induced clogging was observed in samples with soluble salt during the drying process, and clogging severity increased with higher salt concentration level. However, clogging was not a major issue during the wetting process. Concentration areas were found within the deep grooves and beneath the overlapping area. Moreover, for samples with insoluble salt, no clogging was observed in the drying and wetting processes. Even though the geotextile was installed in soils with high salinity, only the soluble salt in the soil partially influenced its efficiency. The H2Ri wicking fabric is in general a promising drainage material for laterally draining water under unsaturated conditions.

8. Permanent deformation is a major concern influencing geotextile drainage efficiency. Permanent deformation mainly occurs during manufacturing (maybe the tensile force is too great during the weaving process). If the fabricating process can be improved, the geotextile drainage efficiency can be collaterally enhanced. Note that only the geotextile surface was affected by severe deformation. The wicking fabric beneath was either partially deformed or without deformation. Both lab loading plate and field monitoring results indicate that the geotextile still works effectively to wick water out of the pavement structure. Moreover, during normal construction and dynamic traffic load, the propagation of deformation is limited. Test results indicate that more soil particles are detained in the deep grooves of the geotextile under dynamic traffic load. Again, this increased risk of clogging only occurs at the surface of the geotextile and does not influence the wicking fabric beneath.

REFERENCES

AASHTO (1993). "AASHTO Guide for Design of Pavement Structures." *American Association of State Highway and Transportation Officials* (AASHTO), Washington, DC, USA.

AASHTO T307-99 (1999). "Standard Method of Test for Determining the Resilient Modulus of Soils and Aggregate Materials." *American Association of State and Highway Transportation Officials*, Washington, DC, USA.

Alim, M. A., and Nishigaki, M. (2009). "Shear Strength Behavior of Unsaturated Compacted Sandy Soils." *International Symposium on Prediction and Simulation Methods for Geohazard Mitigation*, Kyoto, Japan, May, 25–37, 307–312.

Aravin, V. I., and Numerov, S. N. (1953). "Theory of Fluid and Gases through the Underformable Porous Medium." *Publishing House of Technical and Theoretical Publications*, Moscow.

Arya, L. M., and Paris, J. F. (1981). "A physico-empirical model to predict the soil moisture characteristic from particle-size distribution and bulk density data." *Soil Science Society of America Journal*, 45, 1023–1030.

Arya, L. M., Leij, F. J., and Genuchten, V. A. (1999). "Scaling parameter to predict the soil water characteristic from particle size distribution data." *Soil Science Society of America Journal*, 63, 510–519.

ASTM C127 (2015). "Standard Test Method for Determining the Shear Strength of Soil-Geosynthetic and Geosynthetic-Geosynthetic Interfaces by Direct Shear." West Conshohocken, PA.

ASTM C1559-04. (2004). "Standard Test Method for Determining Wicking of Glass Fiber." West Conshohocken, PA.

ASTM D4491-99a. (2009). “Standard Test Methods for Water Permeability of Geotextiles by Permittivity.” West Conshohocken, PA.

ASTM D4595-11 (2011). “Standard Test Method for Tensile Properties of Geotextiles by the Wide-Width Strip Method.” West Conshohocken, PA.

ASTM D4751-12 (2012). “Standard Test Method for Determining Apparent Opening Size of a Geotextile.” West Conshohocken, PA.

ASTM D5321/D5321 M-14 (2014). “Standard Test Method for Determining the Shear Strength of Soil-Geosynthetic and Geosynthetic-Geosynthetic Interfaces by Direct Shear.” West Conshohocken, PA.

ASTM D6767-11. (2011). “Standard Test Method for Pore Size Characteristics of Geotextiles by Capillary Flow Test.” West Conshohocken, PA.

Barber, E. S., and Sawyer, C. L. (1952). "Highway Subdrainage." *Proceedings, Highway Research Board,* 643–666.

Barksdale, R. D. (1972). ‘‘Laboratory Evaluation of Rutting in Base Course Materials.’’ *Proceedings, 3rd International Conference on Structure Design of Asphalt Pavements,* 161–174.

Barksdale, R. D., and Itani, S. Y. (1989). “Influence of aggregate shape on base behavior.” *Transportation Research Record* 1227, National Research Council, Washington, DC, 15–31.

Bouazza, A. (2002). “Geosynthetic clay liners.” *Geotextiles and Geomembranes*, 20(1), 3–17.

Bouazza, A., Gates, W. P., and Abuel, N. H. (2006). "Factors Impacting Liquid and Gas Flow through Geosynthetic Clay Liners." *Geosynthetics-Recent Developments. Commemorating Two Decades of Geosynthetics in India*, 119–146.

Casagrande, A. (1931). "Discussion of Frost Heaving," *Proceedings, Highway Research Board*, Vol. 11, 163–172.

Casagrande, A. (1947). "Classification and Identification of Soils." *Proceedings, American Society of Civil Engineers*, Vol. 73(6), 283.

Cedergren, R. H. (1974). *Drainage of Highway and Airfield Pavements*. John Wiley & Sons, Inc., NY.

Cedergren, H. R., O'Brien, K. H., and Arman, J. A. (1973). "Guidelines for the Design of Subsurface Drainage Systems for Highway Structural Sections." Final Report Number FHWA-RD-73-14, *Federal Highway Administration*, Washington, DC.

Chamberlain, E. J. (1987). "A Freeze-Thaw Test to Determine the Frost Susceptibility of Soils." U.S. Army Corps of Engineers, *Cold Regions Research and Engineering Laboratory (CRREL)*, Special Report: 87-1.

Csathy, T. I., and Townsend, D. L. (1962). "Pore size and field frost performance of soils." *Highway Research Board Bulletin*, No.331, 67–80.

FHWA (1980). "Highway Subdrainage Design." Federal Highway Administration (FHWA), FHWA-TS-80-224, U.S. Department of Transportation.

Fredlund, D. G., and Xing, A. (1994). "Equations for the soil-water characteristic curve." *Canadian Geotechnical Journal*, 31(4), 521–532.

Fredlund, D. G., and Rahardjo, H. (1993). *Soil Mechanics for Unsaturated Soils.* John Wiley & Sons, Inc., New York.

Fredlund, D. G., Vanapalli, S. K., Xing, A., and Pufahl, D. E. (1995). "Predicting the Shear Strength Function for Unsaturated Soils Using the Soil-Water Characteristic Curve." *Proceedings, 1st International Conference on Unsaturated Soils*, September 6–8 Paris, France, Vol. 1, 63–70.

Fredlund, M. D., Wilson, G. W., and Fredlund, D. G. (2002). "Use of the grain-size distribution for estimation of the soil-water characteristic curve." *Canadian Geotechnical Journal*, 39, 1103–1117.

Genuchten, V. A. (1980). "Closed-form equation for predicting the hydraulic conductivity of unsaturated soils." *Soil Science Society of America Journal*, 44(5), 892–898.

Goldberg, R. N., and Nuttall, R. L. (1978). "Evaluated activity and osmotic coefficients for aqueous solutions: The alkaline earth metal halides." *Journal of Physical and Chemical Reference Data*, 7(1), 263–310.

Gupta, S. C., and Ewing, R. P. (1992). "Modeling Water Retention Characteristics and Surface Roughness of Tilled Soils." *Proc. Int. Workshop on Indirect Methods for Estimating the Hydraulic Properties of Unsaturated Soils*. University of California, Riverside, CA, 279–288.

Haynes, H. J., and Yoder, J. E. (1963). "Effects of Repeated Loading on Gravel and Crushed Stone Base Course Materials Used in the AASHO Road Test." Publication FHWA/IN/JHRP-63/04. Joint *Highway Research Project*, Indiana Department of Transportation and Purdue University, West Lafayette, Indiana, 1963. doi: 10.5703/1288284313622.

Hicks, R.G., and Monismith, C.L. (1971). “Factors influencing the resilient properties of granular materials.” *Transportation Research Record* 345, National Research Council, Washington, DC, 15–31.

Holtz, R. D., Christopher, B. R., and Berg, R. R. (1998). “Geosynthetic Design and Construction Guideline.” *National Highway Institute, Federal Highway Administration*, Washington, DC, Report No. FHWA HI-95-038, 460.

Khoury, N. N., and Zaman, M. M. (2004). “Correlation between resilient modulus, moisture variation, and soil suction for subgrade soils.” *Transportation Research Record* 1874 Transportation Research Board 1874, 99–107.

Knight, M.A., and Kotha, S.M. (2001). “Measurement of geotextile-water characteristic curves using a controlled outflow capillary pressure cell.” *Geosynthetics International*, 8(3), 271–282.

Koerner, G. R. (2005). “Update on GSI’s Geotextile Highway Separation Study.” *Proceedings of the GRI-18 Conference on Geosynthetics Research & Development In-Progress*, GeoFrontiers, January 26, 2005, GII Publication, Folsom, PA.

Kunze, R. J., Uehara, G., and Graham, K. (1968). “Factors important in the calculation of hydraulic conductivity.” *Soil Science Society of America Proceedings*, 32, 760–765.

Li, L., Liu, J., Zhang, X., and Saboundjian, S. (2011). “Resilient modulus characterization of Alaska granular base materials.” *Transportation Research Record* 2232, Transportation Research Board, 44–54.

Liang, R., Rabab’ah, S., and Khasawneh, M. (2008). “Predicting moisture-dependent resilient modulus of cohesive soils using soil suction concept.” *Journal of Transportation Engineering*, 134(1), 34–40.

Lin, C., Presler, W., Zhang, X., Jones, D., and Odgers, B. (2015a). "Long-term performance of wicking fabric in Alaska pavements." *Journal of Performance of Construction Facilities, ASCE*., DOI: 10.1061/(ASCE)CF.1943-5509.0000936.

Lin, C., Zhang, X., and Presler, W. (2015b). "Application of Wicking Fabric to Reduce Damage in Alaskan Pavements." Final Project Report to TenCate Geosynthetics (North America), Alaska University of Transportation Center, University of Alaska Fairbanks, under review.

Maree, J. H., Freeme, C. R., Van Zyl, N. J., and Savage, P. F. (1982). "The Permanent Deformation of Pavements with Untreated Crushed Stone Bases as Measured in Heavy Vehicle Simulator Tests." *Proceedings, 11th ARRB Conference*, Part 2, 16–25.

McKee, C. R., and Bumb, A. C. (1984). "The Importance of Unsaturated Flow Parameters in Designing a Monitoring System for a Hazardous Wastes and Environmental Emergencies." *Hazardous Materials Control Research Institute National Conference*, Houston, TX, March, 50–58.

MEPDG (2004). "National Cooperative Highway Research program, Transportation Research Board and National Research Council. Mechanistic-Empirical Design of New and Rehabilitated Pavement Structures." *National Cooperative Highway Research Program*, NCHRP Project 1-37A Report, National Research Council. Washington, DC.

Muskat, M. (1946). *The Flow of Homogeneous Fluids through Porous Media. J. W. Edwards, Inc.*, Ann Arbor, MI.

Nazzal, M. D., and Mohammad, L. N. (2010). "Estimation of resilient modulus of subgrade soils for design of pavement structures." *Journal of Materials in Civil Engineering*, 22(7), 726–34.

Nguyen, Q., Fredlund, D. G., Samarasekera, L., and Marjerison, B. L. (2010). "Seasonal pattern of matric suctions in highway subgrades." *Canadian Geotechnical Journal*, 47(3), 267–280.

Rada, G., and Witczak, M. W. (1981). "Comprehensive evaluation of laboratory resilient moduli results for granular material." *Transportation Research Record 810*, Transportation Research Board, 23–33.

Shukla, S. K., and Yin, J. H. (2006). *Fundamentals of Geosynthetic Engineering.* Taylor & Francis Group, London, UK, 410.

Stormont, J.C., Henry, K., and Evans, T. (1997). "Water retention functions of four nonwoven polypropylene geotextiles." *Geosynthetics International*, 4(5), 273–300.

Taber, S. (1929). "Frost heaving." *Journal of Geology*, 38, 303–317. *In:* Historical Perspectives in Frost Heave Research. CRREL Special Report 91-23, U.S. Army Cold Regions Research and Engineering Laboratory, Hanover, NH, 29–35.

Taber, S. (1930a). "The mechanics of frost heaving." *Journal of Geology*, 38, 303–317.

Taber, S. (1930b). "Freezing and thawing of soils as factors in the destruction of road pavements." *Public Roads*, 11(6), 113–132.

Taylor, M. A., and Khosla, N. P. (1983). "Stripping of asphalt pavement: State of the art." *Transportation Research Record 911*. Transportation Research Board, National Research Council Washington, DC, 150–158.

Thom, N. H., and Brown, S. F. (1987). "Effect of moisture on the structural performance of a crushed-limestone road base." *Transportation Research Record 1121*, Transportation Research Board, Washington, DC, 50–56.

Wang, F., Han, J., Zhang, X., and Guo, J. (2015). "Laboratory test to evaluate effectiveness of wicking fabric in soil moisture reduction." *Journal of Geotechnical and Geoenvironmental Engineering*, ASCE, under review.

Yang, S. R., Lin, H. D., Kung, J. H. S., and Huang, W. H. (2008). "Suction controlled laboratory test on resilient modulus of unsaturated compacted subgrade soils," *Journal of Geotechnical and Geo-environmental Engineering*, 134(9), 1375–1384.

Yang, S.R., Huang, W.H., and Tai, Yu-Tsung (2005). "Variation of resilient modulus with soil suction for compacted subgrade soils." *Transportation Research Record 1913*, Transportation Research Board, 99–106.

Zhang, X., and Belmont, N. (2009). "Use of Mirafi Nylon Wicking Fabric to Help Prevent Frost Heaving in Alaska Pavement: 1st, 2nd, 3rd, 4th, and 5th progress reports." Progress reports to TenCate Geosynthetics (North America).

Zhang, X., and Presler, W. (2012). "Use of H2Ri Wicking Fabric to Prevent Frost Boils in the Dalton Highway Beaver Slide Area, Alaska." Alaska University Transportation Center (AUTC) Project Report, No. RR10.02 & 510020, August.

Zhang, X., and Presler, W. (2012). "Use of H2Ri Wicking Fabric to Prevent Frost Boils in the Dalton Highway Beaver Slide Area, Alaska." Alaska University Transportation Center, University of Alaska Fairbanks, INE/AUTC 12.23.

Zhang, X., Presler, W., Li, L., Jones, D., and Odgers, B. (2014). "Use of wicking fabric to help prevent frost boils in Alaskan pavements." *Journal of Materials in Civil Engineering*, ASCE, 728–740.

Zornberg, J. G., Bouazza, A., and McCartney, J. S. (2010). "Geosynthetic capillary barriers: Current state of knowledge." *Geosynthetics International*, 17(5), 273–300.

Zornberg, J. G., Odgers, B., Roodi, G. H., and Azevedo, M. M. (2013). "Advantages and Applications of Enhanced Lateral Drainage in Pavement Systems." *Proceedings of the 2nd African Regional Conference on Geosynthetics*, GeoAfrica 2013, 18–20 November, Accra, Ghana, 539–548.

Zornberg, J.G., and Thompson, N. (2010). "Guide for the Application and Selection of Geotextiles." Center for Transportation Research (CTR), Document 0-5812-P1, Austin, TX, November, 16.

APPENDIX A BASIC PROPERTIES FOR AB3 BASE COURSE

Table A1 Sieve analysis data

Size (mm)	Retained weight (g)	Retained total weight (g)	Finer mass (g)	Finer percent (%)
19	1982.3	1982.3	18935.7	90.52
9.5	3460.9	5443.2	15474.8	73.98
2.36	6240.6	11683.8	9234.2	44.14
1.18	3300.6	14984.4	5933.6	28.37
0.425	2238.4	17222.8	3695.2	17.67
0.075	1923.7	19146.5	1771.5	8.47
<0.075	1771.5	20918	0	

Table A2 Modified proctor test data

Optimum Moisture Content		Zero-Air-Void Curve		
Mositure content (%)	Dry density (g/cm^3)	Mositure content (%)	Void Ratio	Dry density (g/cm^3)
4.98	1.87	2	0.05	2.56
5.87	1.91	4	0.11	2.44
7.13	1.99	6	0.16	2.32
8.26	2.09	8	0.22	2.22
9.59	2.08	10	0.27	2.13
11.45	2.04	12	0.32	2.04
		14	0.38	1.96

APPENDIX B RESILIENT MODULUS TEST

Table B1 Resilient modulus test data

MC (%)	Confining Pressure (psi)	Deviator Stress (psi)	Resilient Modulus (kips)	MC (%)	Confining Pressure (psi)	Deviator Stress (psi)	Resilient Modulus (kips)
0	3	2.7	226.372242	3.78	3	2.7	157.1874637
	3	5.4	263.1161414		3	5.4	177.0833519
	3	8.1	239.4513311		3	8.1	192.2278297
	5	4.5	315.3937862		5	4.5	232.2953248
	5	9	240.2916379		5	9	209.4792229
	5	13.5	258.5654608		5	13.5	197.9194446
	10	9	261.6698167		10	9	193.2753446
	10	18	273.9133818		10	18	189.5625784
	10	27	300.9744236		10	27	134.9774464
	15	9	275.769637		15	9	130.5972817
	15	13.5	256.4040656		15	13.5	133.4252953
	15	27	329.3219192		15	27	135.9192705
	20	13.5	294.1514339		20	13.5	129.8579322
	20	18	303.1923265		20	18	132.912835
	20	36	344.7263818		20	36	132.2931372
0	3	2.7	212.6653077	3.89	3	2.7	289.7037402
	3	5.4	601.4574244		3	5.4	174.2475687
	3	8.1	351.9970782		3	8.1	106.0001815
	5	4.5	473.0377454		5	4.5	203.301794
	5	9	335.5088666		5	9	95.45924403
	5	13.5	226.0444453		5	13.5	79.90444539
	10	9	239.610051		10	9	91.67653445
	10	18	233.268658		10	18	73.65213143
	10	27	242.2700735		10	27	93.74750974
	15	9	224.4503407		15	9	81.31200719
	15	13.5	220.2048205		15	13.5	64.60348702
	15	27	222.039681		15	27	97.07032962
	20	13.5	220.3123508		20	13.5	62.8727177
	20	18	231.3028343		20	18	65.70764844
	20	36	244.9436171		20	36	144.5195169
0	3	2.7	176.4801437	3.92	3	2.7	201.9803534
	3	5.4	271.8218462		3	5.4	75.71497634
	3	8.1	296.0954738		3	8.1	54.32954903
	5	4.5	403.791501		5	4.5	92.65462563

	5	9	278.81784		5	9	49.61938708
	5	13.5	195.4835353		5	13.5	44.68952729
	10	9	275.7956807		10	9	48.54533701
	10	18	162.6061794		10	18	41.37268315
	10	27	155.1999701		10	27	42.73759144
	15	9	232.9160205		15	9	38.98676751
	15	13.5	203.1658784		15	13.5	34.89891935
	15	27	159.2511834		15	27	43.22628117
	20	13.5	223.5036405		20	13.5	34.0752653
	20	18	182.344427		20	18	34.64013565
	20	36	158.1384149		20	36	52.36230775
2.01	3	2.7	249.0931437	3.98	3	2.7	256.7025517
	3	5.4	116.1017388		3	5.4	272.6418433
	3	8.1	100.7312449		3	8.1	170.2126134
	5	4.5	128.8211392		5	4.5	363.3974933
	5	9	96.43373363		5	9	173.1443019
	5	13.5	93.83660395		5	13.5	162.282002
	10	9	95.34357963		10	9	169.7859869
	10	18	84.0172987		10	18	147.29408
	10	27	62.48714438		10	27	114.303382
	15	9	43.2557049		15	9	122.8385957
	15	13.5	43.43132428		15	13.5	112.0225386
	15	27	64.28272984		15	27	115.5532511
	20	13.5	41.07647815		20	13.5	107.7243164
	20	18	47.00421823		20	18	104.8112658
	20	36	81.40337378		20	36	111.1379138
2.08	3	2.7	206.2742583	4.19	3	2.7	581.6950301
	3	5.4	154.6240447		3	5.4	272.2537989
	3	8.1	151.2057878		3	8.1	161.64526
	5	4.5	157.6118414		5	4.5	555.420437
	5	9	146.417946		5	9	151.0001502
	5	13.5	165.2129223		5	13.5	125.6028371
	10	9	147.0291209		10	9	143.788618
	10	18	167.6117371		10	18	107.4189475
	10	27	170.9396243		10	27	83.85206215
	15	9	127.6649348		15	9	104.7273581
	15	13.5	136.9714046		15	13.5	87.44573107
	15	27	164.0986139		15	27	85.32321637
	20	13.5	134.7609313		20	13.5	85.3429249
	20	18	145.9053751		20	18	82.09449993

	20	36	157.3770226		20	36	80.35852411
2.32	3	2.7	303.9686988	6.28	3	2.7	17.35289121
	3	5.4	401.8434628		3	5.4	15.13738784
	3	8.1	299.0104542		3	8.1	15.22565905
	5	4.5	393.3910826		5	4.5	15.70307916
	5	9	255.8295977		5	9	15.59058693
	5	13.5	237.2677359		5	13.5	16.91444208
	10	9	271.8056453		10	9	15.27547149
	10	18	157.5667446		10	18	19.20770378
	10	27	118.0545971		10	27	22.57727095
	15	9	310.5305706		15	9	14.47872202
	15	13.5	191.0459959		15	13.5	15.57274067
	15	27	121.7397912		15	27	23.9589253
	20	13.5	173.1594025		20	13.5	15.78673241
	20	18	137.6647707		20	18	17.94489516
	20	36	120.9023512		20	36	34.75325742
2.67	3	2.7	293.2580908	6.3	3	2.7	309.0351064
	3	5.4	275.7553601		3	5.4	673.259208
	3	8.1	272.786087		3	8.1	232.0383173
	5	4.5	280.7513444		5	4.5	607.4447109
	5	9	259.5951087		5	9	220.2088188
	5	13.5	195.1397707		5	13.5	179.8628539
	10	9	260.6070356		10	9	216.2473625
	10	18	178.5659129		10	18	158.3955449
	10	27	139.0942026		10	27	117.4781643
	15	9	194.9502343		15	9	151.1189879
	15	13.5	186.651449		15	13.5	139.8459376
	15	27	137.4976311		15	27	122.456602
	20	13.5	182.0108991		20	13.5	155.8633155
	20	18	147.6196006		20	18	132.0097256
	20	36	135.6515197		20	36	116.9702574
6.91	3	2.7	82.97163312	8.83	3	2.7	9.08845146
	3	5.4	57.86777472		3	5.4	8.1018951
	3	8.1	50.5294126		3	8.1	10.2907492
	5	4.5	76.47125613		5	4.5	9.519600649
	5	9	59.17102035		5	9	12.18236179
	5	13.5	61.82611108		5	13.5	16.71338344
	10	9	94.46286128		10	9	16.4858232
	10	18	89.67456207		10	18	24.06656815
	10	27	84.41773116		10	27	31.98611257

	15	9	102.1184854		15	9	18.07114058
	15	13.5	101.2118421		15	13.5	22.27996691
	15	27	118.0276376		15	27	35.51464978
	20	13.5	133.9242276		20	13.5	23.89699922
	20	18	139.5595258		20	18	29.12569891
	20	36	130.8236424		20	36	43.38137426
6.91	3	2.7	71.77954743	8.9	3	2.7	6.591731386
	3	5.4	48.34349814		3	5.4	7.15626041
	3	8.1	43.52101552		3	8.1	9.839938736
	5	4.5	63.95454526		5	4.5	8.151607776
	5	9	52.62126439		5	9	11.43597006
	5	13.5	51.29572785		5	13.5	15.84569579
	10	9	74.33989243		10	9	15.32415063
	10	18	67.12608021		10	18	21.81211272
	10	27	61.33044481		10	27	27.35249662
	15	9	89.10046131		15	9	16.34510099
	15	13.5	80.22034774		15	13.5	19.92824863
	15	27	75.34704955		15	27	31.08812058
	20	13.5	94.14868253		20	13.5	22.07782989
	20	18	91.74419902		20	18	26.76675776
	20	36	80.98259594		20	36	36.56525535
6.98	3	2.7	175.2660234	8.9	3	2.7	6.056099053
	3	5.4	71.26660774		3	5.4	7.135958951
	3	8.1	59.80505677		3	8.1	9.321694514
	5	4.5	79.30076603		5	4.5	7.670683784
	5	9	59.92617394		5	9	10.52094089
	5	13.5	58.17918064		5	13.5	12.98077738
	10	9	68.51373167		10	9	12.27908668
	10	18	60.46737807		10	18	16.79855402
	10	27	55.79547004		10	27	20.29303943
	15	9	75.94734527		15	9	10.85469832
	15	13.5	63.38279761		15	13.5	14.14428559
	15	27	62.68939247		15	27	23.73530464
	20	13.5	76.42441243		20	13.5	14.24756665
	20	18	72.74216286		20	18	19.25660138
	20	36	70.66571663		20	36	30.30041639
7.26	3	2.7	89.11848137	8.98	3	2.7	9.048828751
	3	5.4	45.74324701		3	5.4	7.863500644
	3	8.1	43.10831602		3	8.1	11.37177332
	5	4.5	50.43012043		5	4.5	9.374004381

	5	9	47.21862851		5	9	14.15399635
	5	13.5	51.79181125		5	13.5	19.02881893
	10	9	75.32347308		10	9	17.81987144
	10	18	73.00933388		10	18	26.76152121
	10	27	68.46455707		10	27	32.52520243
	15	9	93.61174014		15	9	19.79849958
	15	13.5	90.50938544		15	13.5	23.09121913
	15	27	99.23123758		15	27	36.27878453
	20	13.5	112.0776997		20	13.5	26.27879584
	20	18	121.0118262		20	18	30.28319749
	20	36	102.1627516		20	36	43.87815905
8.3	3	2.7	22.63806347	9.41	3	2.7	9.724914182
	3	5.4	16.63438935		3	5.4	11.08384048
	3	8.1	17.91231851		3	8.1	15.13179085
	5	4.5	26.71696804		5	4.5	10.95425986
	5	9	25.55230219		5	9	16.85203308
	5	13.5	26.52606213		5	13.5	21.62208196
	10	9	37.30654918		10	9	18.52204805
	10	18	36.31438109		10	18	27.46838372
	10	27	37.23081763		10	27	25.0731424
	15	9	41.4894655		15	9	13.35456983
	15	13.5	40.06148305		15	13.5	20.3232244
	15	27	46.19247542		15	27	
	20	13.5	50.27443754		20	13.5	
	20	18	51.25869717		20	18	
	20	36	54.0765276		20	36	
8.69	3	2.7	8.795103704	9.52	3	2.7	6.937781291
	3	5.4	9.537337748		3	5.4	7.34213661
	3	8.1	14.02882105		3	8.1	10.17011517
	5	4.5	11.93645554		5	4.5	7.257996807
	5	9	17.05541386		5	9	11.17801363
	5	13.5	23.44992124		5	13.5	14.5301171
	10	9	23.3786023		10	9	11.95731269
	10	18	34.63375136		10	18	18.02596457
	10	27	43.90484379		10	27	26.16599867
	15	9	25.51875056		15	9	13.27214809
	15	13.5	31.59867611		15	13.5	19.18520202
	15	27	49.91602625		15	27	29.51310493
	20	13.5	34.81032341		20	13.5	20.52589277
	20	18	41.26522919		20	18	26.1226082

	20	36	58.35715829		20	36	
8.77	3	2.7	7.712431886	9.61	3	2.7	10.20939145
	3	5.4	7.486276637		3	5.4	11.92733115
	3	8.1	10.26040867		3	8.1	16.5262665
	5	4.5	9.086775549		5	4.5	10.89865553
	5	9	12.76611318		5	9	17.85947299
	5	13.5	17.28730058		5	13.5	21.85384336
	10	9	18.123403		10	9	16.84050867
	10	18	25.74265799		10	18	26.33315457
	10	27	31.34664374		10	27	21.95018526
	15	9	21.04460482		15	9	13.04308817
	15	13.5	24.42244055		15	13.5	19.3210257
	15	27	36.83698924		15	27	26.3579984
	20	13.5	29.60309563		20	13.5	
	20	18	33.75400248		20	18	
	20	36	45.2723742		20	36	
9.81	3	2.7	5.892826508	10.8	3	2.7	3.674534
	3	5.4	7.602065982		3	5.4	5.113647
	3	8.1	11.05463691		3	8.1	7.017897
	5	4.5	6.848420023		5	4.5	4.846955
	5	9	12.26597311		5	9	8.172534
	5	13.5	16.78899288		5	13.5	10.36838
	10	9	13.11546788		10	9	9.012155
	10	18	21.65577075		10	18	12.44513
	10	27	22.63908741		10	27	
	15	9	12.65260134		15	9	
	15	13.5	18.02891723		15	13.5	
	15	27	22.53026022		15	27	
	20	13.5	17.65144441		20	13.5	
	20	18	22.00808289		20	18	
	20	36			20	36	

Table B2 Permanent deformation after test

MC(%)	Permanent Deformation (in.)	MC(%)	Permanent Deformation (in.)
0.00	0.013	6.90	0.054
0.00	0.009	6.98	0.045
0.00	0.011	7.26	0.043
2.01	0.015	8.30	0.070
2.08	0.022	8.69	0.100
2.17	0.023	8.77	0.100
2.32	0.013	8.83	0.100
2.67	0.011	8.90	0.212
3.78	0.024	8.90	0.152
3.89	0.033	8.98	0.125
3.92	0.057	9.41	0.295
3.98	0.047	9.52	0.330
4.19	0.018	9.61	0.337
6.28	0.111	9.81	0.236
6.40	0.065	10.81	0.472

APPENDIX C SWCC and GWCC TEST RESULTS

Table C1 GWCC raw data

Pressure Plate Test (Geotextile)					
Suction (kPa)	Water Content (%)	Suction (kPa)	Water Content (%)	Suction (kPa)	Water Content (%)
1	30.5194057	22	10.71929	125	3.725857
1	30.99360456	22	8.558733	125	4.175771
1	29.10026782	22	9.245913	125	4.188097
1	29.26787335	22	10.85603	200	3.209554
1	29.12683193	22	8.991982	200	3.435341
1	29.46196858	25	6.888229	200	3.155548
1	30.35413544	25	8.433579	200	3.165809
1	30.77971081	25	7.175359	200	2.607537
1	29.76146414	25	8.876842	300	2.73003
1	29.90592709	25	7.8125	300	3.439349
1	29.8591309	25	9.81545	300	4.070254
1	30.03819327	32	8.383234	300	3.644478
1	29.83862633	32	6.124011	300	3.371678
1	29.4083829	32	6.426799	450	3.350195
1	29.99187374	32	5.727516	450	3.776379
1	30.06962724	32	6.724021	450	3.911234
1	29.97428055	32	5.774457	450	3.402579
1	29.90825456	32	5.757776	450	3.333333
1	30.47899688	45	5.547398	450	3.551539
1	29.62990655	45	4.988029		
1	29.7285233	45	5.795289		
1	29.8135127	45	4.709247		
1	29.79726336	45	4.832347		
1	29.66924256	60	4.929374		
8	22.99010513	60	5.133576		
8	20.18603931	60	5.171		
8	21.87319795	60	4.827728		
8	22.40159902	60	4.830615		
8	21.83477269	95	5.098514		
10	13.58293426	95	5.545553		
10	14.61148649	95	5.240582		
10	13.95680522	95	5.339266		
10	12.48746702	95	5.217081		
10	12.81287616	100	4.450158		
10	12.17324023	100	4.247104		

15	10.48761	100	4.70639		
15	12.03856	100	4.659434		
15	12.67496	100	4.307209		
22	8.060407569	100	4.61511		
Salt Concentration Test (Geotextile)					
Suction (kPa)	Water Content (%)	Suction (kPa)	Water Content (%)	Suction (kPa)	Water Content (%)
1303	1.204819	5244	1.014713	14554	0.66345
1303	1.122895	5244	0.835509	14554	0.636574
1303	0.966495	5244	1.202532	14554	0.776197
1303	1.375712	5244	1.128527	14554	0.729108
1303	1.973684	5244	0.978593	14554	0.512164
1303	2.028081	5244	0.866667	14554	0.743494
1303	1.204819	5244	0.694074	14554	0.438356
1303	1.122895	5244	0.712897	14554	0.404391
1303	0.966495	5244	0.640205	14554	0.65703
2739	0.970874	8249	0.893389	14554	0.656814
2739	0.877743	8249	0.691643	14554	0.437158
2739	0.666263	8249	0.679206		
2739	0.827498	8249	0.749532		
2739	0.839251	8249	0.692042		
2739	0.704676	8249	0.822264		
2739	0.941828	8249	0.759346		
2739	0.838169	8249	0.752351		
2739	0.713893	8249	0.838223		
2739	0.970874	8249	0.938967		
2739	0.877743	8249	0.819672		
2739	0.666263	8249	0.893389		
3523	0.89717	8249	0.691643		
3523	0.727032	8249	0.679206		
3523	0.729108	14554	0.65703		
3523	0.912647	14554	0.656814		
3523	0.705053	14554	0.437158		
3523	0.721021	14554	0.658256		
3523	0.946372	14554	0.610433		
3523	2.10035	14554	0.718629		
3523	0.925314	14554	0.387847		
3523	0.89717	14554	0.636943		
3523	0.727032	14554	0.647821		
3523	0.729108	14554	0.672108		
5244	0.694074	14554	0.542495		

5244	0.712897	14554	0.482315		
5244	0.640205	14554	0.820232		
5244	0.636537	14554	0.820283		
5244	0.599829	14554	0.612131		
5244	0.502513	14554	0.839895		

Table C2 SWCC raw data

Pressure Plate Test (Soil)			
Suction (kPa)	Water Content (%)	Suction (kPa)	Water Content (%)
1	12.58064516	114	6.613435168
1	12.00631912	114	5.643372158
1	12.16848674	155	6.44316293
1	11.66936791	155	6.179516022
1	13.38983051	345	5.401502022
10	9.197324415	345	5.806688717
10	9.320695103	345	4.974396489
10	8.85668277	515	5.272827485
21	7.44658167	515	5.584350443
21	7.852547057	515	5.604953954
28	8.152444076	775	5.559241077
28	8.388157895	775	5.695593612
46	6.895924309	775	5.709175953
46	7.44754042	900	6.252873563
46	6.959594408	900	5.888399413
114	6.831808141	900	6.046153846

Salt Concentration Test (Soil)	
Suction (kPa)	Water Content (%)
1303	5.304447215
1303	5.467577122
1303	6.07853449
2739	5.865495725
2739	5.427883563
2739	4.81017324
3523	5.530742184
3523	5.693805
3523	4.727554549
5244	5.881005555
5244	5.188824071
5244	5.856341062
8249	5.437622469
8249	4.887860807
8249	5.636955637
14554	5.2017231
14554	5.007469706
14554	4.947586975

APPENDIX D LARGE-SCALE DIRECT SHEAR TEST

Table D.1 Large-scale direct shear test data

MC=0%		MC=2%		MC=4%	
σ (kPa)	τ (kPa)	σ (kPa)	τ (kPa)	σ (kPa)	τ (kPa)
34.6	31.84	59.28	56.63	48.73	47.36
67.41	59.24	124.39	137.62	78.87	85.4
104.4	98.03	144.3	152.83	151.56	148.71
138.1	129.3	186.48	208.2	165.07	176.2
MC=6%		MC=8%		MC=10.5%	
σ (kPa)	τ (kPa)	σ (kPa)	τ (kPa)	σ (kPa)	τ (kPa)
45.12	41.21	38.63	32.33	47.76	40.33
68.93	61.54	73.17	61.54	80.84	66.71
105.54	91.73	103.34	87.94	99.86	82.14
140.32	139.45	142.92	128.76	148.97	120.79